3-2021

Performance Analysis of Long-Term Evoluution Signals in Passive Bistatic Radar Applications Using Reduced Dimension Space-Time Adaptive Processing Techniques

Sureshan Suntharalingam

PERFORMANCE ANALYSIS OF LONG-TERM EVOLUTION SIGNALS IN PASSIVE BISTATIC RADAR APPLICATIONS USING REDUCED DIMENSION SPACE-TIME ADAPTIVE PROCESSING

THESIS

Sureshan Suntharalingam, Flight Lieutenant, RAAF

AFIT-ENG-MS-21-M-082

DEPARTMENT OF THE AIR FORCE
AIR UNIVERSITY

AIR FORCE INSTITUTE OF TECHNOLOGY

Wright-Patterson Air Force Base, Ohio

AFIT-ENG-MS-21-M-082

PERFORMANCE ANALYSIS OF LONG-TERM EVOLUTION SIGNALS IN PASSIVE BISTATIC RADAR APPLICATIONS USING REDUCED DIMENSION SPACE-TIME ADAPTIVE PROCESSING TECHNIQUES

THESIS

Presented to the Faculty

Department of Electrical and Computer Engineering

Graduate School of Engineering and Management

Air Force Institute of Technology

Air University

Air Education and Training Command

in Partial Fulfillment of the Requirements for the

Degree of Master of Science in Electrical Engineering

Sureshan Suntharalingam, M.E.(SysEng), B.E.(ECSE)

Flight Lieutenant, RAAF

March 25, 2021

AFIT-ENG-MS-21-M-082

PERFORMANCE ANALYSIS OF LONG-TERM EVOLUTION SIGNALS IN PASSIVE BISTATIC RADAR APPLICATIONS USING REDUCED DIMENSION SPACE-TIME ADAPTIVE PROCESSING TECHNIQUES

THESIS

Sureshan Suntharalingam, M.E.(SysEng), B.E.(ECSE)
Flight Lieutenant, RAAF

Committee Membership:

Maj James R. Lievsay, PhD
Chair

Dr. Julie A. Jackson
Member

Dr. Michael A. Temple
Member

AFIT-ENG-MS-21-M-082

Abstract

Widespread availability of long term evolution (LTE) signals makes them potential for use in passive bistatic radar (PBR) applications. However, their utility in such applications is yet to be fully explored. This research focuses on the key LTE signal attributes, such as subcarrier modulation schemes and bandwidth, and their effect on PBR application. Space-time adaptive processing (STAP) concepts, both full-dimension STAP (FD-STAP) and reduced-dimension STAP (RD-STAP), were employed to evaluate and compare the effects of varying signal attributes, in terms of signal to interference-plus-noise ratio (SINR) loss metrics ($\text{SINR}_{\text{L,o}}$, SINR_{L}). Simulation results concluded that decreasing LTE signal's bandwidth and increasing its bit-rate will worsen both SINR_{L} and $\text{SINR}_{\text{L,o}}$. This trend remained valid irrespective of the type of STAP algorithm used. This research further analyzed the SINR loss performance trade-off resulting from the choice of an LTE signal for airborne PBR application solely based on just one of the two signal attributes discussed in this report. Additionally, the impacts of intrinsic clutter motion (ICM) on PBR performance metrics examined and characterized using FD-STAP. The presence of ICM and subsequent increase in its wind speed had widened the clutter notches of the corresponding SINR_{L} curves. Furthermore, a significant increase in wind speed diminished the performance superiority of the low bit-rate signal over a high bit-rate signal previously characterized in scenarios without ICM. Finally, this research analyzed the impacts of matched filter (MF) length variation, which concluded that increase in MF length degrades the PBR performance.

We are what our thoughts have made us; so take care about what you think. Words are secondary. Thoughts live; they travel far.

Swami Vivekananda

Acknowledgements

I thank Maj Lievsay for his valuable insights, timely guidance and unrelenting support during my Master's program at Air Force Institute of Technology (AFIT) that culminated in the successful completion of this thesis research. Additionally, the support provided by the Engineering Faculty staff, particularly in tackling the computational resource limitations and solidifying my basic understanding of the core concepts relating to this advanced radar research, was immense. Dr. Lacey and Mr. Harris were instrumental in ensuring remote connectivity to computing resources, virtual computing in specific, was established that allowed me to continue my research remotely from home during this pandemic. Finally, the strong bonds established within the post-graduate cohort of Low Observable and Radar Engineering (LORE) section was a key catalyst in maintaining high levels of morale during this challenging but rewarding 18 months.

I thank my wife, family and friends for their continued support all the way from Australia, without which my mission here at AFIT would have been impossible.

Finally, I dedicate this research to the Royal Australian Air Force (RAAF), for entrusting me with this unique opportunity to advance my technical, professional and social mastery. It is time now to reinvest my gains back in to this organisation with the hope of furthering our radar knowledge base within RAAF.

Sureshan Suntharalingam

Table of Contents

Page

Page

List of Figures

List of Tables

List of Abbreviations

2D two-dimensional.

3D three-dimensional.

3GPP Third Generation Partnership Project.

AF ambiguity function.

AFIT Air Force Institute of Technology.

AWGN additive white Gaussian noise.

CFAR constant false alarm rate.

CID cell-identities.

CMT covariance matrix taper.

CNR clutter to noise ratio.

CP cyclic prefix.

CPI coherent processing interval.

CSRE cell-specific reference element.

CUT cell under test.

DFT discrete Fourier transform.

DL downlink.

DM-RS demodulation reference signals.

DoF degrees of freedom.

DPCA displaced phase center antenna.

EFA extended factored algorithm.

eNodeB enhanced Node B.

ESA electronically scanned array.

FDD frequency division duplexing.

FD-STAP full-dimension STAP.

FFT fast Fourier transform.

GMTI ground moving target identification.

GSM global system for mobile communications.

ICM intrinsic clutter motion.

IFFT inverse fast Fourier transform.

IPOP in-plane and out-of-plane.

ISI intersymbol interference.

JDL joint domain localized.

LORE Low Observable and Radar Engineering.

LOS line of sight.

LPR localized processing region.

LTE long term evolution.

MF matched filter.

MIMO multiple-input multiple-output.

MTI moving target indication.

OFDM orthogonal frequency division multiplexing.

OFDMA orthogonal frequency division multiple access.

PAPR peak-to-average power ratio.

PBR passive bistatic radar.

PHY physical layer.

PRF pulse repetition frequency.

PRI pulse repetition interval.

PSD power spectral density.

PSS primary synchronisation signal.

QAM quadrature Amplitude Modulation.

QPSK quadrature Phase Shift Keying.

RAAF Royal Australian Air Force.

RB resource block.

RCS radar cross-section.

RD-STAP reduced-dimension STAP.

RE resource element.

SC-OFDMA single carrier orthogonal frequency division multiple access.

SINR signal to interference-plus-noise ratio.

SMI sample matrix inversion.

SNR signal-to-noise ratio.

SRS sounding reference signals.

SSS secondary synchronisation signal.

STAP space-time adaptive processing.

TDD time division duplexing.

UE user elements.

UL uplink.

ULA uniform linear array.

WCDMA wideband code division multiple access.

PERFORMANCE ANALYSIS OF LONG-TERM EVOLUTION SIGNALS IN PASSIVE BISTATIC RADAR APPLICATIONS USING REDUCED DIMENSION SPACE-TIME ADAPTIVE PROCESSING TECHNIQUES

I. Introduction

1.1 Research Motivation

Slow-moving target identification is critical in any urban operational scenario. With ever increasing spectrum congestion, employing such a scenario in contested environments requires modern airborne radar platforms to conduct their search undetected using signals of opportunity. Increasing need for such requirements motivated this research to focus on the utility of passive bistatic radar (PBR) with long term evolution (LTE) waveform in ground moving target identification (GMTI) applications. PBR conducts its search and track activities through exploiting non-cooperative signals of opportunities such as a wide-range of terrestrial communication signals including LTE. Thus, PBR has the advantage of remaining undetected through not transmitting, instead relying on non-cooperative emitters such as LTE signals. LTE signals are chosen for this research based on humanity's ever increasing thirst for widespread wireless connectivity and increased communication bandwidth, making these orthogonal frequency division multiplexing (OFDM) communication waveforms ubiquitous.

One of the key constraints in detecting slow-moving ground targets in urban scenarios is the presence of ground clutter that suppresses the echo returns from the targets. Hence, this research uses space-time adaptive processing (STAP) techniques

to suppress clutter and to provide greater likelihood of target detection [1]. STAP is a multidimensional adaptive filtering technique that simultaneously combines signals from multiple channels of an antenna array and multiple pulses of a coherent radar waveform. The utility of LTE signals in PBR applications for GMTI will be evaluated using STAP techniques, both full-dimension STAP (FD-STAP) and reduced-dimension STAP (RD-STAP). Further analysis into the impact of LTE signal attributes, such as signal bandwidth and subcarrier modulation scheme (bit-rate), on PBR's target detection performance will also be undertaken using the same STAP techniques. Through this analysis, performance metrics for various LTE signal attribute combinations are expected to be generated. This should assist mission planners in choosing the appropriate LTE signal combination for their airborne GMTI missions based on operating environment and mission requirements.

1.2 Research Problem Statement

The aim of this research is to tackle the PBR signal selection problem in GMTI missions through assisting the mission planners in choosing an LTE signal with appropriate attributes best suited for mission needs and operational environment. This is done through,

- evaluating the utility of LTE signals in such missions within a contested and spectrum congested environment;
- analyzing the impact of varying LTE signal attributes on PBR target detection performance utilizing both FD-STAP and RD-STAP techniques; and
- presenting these results as performance metrics comparing LTE signal attributes against their corresponding signal to interference-plus-noise ratio (SINR) loss curves.

1.3 Research Objectives

The following are the primary objectives of this research:

- Evaluate the employability of LTE signals for airborne GMTI using PBR applications.
- Develop PBR performance metrics for key LTE signal attributes in terms of SINR loss using STAP techniques.

1.4 Previous Works

Maj Taylor had previously analyzed the relationship between LTE waveform attributes and PBR performance using optimum FD-STAP techniques [2]. This research will expand upon [2] through employing RD-STAP techniques, which is representative of real-world operational scenarios. Other prominent works relating to utilization of LTE signals in PBR applications and STAP techniques in target detection are summarized below.

Suitability of LTE as radar waveforms of opportunity in PBR applications was investigated and demonstrated in [3–10]. A broader overview of radar waveform diversity was documented in [11], which aided in developing the foundational understanding of radar waveform characteristics. Evers and Jackson summarized the signal structure of frequency division duplexing (FDD) LTE downlink (DL) signal and illustrated its effect on cross and self ambiguity function (AF) of the signal. The signal structure outlined in [3] extracted from [12, 13] was adopted in this research. A novel LTE signal generation tool, AFIT LTE toolbox, was developed by the researchers to aid in crafting the signals relating to [3]. However, this Master's thesis research employed MATLAB LTE toolbox instead for reasons specified within chapter III. Furthermore, [3, 4] focused on the deterministic features in examining self and cross

AF of a specific LTE signal configuration. In contrast this Master's thesis research focused on random user data portion of the signal in analyzing the impact of signal attributes such as bandwidth modes and encoding schemes. Detailed discussion into the genesis of LTE technology and in-depth analysis of its signal structure, transmission framework and other prominent aspects provided within [14,15] have greatly assisted this research in understanding, simulating and exploiting these signal waveforms.

While the above listed works investigated the signal characteristics and utility of LTE signals in radar applications, the following works proposed novel LTE and radar signal processing techniques specific to certain radar applications. A signal processing framework that iteratively detects and subtracts the most powerful signal from the reflected target signal was proposed in [7] for use in passive air traffic surveillance applications. This approach presented in [7] contrasts [3] that focused on cross AF. Furthermore, Klock's research focused on stationary transmitter and receiver setup unlike the airborne moving receiver platform considered in this Master's thesis research. Similarly, MATLAB LTE toolbox was utilized in [7], but longer duration waveform was used in contrast to this thesis research. Similarly a new processing technique based on recursive minimum mean square error called time range adaptive processing was investigated in [16] to address the sidelobe issues inherent in the pulse agile radar systems. This designed approach in [16] simultaneously estimates target's range and Doppler to suppress the range and Doppler sidelobes of a pulse-diverse system. A Bayesian framework for tracking mobile targets and estimating their velocity for a PBR system using LTE was proposed in [8], which concluded that mitigation of static clutter and direct signal is critical in target detection and estimation. A more practical analysis of the same scenario without relying on the proposed Bayesian approach was undertaken in [5,6]. The experimental research in [5,6] confirmed LTE-based PBR systems can be employed to detect and track slow-moving

ground targets such as motor vehicles and pedestrians. Furthermore, a similar experimental approach could be adopted to practically assess the performance metrics findings of this thesis research as a future task.

Hitherto there has been significant amount of research documented in literature addressing STAP in radar applications. Of these [1, 17–28] are the most relevant to this research in providing a broad concept overview of STAP in various radar applications. These works aided in establishing the STAP knowledge base prior to advanced signal processing techniques. Several such advanced STAP techniques were covered in [1, 9, 17, 29–36]. Among these, [1, 29, 30] provided the underlying signal processing models for the two RD-STAP algorithms addressed in this research, namely extended factored algorithm (EFA) and joint domain localized (JDL).

Furthermore, this thesis research used the STAP and clutter models documented in [2, 37]. Lievsay expanded the clutter models presented in [38–40] by introducing clutter covariance matrix taper to address the pulse-diverse effects of LTE waveforms. Hence, models presented within [2, 37] were used as stepping stones in constructing the simulations models of this research, while [1, 29, 30, 38, 39] were relied upon to develop the RD-STAP techniques employed in this thesis. Finally, this Master's thesis research investigated the impact of intrinsic clutter motion (ICM) on PBR performance using FD-STAP through employing the two ICM models documented in [1] and [41].

1.5 Research Methodology

This thesis research will build on the previous work conducted at AFIT. Hence, majority of this research will follow the methodology described in [2] to derive the PBR performance metrics through FD-STAP. It will expand upon the FD-STAP approach to answer the problem statement using RD-STAP, a technique represent-

ative of operational scenarios. Finally, this research in its entirety will be modeling and simulation (M&S) centric using MATLAB® to simulate the LTE signals, clutter environment, bistatic radar scene, and to perform signal processing.

1.6 Assumptions and Implications

The following list contains some of the broad assumptions underpinning this research. Specific assumptions relating to research concepts, background, and methodology are detailed in their respective chapters.

- Narrowband signal model is assumed in order to decouple the Doppler and the time-delay. Under this signal model, the signal bandwidth is assumed to be much smaller than its carrier frequency, i.e. $B \ll f_o$. Hence there is no signal correlation across the spatial domain.

- Additionally, the pulse repetition frequency (PRF) is assumed to be much smaller than the signal bandwidth ($f_r \ll B$), thus the received signal from target and interference sources are uncorrelated in slow-time (temporal domain).

- An airborne platform with side-looking uniform linear array (ULA) antenna mounted on board exploiting LTE frequency division duplexing (FDD) downlink (DL) signals is assumed throughout this research.

- A flat Earth model is assumed throughout this research.

1.7 Expected Contributions

Development of PBR performance metrics in terms of SINR loss for LTE FDD DL signals will be the main contribution of this research. This PBR performance metric is expected to assist mission planners in choosing suitable candidates or combinations of

LTE signals for a target surveillance mission. Additionally, this research is expected to further consolidate the STAP related knowledge base and serve as a platform for future research at AFIT. Furthermore, a summary of results from this research is presented in [42].

1.8 Thesis Report Organization

This research follows the five-chapter model, which is the default recommended thesis report structure for an AFIT thesis. Chapter I, introduced the research motivation and its problem statement. In addition to this, research objectives, key assumptions underpinning this research work, and a brief summary of prior research relating to this topic were documented in this chapter. Chapters II to V are structured as per below.

Chapter II contains theoretical background of key research topic areas, explained through relevant literature review findings of prior research. Chapter III describes the experimental construct of this research to address its problem statement through detailing all the relevant M&S steps employed. Results of these simulations are presented and analyzed in Chapter IV, and assessed against the research objectives and problem statement in Chapter V. Chapter V also proposes future work candidates to expand on this research.

II. Background Theory

2.1 Chapter Overview

The aim of this chapter is to equip the reader with the basic underlying theoretical concepts relating to this thesis research. Brief overview of the core concepts relating to this research, such as LTE signal transmission and structure, radar signal processing including FD-STAP and RD-STAP algorithms, and PBR, is provided within this chapter. This overview incorporates the literature review findings conducted in preparation for this research within relevant sections.

2.2 Notation Convention

Prior to introducing the theoretical background, the standard convention in technical writing notation adopted throughout this report is outlined below for reader's reference.

- Matrices are represented in uppercase bold face symbols.
- Vectors are represented in lowercase bold face symbols. All vectors used in this report are column vectors unless specified otherwise.
- Scalars are represented in lowercase regular face symbols.
- Linear transformations of a vector or matrix, projecting them to a lower dimensional subspace, are represented using the same corresponding symbol with a tilde accent on top. For example, $\tilde{\mathbf{v}}$ is the transformation of space-time steering vector $\mathbf{v}$.
- Estimates of matrix, vector or scalar variable are represented using the same corresponding symbol with a hat accent on top. For example, $\hat{\mathbf{R}}$ is an estimate

of space-time covariance matrix, $\mathbf{R}$.

- Identity matrices are represented with their dimensions as subscripts. For example, $\mathbf{I}_N$ is an identity matrix of size $N \times N$.

2.3 LTE Downlink Transmission

LTE communication signals form the basis of this research. As such, a brief overview of LTE DL transmission framework is provided in this section.

2.3.1 LTE Downlink Transmission Overview

Each LTE signal consists of four distinct layers: physical layer (PHY), medium access control (MAC), radio link control (RLC) and packet data convergence protocol (PDCP) layers. PHY layer will be the primary focus of this thesis research as it governs the signal structure of an LTE signal.

The key characteristic requirements that influenced the design of PHY layer are high peak transmission rates, spectral efficiency and varying channel bandwidths [43]. Orthogonal frequency division multiplexing (OFDM) and multiple-input multiple-output (MIMO) technologies were adopted by the Third Generation Partnership Project (3GPP) [14], a global collaborative effort, to develop the next generation wireless communication framework. Together, these two technologies constitute the key difference between LTE and 3G signals.

2.3.2 OFDM Overview

OFDM is both a modulation and multiple access scheme employed in LTE signal framework to offer optimal transmission rate over wideband channels [14]. It relies on using multiple narrowband subcarriers that spread over a wideband channel bandwidth [43]. Thus, OFDM is a multicarrier modulation scheme, which is a key point of

distinction between the earlier iterations of narrowband wireless cellular frameworks that relied only on single carrier modulation schemes such as wideband code division multiple access (WCDMA) and global system for mobile communications (GSM).

OFDM of an LTE signal is implemented through converting the required number of subcarriers, N_s, into time domain signal using N_s-point inverse fast Fourier transform (IFFT). This conversion results in a time domain vector of duration T_u, which is the time superposition of N_s narrowband modulated subcarriers. Conversely, applying fast Fourier transform (FFT) to a parallel sequence of N_s independently modulated data symbols in time domain results in a frequency domain waveform of N_s orthogonal subcarriers [44]. These LTE subcarriers are usually represented as complex data symbols in the frequency domain. Subcarrier frequencies are chosen such that they are orthogonal to each other in order to eliminate cross-talk or interference between the subcarriers. Basically, orthogonality ensures mitigation against intersymbol interference (ISI). However, propagation of LTE wireless signal introduces multipath fading effects at receiver due to OFDM requiring accurate frequency synchronisation between the transmitter and receiver. Therefore, in order to mitigate this frequency deviation issue at the receiver, a guard interval known as cyclic prefix (CP) of duration T_{CP} is introduced into the LTE signal structure. Thus, the resulting overall symbol duration is $T_{sym} = T_u + T_{CP}$. Finally, Figure 2.1 shows a pictorial overview of LTE DL transmission that encapsulates the concept discussed above.

2.3.3 LTE Physical Layer Overview

LTE PHY is responsible for all radio signal transmission, reception and all associated signal processing between user elements (UE) and enhanced Node B (eNodeB) [14]. Implementation of OFDM and MIMO is also carried out in this layer. Two different duplexing modes are utilised in LTE signal transmission: frequency di-

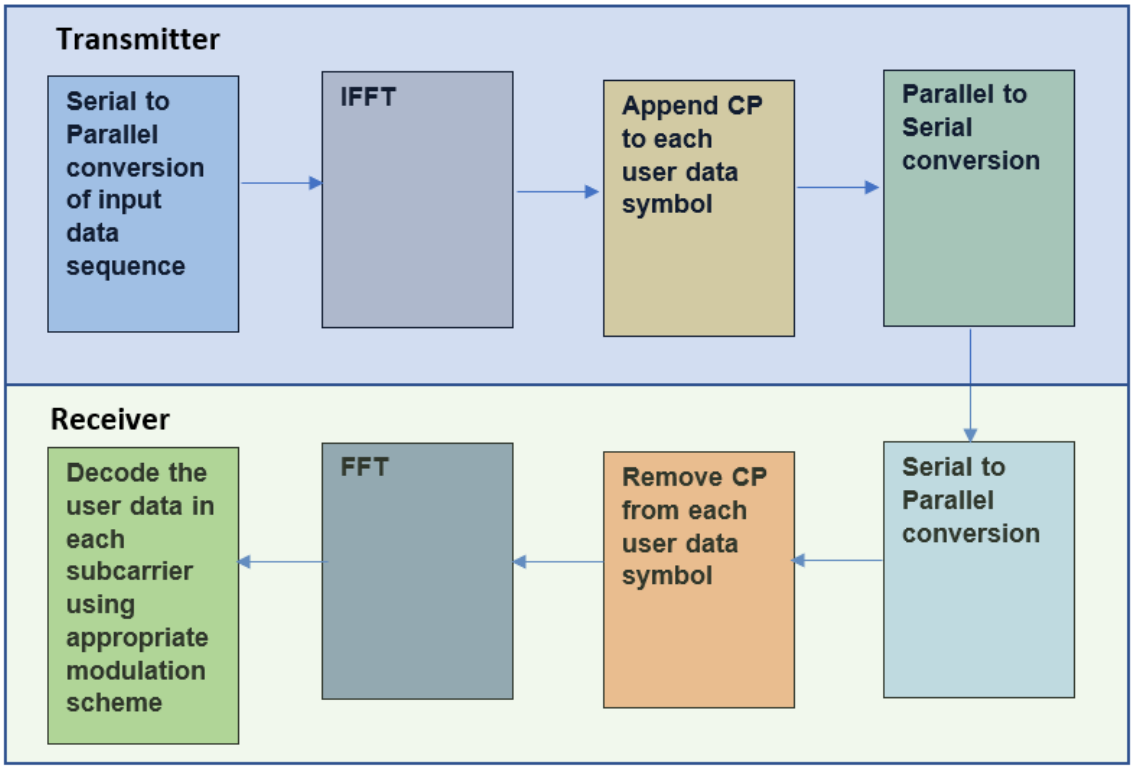

Figure 2.1: LTE FDD DL transmission overview demonstrating the implementation of OFDM through Fourier transforms and multipath interference mitigation through incorporation of CP into LTE signal structure.

vision duplexing (FDD) for signal downlink (DL) and time division duplexing (TDD) for uplink (UL). Each of these modes uses different variations of OFDM access technology to implement signal multiplexing to allow access to multiple users in the available bandwidth – orthogonal frequency division multiple access (OFDMA) in FDD DL, and single carrier orthogonal frequency division multiple access (SC-OFDMA) in TDD UL respectively. Figures 2.2 and 2.3 depict the partitioning of an LTE radioframe in FDD DL and TDD UL transmission modes respectively. This research will solely focus on FDD DL transmission mode with detailed discussion provided in Section 2.3.4.

One of the key drawbacks of OFDMA is its high peak-to-average power ratio (PAPR) due to random constructive addition of subcarriers and adjacent channel

interference through spectral spreading [43]. PAPR is often mitigated using complex filtering techniques normally implemented at cellular base stations. The same implementation is cumbersome in user elements (UE). Hence, SC-OFDMA is utilized in LTE UL mode to reduce PAPR. Conversely, OFDMA is employed in LTE DL, as the base stations can accommodate the complex filters required to alleviate high PAPR unlike UE in the case of LTE UL scenario.

2.3.4 LTE Signal Structure

Signal structure of an LTE FDD DL radioframe, spanning a duration of 10 ms, is depicted in Figure 2.2. Each radioframe is partitioned to 10 subframes, 20 slots or 140 symbols [13, 15]. The total number of subcarriers of each of these LTE symbols, N_s, are partitioned further into data (N_u), DC (N_{dc}) and guard-band (N_g) subcarriers, whose exact number depends on the channel bandwidth of the LTE signal. Each of

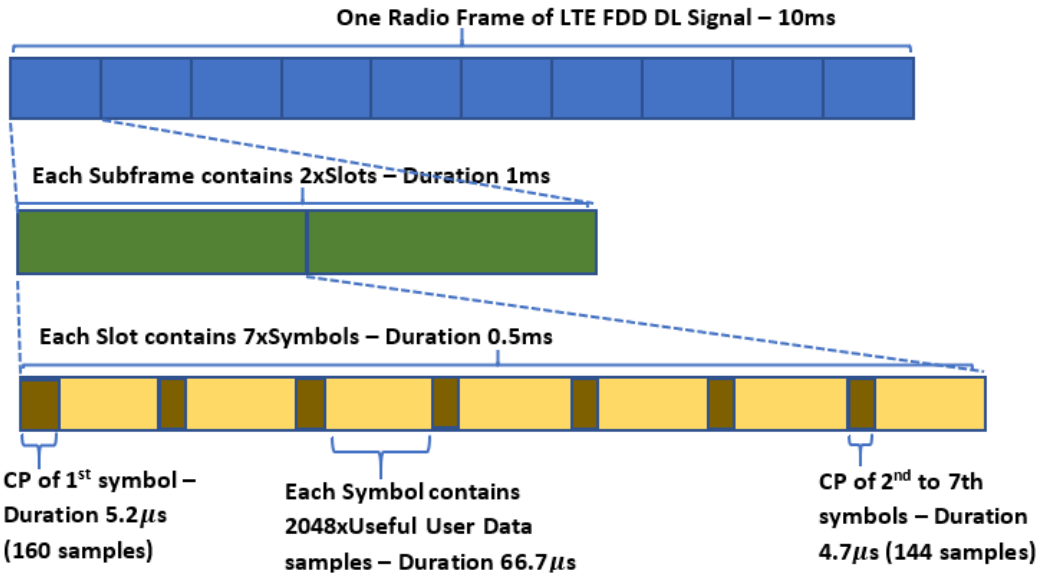

Figure 2.2: Pictorial breakdown of an LTE FDD DL radioframe in normal CP mode showing the hierarchical partitioning from radioframe to symbol.

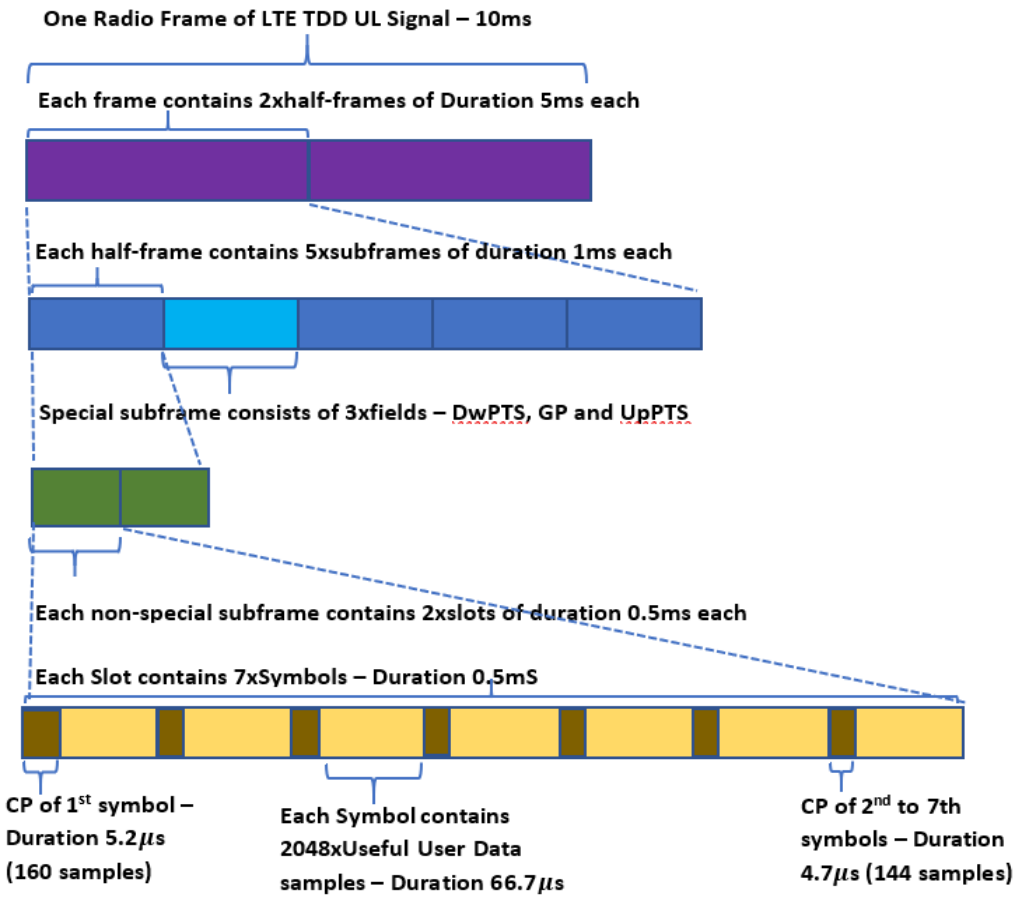

Figure 2.3: Signal Structure of an LTE FDD UL radio frame with notable difference of each radioframe partitioning to two half-frames, which subsequently partitions to special and non-special subframes.

these subcarriers have a frequency separation of 15 kHz, with channel bandwidth, B, ranging from 1-20 MHz. Each of the subcarrier is modulated using either quadrature Phase Shift Keying (QPSK), 16 quadrature Amplitude Modulation (QAM) or 64 QAM. Signal bit-rate is dependent on these subcarrier modulation schemes. Complexity of the subcarrier modulation scheme influences the signal bit-rate such that the complex modulation scheme signal is transmitted at higher bit-rate than the signal modulated using less-complex encoding scheme. Therefore, 64QAM signal, considered to be the complex of the three LTE subcarrier modulation schemes, has

the highest signal bit-rate while QPSK has the lowest bit-rate. Time duration of each symbol is 66.67μs, while time duration of each of sample is expressed using the basic time unit in LTE transmission T_{sam}= 1/30720000 = 32.55 ns. In addition to the user samples, each symbol also contains CP of varying sample length.

In the normal CP mode the first symbol of a slot has a CP of 160 samples long; each of the remaining six symbols contain a CP of 144 samples. The first symbol has a longer CP length to ensure that the overall slot length in terms of T_{sam} is divisible by the slot sample length of 15360 [43]. These CPs are copies of the end portion of their respective symbols appended to their beginning to mitigate multipath interference effects [3]. In the extended CP mode, a slot has 6 symbols to accommodate the longer CP length of 512 samples. The normal CP mode is employed in urban areas with smaller wireless communication cells. Conversely, the extended CP mode is adopted in rural areas with larger cells. The CP portions of LTE symbols will be removed when generating the LTE pulse trains in order to analyze the random user data content of these communication waveforms, which is detailed in Chapter III. Table 2.1 summarises some of the key parameters of LTE DL FDD radioframe for reference [43]. Interestingly, not all subcarriers are used or modulated, with only the data subcarriers are modulated with a chosen modulation scheme. The remaining subcarriers, such as guard, are not used which accounts for 10% of the overall signal bandwidth. This results in an LTE signal's effective bandwidth, B_e, to be approximately equal to 90% of its corresponding bandwidth mode (B) as shown in Table 2.1.

In frequency domain, an LTE signal is usually represented in terms of its subcarriers and resource blocks. The number of subcarriers, N_s, varies depending on the channel bandwidth as shown in Table 2.1. Each of these subcarriers is separated by a frequency spacing, Δf, of 15 kHz. Furthermore, an LTE signal is divided in both time and frequency domains into resource blocks (RBs). In frequency domain, each

RB spans 12 subcarriers while in time domain, each RB has a duration of one slot (0.5 ms) [14, 15]. The number of RBs also varies with channel bandwidth, with smallest RB allocation of 6 for a channel bandwidth of 1.5 MHz and 100 RBs for 20 MHz. Each of these RBs is further partitioned into resource element (RE) spanning the length of one OFDM symbol duration in the time domain and one subcarrier frequency spacing in the frequency domain (Δf). An RE, equalling one OFDM subcarrier, is the smallest unit in the LTE time frequency grid as shown in Figure 2.4. One RB consists of 84 and 72 REs in normal and extended CP modes respectively. Furthermore, from Figure 2.4, it is evident that number of RBs does not change between the two CP modes of a specific bandwidth mode while it does change with respect to B as shown in Table 2.1. Conversely, RE which depends on number of symbols, N_{sym}, varies with change in CP mode.

Table 2.1: LTE DL FDD Physical layer key parameters

B [MHz]	**1.4**	**3**	**5**	**10**	**15**	**20**
T_{frame} [ms]	10					
$T_{subframe}$ [ms]	1					
Δf [kHz]	15					
f_s [MHz]	1.92	3.84	7.68	15.36	23.04	30.72
N_{sym} [symbols]	7/6 (normal/extended CP)					
N_s [subcarriers]	128	256	512	1024	1536	2048
N_u [subcarriers]	72	180	300	600	900	1200
N_g [subcarriers]	55	75	211	423	635	847
N_{dc} [subcarriers]	1					
Number of RBs	6	15	25	50	75	100
B_e [MHz]	1.095	2.715	4.515	9.015	13.515	18.015
T_{CP} (normal CP) [μs]	5.2 (first symbol) / 4.69(remaining symbols)					
T_{CP} (extended CP) [μs]	16.67					
T_{sym} [μs]	66.67					

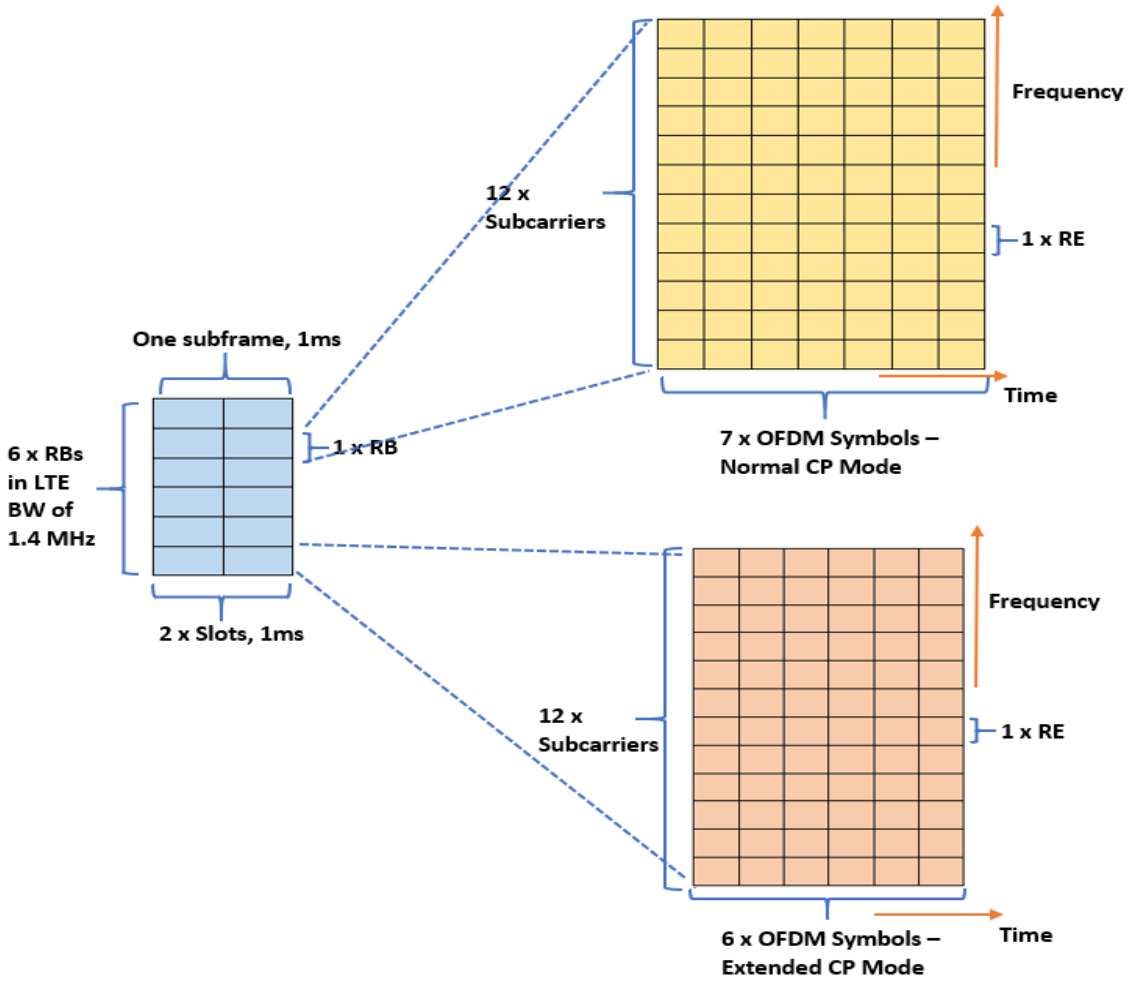

Figure 2.4: Time-Frequency grid showing the mapping between an LTE FDD DL subframe and one slot in both normal and extended CP modes. The 1.4 MHz bandwidth signal shown contains six RBs per slot. Each RB contains 12 subcarriers in frequency domain with a Δf of 15 kHz and 7 or 6 symbols in time domain with a T_{sym} of 66.67μs. Hence in total, each 1.4 MHz LTE signal contains six RBs and 84 REs in normal CP mode and 72 REs in extended CP mode per each slot.

2.3.5 LTE Reference and Synchronization Signals

2.3.5.1 LTE Reference signals

LTE signals contain cell-specific reference element (CSRE) in its time-frequency grid to enable channel estimation and coherent demodulation at the UE [14]. These reference signals are inserted in the first and the third last symbol with an intra-

symbol spacing of 6 subcarriers between each CSRE. Additionally, these CSREs are also staggered every three subcarriers between symbols, resulting in a total of four CSREs per each RB. Figure 2.5 shows the locations of CSREs on a time-frequency grid of a 1.4 MHz LTE DL signal subframe. CSREs are made up of complex values corresponding to 504 two-dimensional (2D) reference signal sequences determined according to the symbol position and cell identity [15]. LTE specification [12, 13] specifies 504 different reference sequences to 504 different cell identities; 168 pseudo-random cell-identity groups with three orthogonal physical layer identities in each group. Even though they are pseudorandom, CSREs can be known *a priori*, through knowing PHY layer cell-identities (CID) [3, 44]. Finally, the UE will interpolate over multiple CSREs to estimate the channel [3, 43].

Unlike DL, the UL mode employs two reference signals: demodulation reference signals (DM-RS) and sounding reference signals (SRS). DM-RS are used to implement coherent signal demodulation at eNodeB. Conversely, SRS are used to enable frequency selective uplink scheduling of UE, while DM-RS is utilized for coherent

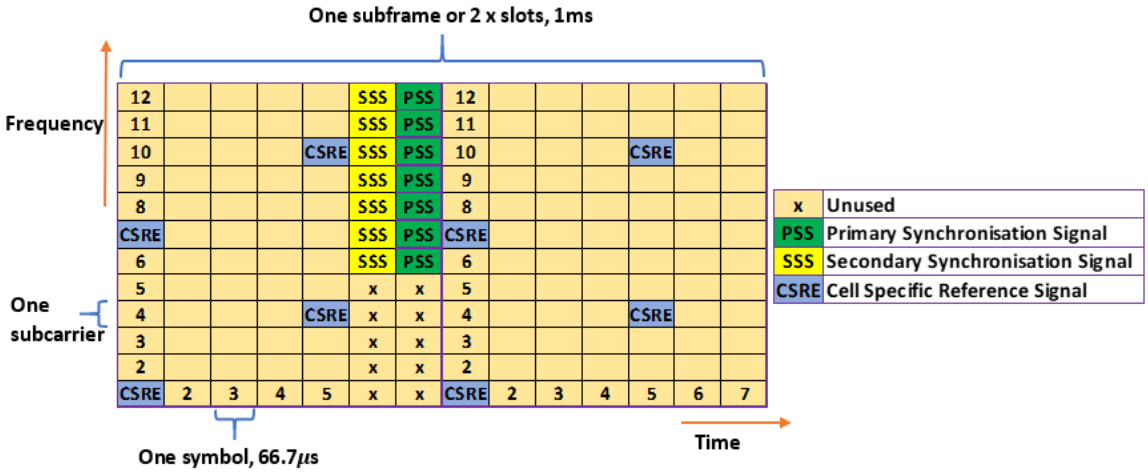

Figure 2.5: Resource grid for the duration of one DL subframe of 1.4 MHz LTE FDD DL signal showing the locations of CSRE, PSS and SSS. The resource grid also shows the unused subcarriers - five subcarriers on either ends of the 62 synchronization subcarriers in sixth and seventh OFDM symbols of a normal CP mode LTE signal.

demodulation over a specific bandwidth assigned to a UE [14].

2.3.5.2 LTE Synchronization signals

LTE signal uses 504 PHY layer CID assigned to transmitters of different cells, to enable UE to separate the information received from different transmitters [3, 43]. These CID are a combination of 168 physical cell identity groups and three physical layer identities within each physical layer group. Each CID is made up of unique pair of primary synchronisation signal (PSS) and secondary synchronisation signal (SSS); primarily used for initial DL synchronization of the network [3, 14]. Using PSS, UE is able to identify signal transmission cell's physical layer identity: 0, 1 or 2. Similarly, UE also determines the physical layer identity group number using PSS: one of 0 to 167. UE combines these two numbers to determine CID of the transmission cell. UE uses this CID to workout the locations of CSRE; thus enacting channel estimation and cell synchronization using synchronization and reference signals. Basically, cell synchronization is the primary step adopted by UE to acquire CID that enables it to read the user data from a particular cellular network. These synchronization signals are transmitted twice per each radioframe: once on the first subframe (first slot) and then on the sixth subframe (11^{th} slot). PSS is located in the last symbol of first and 11^{th} slots and SSS located in the symbol immediately preceding the PSS symbol (second last symbol of these slots). In frequency domain, synchronization signals occupy the central six RBs regardless of the bandwidth mode. Specifically, these synchronization sequences uses 62 equally spaced subcarriers in total with 31 on either side of the DC subcarrier, resulting in five subcarriers at each ends of sixth and seventh symbols of 1.4 MHz signal unused. Figure 2.5 shows location of PSS and SSS of 1.4 MHz bandwidth LTE signal over two RBs of the first two slots [3, 14, 43].

2.4 Radar Signal Processing Basics

The most primitive function of a radar as its expanded acronym suggests is radio detection and ranging (RADAR) of targets. Various signal processing techniques are used in analyzing the received signal in order to detect the presence of a target and to extract its critical attributes such as range, velocity and bearing. Three of the key signal processing techniques will be introduced in the following subsections. Prior to this introduction, a brief overview of pulsed-Doppler radar signal transmission is provided here for reference.

A phased array radar, typically monostatic, transmits a pulsed-waveform (pulse-train) comprised of pulses of duration τ, normally referred to as pulsewidth. Each of these pulses forms a time-domain envelope of a modulated signal with a higher carrier frequency. A radar transmits this pulsed-waveform and awaits for its reflection to reach its receiver for a specific duration known as inter pulse period (IPP). Thus, the total duration of pulse transmission and received signal waiting period is called pulse repetition interval (PRI), which repeats at a frequency of pulse repetition frequency (PRF).

Advanced radar signal processing usually operates on data sampled in more than one domain [38]. Collection of range samples over a single pulse duration at a frequency equalling pulse bandwidth is called fast-time. Similarly, calculation of the phase drift or Doppler processing over many pulses at each range bin at radar's PRF is called slow-time. The processing frequency in slow-time (PRF) is much smaller than that of fast-time (pulse bandwidth), i.e. $f_r \ll B$, where f_r is the PRF of the radar waveform [2, 38]. Furthermore, processing of radar signal data through applying suitable weights to maximize signal to interference-plus-noise ratio (SINR) in both temporal (pulse) and spatial (receiver channel) dimensions is known as STAP, commonly used in phased array radars. Figure 2.6 contains a three-dimensional (3D)

radar data cube highlighting various signal processing methods in their corresponding dimensions [1,39]. This research will focus only on fast-time (pulse compression), slow-time (Doppler processing) and STAP.

2.4.1 Fast-Time Processing

The radar data cube in Figure 2.6 shows a total of L samples of the complex baseband signal corresponding to successive range intervals sampled at pulse bandwidth or greater to satisfy the Nyquist criterion for each pulse transmitted. These range samples are referred to as range bins once converted to distance using the signal propagation speed, which is equal to speed of light for the purpose of this research. Pulse compression is the common signal processing technique employed in fast-time

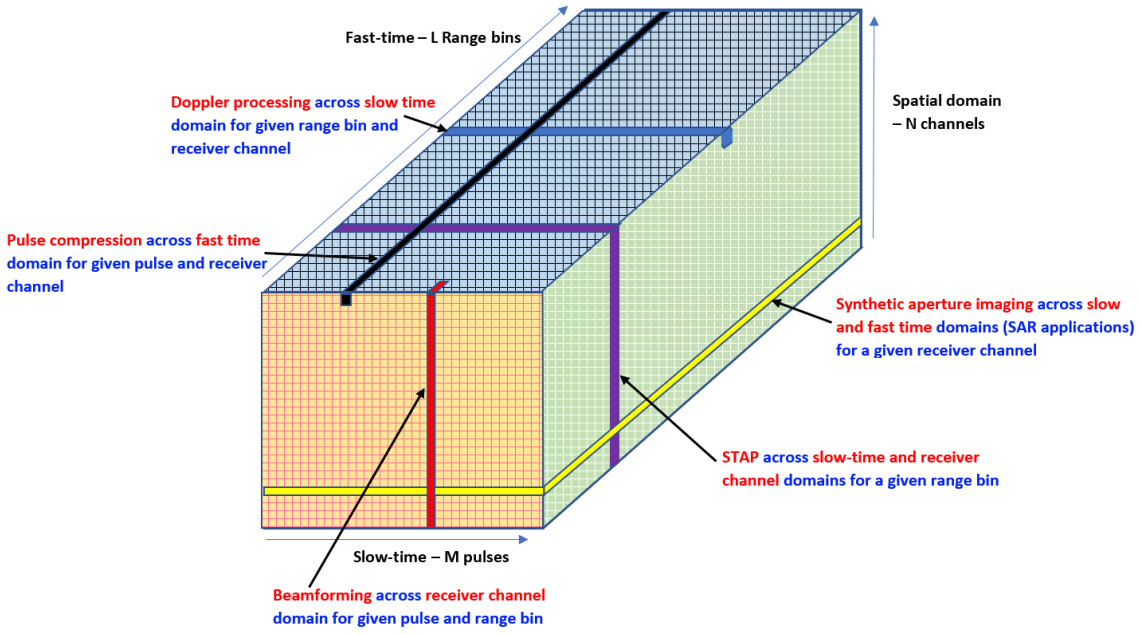

Figure 2.6: A 3D radar data cube, showing various radar signal processing techniques in their respective dimensions. It depicts received data over one coherent processing interval (CPI) comprised of LMN complex baseband signals, where L range samples are collected for each pulse to cover the range interval by a single channel. With a total of M pulses and N channels, these received complex baseband signals are represented as a $L \times M \times N$ data cube.

dimension. It essentially uses waveform design to decouple energy and resolution by exploiting amplitude, phase, or frequency modulation to increase waveform bandwidth while maintaining its pulse width such that $B \gg 1/\tau$ [38].

In radar application, target detection is carried out using the reflected signal in fast-time, through calculating its output signal-to-noise ratio (SNR) instead of analyzing or decoding the received signal [2, 45]. Thus, the focus of signal processing in this dimension is on maximizing the SNR of the received signal through applying appropriate match filter weights rather than preserving its signal shape. The impulse response of the matched filter of a finite length signal is the time-reverse complex conjugate of the received signal. Consider a reflected signal $r(t) = s(t) + n(t)$, where $s(t)$ is the transmitted signal and $n(t)$ is the additive white Gaussian noise (AWGN) signal. The matched filter is designed with an impulse response, $h(t)$, such that it maximizes the SNR at a predetermined delay of t_0. We know, for this condition to be true, $h(t) = s^*(t_0 - t)$ must hold true. This condition results in a maximum SNR at $t = t_0$ of $2E/N_0$, where E is the signal energy and N_0 is the noise signal energy [45]. Therefore, the weights that needed to be applied to the reflected signal to maximize the SNR, $\mathbf{w}$, is equal to conjugate of the digitized transmit signal, $s^*(n)$ [2].

Width of the matched filter response mainlobe equates to the achievable range resolution, ΔR, of the corresponding radar transmit waveform. For a monostatic radar the range resolution is

$$\Delta R = \frac{c}{2\,B}. \tag{2.1}$$

Similarly, unambiguous range, R_{ua}, is the maximum range at which range to a target can be measured unambiguously by the radar, expressed mathematically as

$$R_{ua} = \frac{c}{2f_r}. \tag{2.2}$$

2.4.2 Slow-Time Processing

Slow-time processing, widely referred to as Doppler processing, uses Doppler shift information to enable target detection in environments where clutter is the dominant interference. It also measures the radial velocity of the targets through their Doppler frequency shifts [38]. Moving target indication (MTI) and pulse-Doppler processing are the two specific classes of Doppler processing, which are not discussed in detail as part of this research. However, [38] is a good source of information on these techniques.

The Doppler shift, f_D, that is at the core of Doppler processing is defined as the difference between the frequency received, f_R, and frequency transmitted, f_T, expressed as [46]

$$f_D = f_T - f_R = \frac{-2v_r}{\lambda} = \frac{-2v}{\lambda}\cos\psi, \tag{2.3}$$

where v_r is the target's radial velocity, λ is the signal wavelength, ψ is the cone angle between the target's velocity vector and radar's line of sight (LOS) [38].

Doppler shift induced by a typical ground moving target is minimal, but the accumulated change in phase over slow-time is more detectable [2]. Doppler processing is focused on examining these accumulated phase changes over the normalized frequency, $\bar{f}_D$, in the range $\pm$ 1/2 cycles per sample. The unambiguous Doppler frequency range of the radar, f_{ua}, is expressed as

$$f_{ua} = \pm\frac{f_r}{2}, \tag{2.4}$$

which is the the maximum range of Doppler shift frequencies that can be unambiguously measured [38].

Equations (2.2) and (2.4) highlight the existence of the trade-off between unambiguous range and unambiguous Doppler of a pulsed-waveform. These two variables

are dependent on radar signal's PRF and are inversely related to each other. Hence, a high PRF system will offer superior (larger) f_{ua} with inferior (smaller) R_{ua} and vice versa for a low PRF system. Thus, a high PRF system is well suited for measuring targets with faster speeds as its Doppler shift measurement is always unambiguous. Conversely, a low PRF system is unambiguous in range for all targets of interest. These systems are best suited in detecting slow moving targets that are farther away [38]. Finally, a medium PRF system will have both range and Doppler ambiguities and employed in scenarios where such tradeoffs are acceptable.

The aggregation time of these slow-time time samples over a single range bin is called coherent processing interval (CPI), which is equal to the total number of pulses contained in one CPI times the PRI of the system (assuming fixed PRF system). Thus, increasing the number of pulses transmitted in one CPI increases the number of samples aggregated across the slow-time, which also increases the number of samples in the $\bar{f}_D$ range. This essentially, results in improvement of Doppler resolution which is given by

$$\Delta f_D = \frac{f_r}{M}, \tag{2.5}$$

where M is the number of pulses transmitted in one CPI.

2.5 Fully Adaptive STAP

2.5.1 Platform Geometry

STAP systems rely on electronically scanned array (ESA) antenna system mounted on an airborne platform to scan a target scene of interest. ESA is usually planar in geometry and can enable target detection over slow-time, fast-time, and multiple spatial domains (in azimuth and elevation). However, the 2D STAP employs a uniform linear array (ULA) which is limited to one spatial dimension. Basically, a ULA

gathers radar data in two temporal and one spatial dimension over a given CPI. The ULA geometry depicted in Figure 2.7 forms the geometry reference for this thesis report.

A typical ULA uses an array of sensors to estimate the direction of the returned electromagnetic wave by measuring the time difference of arrival as a phase variation across the aperture. For this research, each antenna element of this ULA has a dedicated channel. Each channel down-converts the received signal to baseband and then applies match filtering to the down-converted signal. This match-filtered signal is then sampled or digitized by an analog-to-digital converter prior to feeding it through to the digital processor for post-processing [1, 39]. The digitized data obtained from each of the three dimensions, forms the 3D radar data cube. Figure 2.6 depicts a 3D radar data cube highlighting various signal processing methods as a reference. This thesis report focuses only on STAP.

The following assumptions relating to STAP are applied throughout this research [2, 17, 39]:

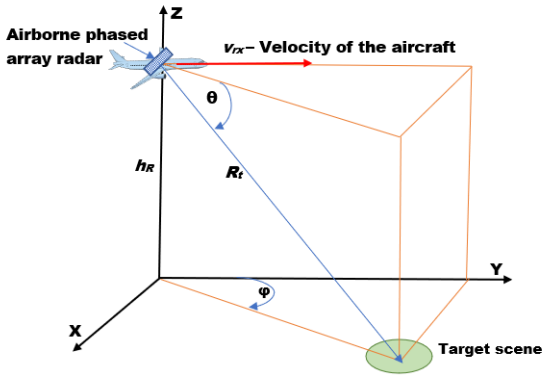

Figure 2.7: Airborne phased array radar platform geometry for an arbitrary target scene. θ is the elevation angle, ϕ is the azimuth angle, v_{rx} is the velocity of the aircraft, h_R is the height of the airborne radar platform, and R_t is the range to the center of the target scene from the airborne radar.

- ESA is a ULA with N receiver channels across azimuth.
- Far-field approximation is applied to the signal propagation indicating a planar propagating wave.

Other assumptions specific to signal model and data processing are introduced progressively throughout this report.

The respective phase measured at the n^{th} spatial channel of the ULA depicted in Figure 2.7 due to a propagating plane wave with specific direction of arrival is given as

$$\gamma_{s/n} = \tau_n \omega \tag{2.6a}$$

$$\text{where } \tau_n = \frac{\mathbf{k}(\phi, \theta) \cdot \mathbf{d}_n}{c} \tag{2.6b}$$

$$\text{and } \mathbf{d}_n = d_{x/n}\hat{\mathbf{x}} + d_{y/n}\hat{\mathbf{y}} + d_{z/n}\hat{\mathbf{z}} \tag{2.6c}$$

where

- τ_n is the time-delay between reception of the plane wave at the reference point and the n^{th} channel,
- ω is the angular frequency in radians,
- $\mathbf{d}_n$ is the position vector corresponding to the phase center of n^{th} channel,
- $\mathbf{k}(\phi, \theta)$ is the unit vector pointing normal to the plane wave in terms of azimuth and elevation angles,
- c is the velocity of light,
- $d_{x/n}, d_{y/n}, d_{z/n}$ represents the Cartesian coordinates of the n^{th} channel phase center, and
- $\mathbf{x}, \hat{\mathbf{y}}, \hat{\mathbf{z}}$ are the unit vectors along these Cartesian axes.

Substituting (2.6b) and (2.6c) into (2.6a), results in [17]

$$\gamma_{s/n} = \frac{\omega}{c}\, d_{x/n} \cos\theta \sin\phi = \frac{2\pi}{\lambda}\, d_{x/n} \cos\theta \sin\phi \tag{2.7}$$

The spatial and temporal components of the space-time snapshot, $\boldsymbol{\chi}_s$ and $\boldsymbol{\chi}_t$, of the received signal at l^{th} range gate of this N-channel ULA with a transmit waveform comprised of M pulses at a pulse repetition interval PRI of T are expressed as

$$\boldsymbol{\chi}_s = \alpha_s \mathbf{a}(\vartheta) \tag{2.8a}$$

$$\boldsymbol{\chi}_t = \alpha_t \mathbf{b}(\bar{\omega}) \tag{2.8b}$$

where, ϑ and $\bar{\omega}$ are the normalized spatial and Doppler frequencies corresponding to the spatial and temporal dimensions, with steering vectors in these dimensions denoted by $\mathbf{a}(\vartheta)$ and $\mathbf{b}(\bar{\omega})$ respectively and expressed mathematically as

$$\mathbf{a}(\vartheta) = \left[1; e^{j2\pi\vartheta}; \ldots; e^{j(N-1)2\pi\vartheta}\right], \tag{2.9a}$$

$$\mathbf{b}(\bar{\omega}) = \left[1; e^{j2\pi\bar{\omega}}; \ldots; e^{j(M-1)2\pi\bar{\omega}}\right]. \tag{2.9b}$$

Equations for ϑ and $\bar{\omega}$ are given as

$$\vartheta = \frac{\mathrm{d}}{\lambda_0} \cos\theta \sin\phi, \tag{2.10a}$$

$$\bar{\omega} = \frac{2v_r}{\lambda f_r}. \tag{2.10b}$$

Ward and Melvin provided detailed derivations of these steering vectors in [1] and [17]. The space-time steering vector is expressed as the Kronecker product of

these two individual steering vectors.

$$\mathbf{v}(\vartheta, \bar{\omega}) = \mathbf{b}(\bar{\omega}) \otimes \mathbf{a}(\vartheta) \tag{2.11}$$

2.5.2 Radar Data Cube

The radar cube previously introduced in Figure 2.6, corresponds to a single CPI which contains complex baseband space-time and range samples within its three dimensions:

- N rows corresponding to number of channels of ULA with each row containing spatial sample on which the processor performs beamforming,
- M columns corresponding to number of pulses, with each column containing slow-time samples on which the processor performs Doppler processing, and
- a total of L range samples are contained in its third dimension, which are used in match-filter processing [39].

In STAP, the processor performs beamforming across the rows and Doppler processing across the columns for a given range cell under test (CUT) as depicted in Figure 2.8. Thus, the set of all samples of the match filtered signal for the CUT is arranged to form a matrix shown in Figure 2.8. In order to process the range CUT, the cells of the matrix are re-arranged to a single column vector, $\boldsymbol{\chi}$, of length $MN \times 1$, commonly referred to as space-time snapshot as per shown through the STAP processing chain in Figure 2.9 [2, 39]. Hence, a space-time snapshot is defined to be the slice of datacube corresponding to a single range bin [1]. This space-time snapshot can be decomposed into

$$\boldsymbol{\chi} = \alpha \mathbf{v}(\vartheta, \bar{\omega}) + \boldsymbol{\chi}_u, \tag{2.12}$$

where its undesired noise plus interference component, $\boldsymbol{\chi}_u$, is further decomposed into,

$$\boldsymbol{\chi}_u = \boldsymbol{\chi}_c + \boldsymbol{\chi}_n, \tag{2.13}$$

where $\boldsymbol{\chi}_c$ and $\boldsymbol{\chi}_n$ are the clutter, and noise space-time snapshot contributions.

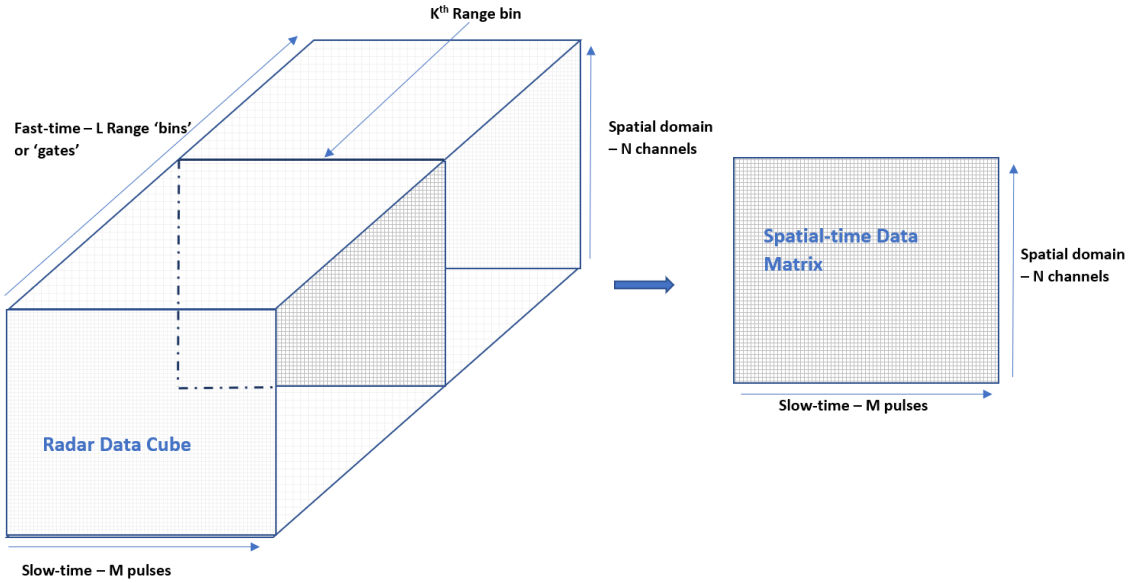

Figure 2.8: 3D radar data cube with L range bins, M slow-time pulses and N phased array channels corresponds to a single CPI which has been converted into complex baseband samples through pre-processing techniques [17]. Space-time data matrix corresponding the range CUT at k^{th} range bin is extracted on which STAP will be applied to determine SINR performance loss.

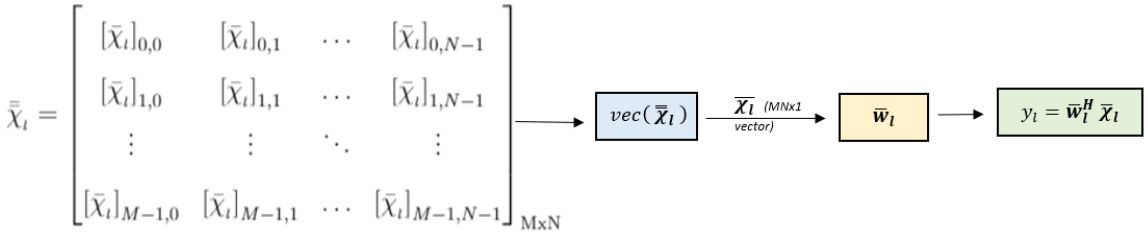

Figure 2.9: A generic processing chain associated with STAP begins with vectorizing the space-time data matrix, $\boldsymbol{\chi}_l$ from $M \times N$ matrix to $MN \times 1$ vector. Once vectorized, the processor applies complex transpose of the space-time weight vector of size $MN \times 1$ to yield a scalar test statistic y_l which will be compared with a pre-defined threshold to determine the appropriate hypothesis: H_1 or H_0.

2.5.3 Clutter Signal Modeling

Clutter is the most complicated source of interference as it is distributed in both temporal and spatial domains. It also spreads in Doppler, induced due to platform motion [1]. This thesis report only considers ground based stationary clutter sources for simplicity. The clutter component of a space-time snapshot is

$$\boldsymbol{\chi}_c = \sum_{k=1}^{N_r} \sum_{i=1}^{N_c} \alpha_{ik} \mathbf{v}(\vartheta_{ik}, \bar{\omega}_{ik}), \tag{2.14}$$

where N_r is the number of range ambiguities, and N_c is the number of independent clutter sources in each of these ambiguous ranges. As ground clutter is distributed in range over a region extending to radar horizon, range ambiguities could occur if radar's range horizon (R_h) extends beyond its unambiguous range (R_{ua}). Thus, if $R_{ua} < R_h$, then clutter contribution from multiple ranges will appear in the CUT. The range of the 3D data cube's range bins is limited to between h_R and R_{ua} to restrict the range. However, in general, clutter contribution in terms of clutter to noise ratio (CNR) decreases by a factor of R^3 as R increases; hence, contributions from these farther range ambiguities are generally insignificant. Similarly, α_{ik} and $\mathbf{v}(\vartheta_{ik}, \bar{\omega}_{ik})$ are the amplitude and the space-time steering vector of the ik^{th} clutter patch. The random amplitude of the ik^{th} clutter patch satisfies the following through assuming clutter returns are uncorrelated [1].

$$E\{|\alpha_{ik}|^2\} = \sigma^2 \xi_{ik}. \tag{2.15}$$

CNR of the ik^{th} clutter patch, ξ_{ik}, is expressed using bistatic version of the radar

range equation as follows [1, 2, 37]

$$\xi_{_{ik}} = \frac{P_T G_T(\theta_{T_{ik}}, \phi_{T_{ik}}) g_R(\theta_{R_{ik}}, \phi_{R_{ik}}) \lambda^2 \sigma_{ik}}{(4\pi)^3 \sigma^2 L_T L_R R_{T_{ik}}^2 R_{R_{ik}}^2}, \tag{2.16}$$

where:

- P_T is the peak transmit power assigned as 1000 W for all experiments of this research,
- G_T is the transmitter gain which is a function of transmitter elevation and azimuth,
- θ_T and ϕ_T are the angles to the ik^{th} clutter patch,
- g_R is the gain of each receiver element which is also a function of receiver element's elevation and azimuth to the ik^{th} patch, (θ_R,ϕ_R),
- σ_{ik} is the bistatic radar cross-section (RCS) of the ik^{th} clutter patch,
- σ^2 is the noise power fixed at 1 W,
- L_T and L_R are the system losses of transmitter and receiver respectively,
- $R_{R_{ik}}$ is the range from receiver to the ik^{th} clutter patch, and
- $R_{T_{ik}}$ is the range from transmitter to the ik^{th} clutter patch

The bistatic RCS of the he ik^{th} clutter patch is calculated as [37]

$$\sigma_{ik} = A_{ik}\, \sigma_0(\theta_I, \theta_S, \phi_{OP}), \tag{2.17}$$

where A_{ik} is the area of the ik^{th} clutter patch, and σ_0 is the normalized RCS coefficient.

Lievsay adopted an interpolation model based on the measured responses from Willis [47] generated as a function of clutter patch coordinate parameters – a combination of in-plane and out-of-plane (IPOP) ground clutter patch angles θ_I, θ_S and ϕ_{OP} [37] as hihglighted in Figure 2.10 [47]. The strongest RCS reflectivity was observed when the out-of-plane angle is at its extreme bounds at either 0° or 180°. Conversely, the weakest reflectivity was at $\phi_{OP} = 90°$. Refer to [37] and [47] for detailed analysis of clutter patch RCS modeling and measurements. Finally, this research uses the method outlined in [37] to calculate A_{ik}, which employs a four-sided polygon to approximate the patch area.

Assuming returns from independent clutter patches of the same range bin are uncorrelated, the space-time clutter covariance matrix can be expressed as

$$\mathbf{R}_c = E\left[\boldsymbol{\chi}_c \boldsymbol{\chi}_c^{\mathsf{H}}\right] = \sigma^2 \sum_{i=1}^{N_c} \xi_{ik} \mathbf{v}_{ik} \mathbf{v}_{ik}^{\mathsf{H}}, \tag{2.18}$$

where ξ_{ik} is the CNR contribution of the ik^{th} clutter patch, and σ^2 is the noise power component. Thus, $\mathbf{R}_c$ is a $MN \times MN$, block toeplitz matrix. For the range

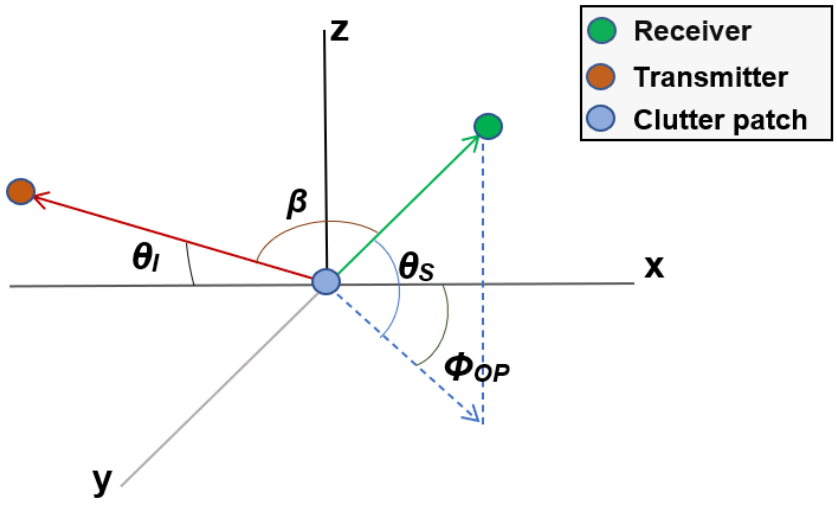

Figure 2.10: Bistatic clutter geometry showing the IPOP angles. This geometry is based on the coordinate system described in [47].

unambiguous case ($N_r = 1$) $\mathbf{R}_c$ can be compactly expressed as

$$\mathbf{R}_c = \mathbf{V}_c \, \mathbf{\Xi}_c \, \mathbf{V}_c^{\mathsf{H}}, \tag{2.19}$$

where $\mathbf{\Xi}_c$ is the $N_c \times N_c$ clutter power contribution diagonal matrix, and $\mathbf{V}_c$ is the $MN \times N_c$ matrix of space-time steering vector of all clutter patches in the CUT.

As per earlier discussions, the LTE waveforms are considered to be non-ideal radar waveforms due to high range sidelobes and pulse diversity. These pulse-diverse waveforms result in poor clutter filtering due to pulse-to-pulse decorrelation of the range sidelobes [37]. Hence, in order to model the de-correlation over slow time due to pulse-diverse LTE waveform, a covariance matrix taper (CMT) is applied to the clutter covariance matrix calculated in (2.18) [2, 37]. Lievsay demonstrated that pulse diverse waveforms cause clutter Doppler spreading, thus applied a CMT to $\mathbf{R}_c$ to model the interference subspace leakage [37]. Application of CMT modifies $\mathbf{R}_c$ as per below

$$\mathbf{R}_c = \int \mathbf{T}(\tau - \tau_0) \odot \mathbf{R}_c \, d\tau, \tag{2.20}$$

where $\mathbf{R}_{c,\tau}$ is the clutter covariance matrix evaluated at delay τ, and $\mathbf{T}(\tau - \tau_0)$ is the CMT.

2.5.4 Intrinsic Clutter Motion

The clutter model outlined in 2.5.3 assumes the clutter patch echoes do not fluctuate between pulses. However, in practice clutter echoes can fluctuate between pulses. This fluctuation is typically due to natural variation in clutter reflectivity due to wind and other climatic factors [48]. This pulse-to-pulse variation in clutter reflectively is referred to as intrinsic clutter motion (ICM). Two separate models will be used to simulate the effects of ICM in this research. Brief outlines of each of these methods

are provided in 2.5.4.1 and 2.5.4.2.

2.5.4.1 ICM Model - Method 1

ICM Method 1 is based on the description provided by Ward in [1]. This approach uses standard deviation of the clutter velocity to model the temporal amplitude variations. The clutter space-time snapshot in (2.14) can be alternatively expressed as

$$\boldsymbol{\chi}_c = (\boldsymbol{\alpha}_k \odot \mathbf{b}_k) \otimes \mathbf{a}_k, \tag{2.21}$$

where $\boldsymbol{\alpha}_k$ represents the $M \times 1$ vector of random amplitudes. The temporal fluctuation causing these random amplitude variations can be modelled as a wide-sense stationary random process whose autocorrelation function is

$$\gamma_k(m) \triangleq E\{\alpha_{l+m}\alpha_l^*\} = \sigma^2\, \boldsymbol{\xi}_k \exp\left\{ \frac{-\,(4\pi\, \sigma_v\, T_r)^2}{2\,\lambda_o^2}\, m^2 \right\}, \tag{2.22}$$

where σ_v is the velocity standard deviation of the ICM [1]. It is assumed that all clutter patches have the same intrinsic velocity spectrum. Hence, a single σ_v is used to model ICM in each simulation. Typical values of σ_v were measured for various altitudes and tabulated in [49]. A small number of σ_v values will be chosen within the range of $0.25 - 2\,\mathrm{m/s}$, to simulate clutter motion from weather at altitudes below $12,000$ ft [49].

Finally, the clutter covariance matrix in presence of ICM is given by

$$\mathbf{R}_c = \sum_{k=1}^{N_c} (\boldsymbol{\Gamma}_k \odot \mathbf{b}_k \mathbf{b}_k^{\mathsf{H}}) \otimes \mathbf{a}_k \mathbf{a}_k^{\mathsf{H}}, \tag{2.23}$$

where,

$$\boldsymbol{\Gamma}_k = \mathrm{Toeplitz}(\gamma_k(0); ...; \gamma_k(M-1)), \tag{2.24}$$

is the $M \times M$ covariance matrix of the k^{th} patch fluctuations. Presence of ICM will broaden the clutter ridge indicated through widening of the clutter notch in corresponding SINR_L curves. This widening effect is due to the increase in the rank of the clutter covariance matrix [50], which ultimately requires more adaptive DoF to suppress the clutter returns. Section 4.5.1 and will analyze these effects through simulation results in detail.

2.5.4.2 ICM Model - Method 2

The Billingsley model documented in [41, 48] is adopted as the second method to model ICM in this research. This model is a product of an extensive research conducted by Billingsley at MIT Lincoln Laboratory. Unlike Method 1, this method accepts the wind speed as an input parameter instead of its standard deviation. Both methods follow a similar exponential model with operating wavelength as a common input parameter. The clutter Doppler power spectral density (PSD) of Method 2, $P_c(f)$, is expressed as [48]

$$P_c(f) = \frac{r}{r+1}\,\delta(f) + \frac{1}{r+1}\,\frac{b\lambda}{4}\exp\Big\{-\frac{b\lambda}{2}\,|f|\,\Big\}, \tag{2.25}$$

where f is the Doppler frequency in Hz, $\delta(\cdot)$ is the Dirac delta function, b is the shape parameter that depends on wind conditions as tabulated in [41], and r is the ratio between the first and second terms of (2.25). The ratio, r, can be expressed as a function in terms of wind speed, v_c, and carrier frequency, f_c, as shown below [41,48].

$$10\log r = -15.5\log w - 12.1\log f_c + 63.2 \tag{2.26}$$

Inverse Fourier transform of (2.25) results in the following temporal correlation

function

$$r_c(\tau) = \int_{-\infty}^{\infty} P_c(f) \exp\{j2\pi f\tau\} = \frac{r}{r+1} + \frac{1}{r+1} \frac{(b\lambda)^2}{(b\lambda)^2 + (4\pi\tau)^2}. \tag{2.27}$$

Finally, the ICM taper corresponding to this ICM model is obtained by sampling $r_c(\tau)$ given in (2.27) at multiples of PRI [48]. The resulting $M \times 1$ temporal taper vector can be expressed as

$$T_{\text{ICM}} = r_c(0 : M-1). \tag{2.28}$$

Applying the ICM taper in (2.28) to temporal steering clutter vector results in the following clutter space-time snapshot.

$$\boldsymbol{\chi}_c = \sigma^2 \boldsymbol{\xi}_k \cdot (T_{\text{ICM}} \odot \mathbf{b}_k) \otimes \mathbf{a}_k \tag{2.29}$$

Similarly, its corresponding clutter covariance matrix can be expressed as,

$$\mathbf{R}_c = \sigma^2 \sum_{k=1}^{N_c} \boldsymbol{\xi}_k (\mathbf{T}_k \odot \mathbf{b}_k \mathbf{b}_k^{\mathsf{H}}) \otimes \mathbf{a}_k \mathbf{a}_k^{\mathsf{H}}, \tag{2.30}$$

where

$$\mathbf{T}_k = \text{Toeplitz}\left(T_{\text{ICM}}(0); ...; T_{\text{ICM}}(M-1)\right), \tag{2.31}$$

is the $M \times M$ covariance matrix of the k^{th} patch fluctuations.

Similar to the ICM model outlined in 2.5.4.1, the Billingsley model in Method 2 is also expected to widen the clutter notches of SINR_{L} curves with increase in v_c. Section 4.5.2 and will analyze these effects through simulation results in detail. Finally, ICM Method 2 assumes the clutter motion to be constant at a given wind speed while ICM Method 1 models clutter with varying motion and wind speeds, but with constant standard deviation. Hence on the concept level Method 1 appears to

be a more practically representative model in comparison to Method 2. However, this thesis research did not seek investigate or validate the superior of these two ICM models.

2.5.5 Noise Signal Modeling

Noise is the simplest of the three undesired signal sources to model as it is uncorrelated in both space and time. This assumption leads to the following $MN \times MN$ space-time noise covariance matrix

$$\mathbf{R}_n = E\left[\boldsymbol{\chi}_n \boldsymbol{\chi}_n^{\mathsf{H}}\right] = \sigma^2 \mathbf{I}_M \otimes \mathbf{I}_N = \sigma^2 \mathbf{I}_{MN}, \tag{2.32}$$

where σ^2 is the noise power. As these individual undesired components are independent of each other, the interference plus noise covariance matrix is given by

$$\mathbf{R}_u = E\left[\boldsymbol{\chi}_u \boldsymbol{\chi}_u^{\mathsf{H}}\right] = \mathbf{R}_c + \mathbf{R}_n. \tag{2.33}$$

2.5.6 STAP Data Processing

In a broad sense, STAP involves adaptively adjusting a two-dimensional space-time filter response in an attempt to maximize the filter's output SINR. Consequently, this improves detection performance through suppressing the undesired signal returns such as correlated clutter sources, and uncorrelated noise sources [39]. An optimum matched filter response is obtained through applying a set of weights, $\mathbf{w}$, to the vectorized space-time samples, $\boldsymbol{\chi}$, at the range CUT. The space-time processor applies this weight vector to the received space-time snapshot data to provide coherent gain on target while forming angle and Doppler response nulls to suppress clutter and jamming [1]. The application of $\mathbf{w}$ to the space-time snapshot results in the scalar test statistic y. This test statistic output from the square-law detector at each angle-

Doppler $(\vartheta, \bar{\omega})$ coordinate pair is expressed as, (also shown in Figure 2.9)

$$y(\vartheta, \bar{\omega}) = |\mathbf{w}^{\mathsf{H}} \boldsymbol{\chi}|^2, \tag{2.34}$$

which is compared against a predetermined threshold for target detection.

The optimum filter to maximize the SINR is given as [17]

$$\mathbf{w}_{\mathrm{o}}(\vartheta, \bar{\omega}) = \kappa\, \mathbf{R}_u^{-1} \mathbf{v}(\vartheta, \bar{\omega}), \tag{2.35}$$

where κ is an arbitrary scale factor, that does not affect the SINR performance. Defining κ as shown below will enable $\mathrm{y}(\vartheta, \bar{\omega})$, to display constant false alarm rate (CFAR) behavior.

$$\kappa = \frac{1}{\sqrt{\mathbf{v}^{\mathsf{H}} \mathbf{R}_u^{-1} \mathbf{v}}} \tag{2.36}$$

A single space-time weight vector is optimized for a specific angle and Doppler pair as shown in (2.35). However, in practice the interference covariance matrix must be estimated. The sample matrix inversion (SMI) approach is adopted to estimate $\mathbf{R}_u$ from training data. A finite amount of training data is collected over the CPI data to estimate $\mathbf{R}_u$ as

$$\hat{\mathbf{R}}_u = \frac{1}{L_s} \sum_{l}^{L_s} \boldsymbol{\chi}_l \boldsymbol{\chi}_l^{\mathsf{H}}. \tag{2.37}$$

The training data contains L_s number of range bins whose length is generally dependent on the degrees of freedom (DoF) offered by the radar system. In a stationary clutter environment, $2 \times$ DoF training data snapshots are necessary to achieve to achieve an average performance loss of 3 dB [51, 52]. Most importantly, the training data is void of CUT's space-time snapshot and potentially adjacent guard band cells as well (see Figure 2.11). Thus, $\frac{L_s}{2}$ number of range bins from either side of the CUT are combined to form the training data as shown in Figure 2.11. These training

space-time snapshots, $\boldsymbol{\chi}_l$, are used in (2.37) to estimate $\mathbf{R}_u$. Incorporating (2.37) into (2.35) generates the following practical filter[1]

$$\mathbf{w}(\vartheta, \bar{\omega}) = \hat{\kappa}\, \hat{\mathbf{R}}_u^{-1} \mathbf{v}(\vartheta, \bar{\omega}). \tag{2.38}$$

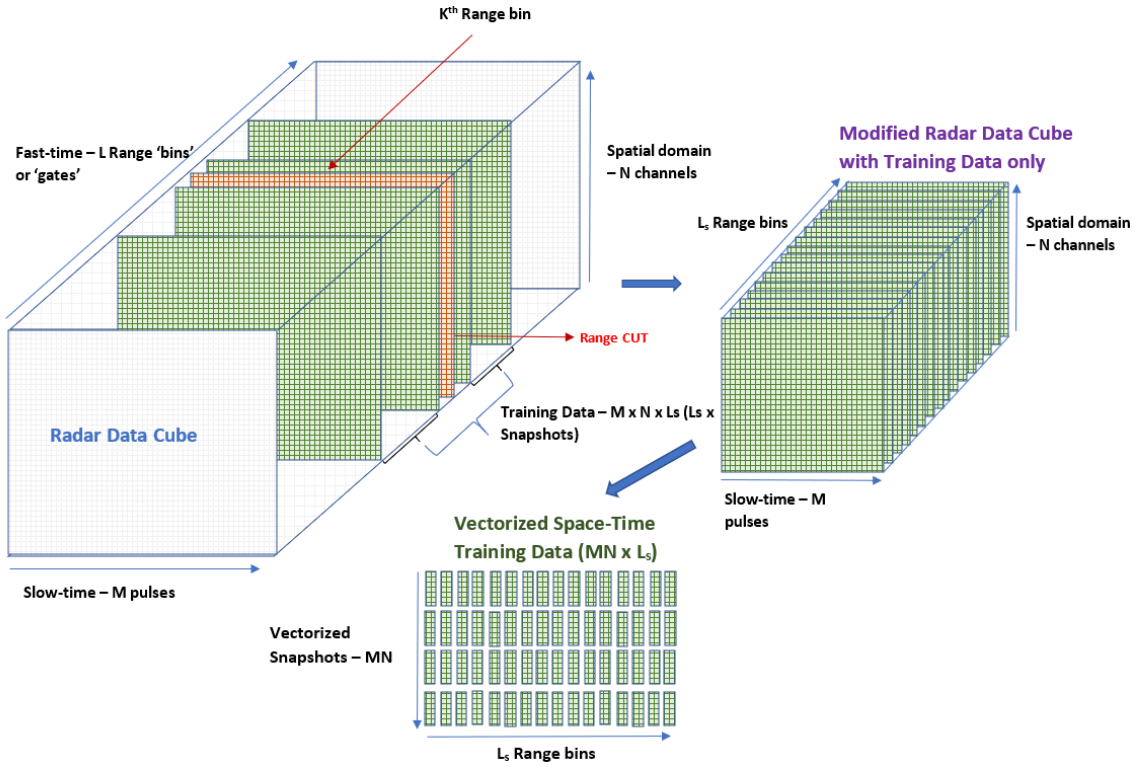

Figure 2.11: Training data containing space-time snapshots corresponding to range bins of length of L_s located on either side of the CUT are grouped. Once grouped, snapshot matrices in this data are vectorized, each forming a $MN \times 1$ column vector. L_s of these column vectors spanning the total length of the training data are grouped together to form a space-time snapshot training matrix, $\boldsymbol{\chi}$ of size $MN \times L_s$.

[1]New training data need to be captured for each CUT to calculate specific $\hat{\mathbf{R}}_u$ and $\mathbf{w}$.

2.5.7 SINR Performance Metrics

SINR is the ratio of the output power of the signal versus the output power of the interference-plus-noise, expressed as

$$\text{SINR} = \frac{P_S}{P_I + P_N} = \sigma^2 \xi_t \frac{|\mathbf{w}^{\mathsf{H}}\mathbf{v}|^2}{\mathbf{w}^{\mathsf{H}}\mathbf{R}_u\mathbf{w}}, \tag{2.39}$$

where ξ_t is the SNR at one channel and one pulse. The optimal SINR is calculated by substituting space-time optimum weight vector from (2.35) into (2.39), resulting in

$$\text{SINR}_{\text{o}} = \sigma^2 \xi_t \mathbf{v}^{\mathsf{H}}\mathbf{R}_u^{-1}\mathbf{v}, \tag{2.40}$$

whereas the SINR due to SMI is calculated by substituting (2.38) into (2.39) shown as

$$\text{SINR} = \sigma^2 \xi_t \frac{|\mathbf{v}^{\mathsf{H}}\hat{\mathbf{R}}_u^{-1}\mathbf{v}|^2}{\mathbf{v}^{\mathsf{H}}\hat{\mathbf{R}}_u^{-1}\mathbf{R}_u\hat{\mathbf{R}}_u^{-1}\mathbf{v}}. \tag{2.41}$$

It can also be useful to express SINR as a relative metric with SINR Loss. The two versions of SINR Loss are defined as [1]

$$\text{SINR}_{\text{L,o}} = \frac{\text{SINR}_{\text{o}}}{\text{SNR}} = \frac{\text{SINR}_{\text{o}}}{\xi_t NM} \tag{2.42}$$

$$\text{SINR}_{\text{L}} = \frac{\text{SINR}}{\text{SNR}} = \frac{\text{SINR}}{\xi_t NM} \tag{2.43}$$

These ratio of ratios metrics remove the influence of signal and noise so the impacts from algorithms, waveforms, and estimation techniques can be analyzed. The metrics in (2.42) and (2.43) are the the primary ones used in this research.

2.6 Partially Adaptive STAP

Thus far, this report has described the application of STAP as a 2D adaptive filter operating on M pulses and N channels [17], commonly referred to as fully adaptive STAP or FD-STAP. This section will introduce two alternate STAP techniques commonly used in practical applications to mitigate the FD-STAP limitations, such as excessive computational processing requirements and limited availability of suitable training data. While reducing the DoF could be used as a mitigation strategy against these limitations, doing so degrades the performance due to reduction in space-time aperture [17]. Hence, alternate STAP techniques, implemented either through reduction in STAP processor's dimensionality or application of low-rank interference covariance matrix approximation, are introduced in this section. RD-STAP transforms the original set of received signals to a relatively small subset to solve a reduced-dimension adaptive filtering problem [1]. This research focuses solely on RD-STAP techniques for its partially adaptive STAP analysis. Reduced rank STAP (RR-STAP), which focuses on improving the statistical convergence through employing data-dependent transformations will not be analyzed in detail as part of this research.

2.6.1 RD-STAP Concept Overview

RD-STAP relies on reducing STAP processor's dimensionality in terms of number of pulses or channels to reduce the computational and training data burden imposed on the system. This technique applies data independent transformations to pre-filter the data and reduce the number of adaptive DoF [17]. RD-STAP projects the space-time snapshot, $\boldsymbol{\chi}$, to reduced dimensions by applying linear transformations resulting in the following transformed vector of reduced dimensions

$$\tilde{\boldsymbol{\chi}} = \mathbf{T}^{\mathsf{H}}\boldsymbol{\chi}, \tag{2.44}$$

where the transformation matrix, $\mathbf{T} \in NM \times K$, yields the transformed space-time snapshot, $\tilde{\boldsymbol{\chi}}$ of reduced dimensions $K \times 1$. K is chosen such that $K \ll NM$. Applying the same transformation to the space-time steering vector in (2.11) gives

$$\tilde{\mathbf{v}} = \mathbf{T}^{\mathsf{H}}\mathbf{v}(\vartheta, \bar{\omega}). \tag{2.45}$$

The corresponding optimal RD-STAP weight vector for this transformed data with reduced dimensions space-time interference covariance matrix, $\tilde{\mathbf{R}} \in K \times K$ is expressed in (2.46a). The adaptive solution involves estimating $\hat{\tilde{\mathbf{R}}}$ from (2.37) using transformed training dataset of reduced length. Applying the transformed steering vector, $\tilde{\mathbf{v}}$, to $\hat{\tilde{\mathbf{R}}}$ yields the practical RD-STAP weight vector in (2.46b) [17, 39].

$$\tilde{\mathbf{w}}_{\mathrm{o}} = \tilde{\mathbf{R}}^{-1}\tilde{\mathbf{v}} \tag{2.46a}$$

$$\tilde{\mathbf{w}} = \hat{\tilde{\mathbf{R}}}^{-1}\tilde{\mathbf{v}} \tag{2.46b}$$

The transformation matrix, $\mathbf{T}$, can be chosen from one of the beam/element-space – pre/post-Doppler combinations detailed in the following subsection.

2.6.2 RD-STAP Algorithms

Combinations of temporal and spatial filtering of the received sampled data determine the type of transform to be used. Figure 2.12 shows a typical taxonomy of RD-STAP algorithms, classified by the non-adaptive filtering transformations applied to the CPI data samples. CPI data with nil transformation is represented by the top-left quadrant of Figure 2.12, which relates to FD-STAP discussed earlier. Filtering in their respective domains prior to adaptation will result in either beam-space pre-Doppler or element-space post-Doppler as shown in the bottom-left and top-right quadrants of Figure 2.12. Spatial filtering, also known as beamforming, is performed

on each PRI to reduce the DoF in spatial nulling and angle estimation applications and to transform the space-time snapshot data to angle beam-by-PRI data [1]. These pre-Doppler classes of algorithms are generally referred to as displaced phase center antenna (DPCA) and discussed in detail within [1, 39].

Similarly, temporal filtering commonly known as Doppler processing is performed on each channel prior to adaptive processing, transforming the space-time snapshot into space-Doppler snapshot. Doppler filtering can isolate the clutter interference to the angular regions of the clutter ridge corresponding to the Doppler filter mainlobe; thus reducing the number of adaptive DoF required in post-Doppler processing. Extended factored algorithm (EFA) is a specific variant of element-space post-Doppler filtering analyzed in this research. A brief introduction of EFA is provided in 2.6.3.

Finally, performing both spatial and temporal filtering prior to adaptation, known as beam-space post-Doppler algorithm, is depicted in the bottom right quadrant of Figure 2.12. A common example of this class of algorithm is to perform 2D discrete Fourier transform (DFT) of the CPI data as shown in Figure 2.12. Using this approach, interference is localized both temporally and spatially, allowing a smaller subset of transformed data to be adaptively processed [1]. Joint domain localized (JDL) algorithm is a specific variant of beam-space post-Doppler filtering analyzed in this research. A brief introduction of JDL is provided in 2.6.4.

2.6.3 Extended factored algorithm (EFA)

EFA is an element-space post-Doppler class of RD-STAP algorithm that uses both temporal tapering and filtering to reduce the dimension of the space-time data. EFA applies one-dimensional DFT of length M, to the windowed PRI data of each channel. This transforms the data from the space-time to space-Doppler domain. Using correlation reduction property of frequency domain, an odd number of Doppler

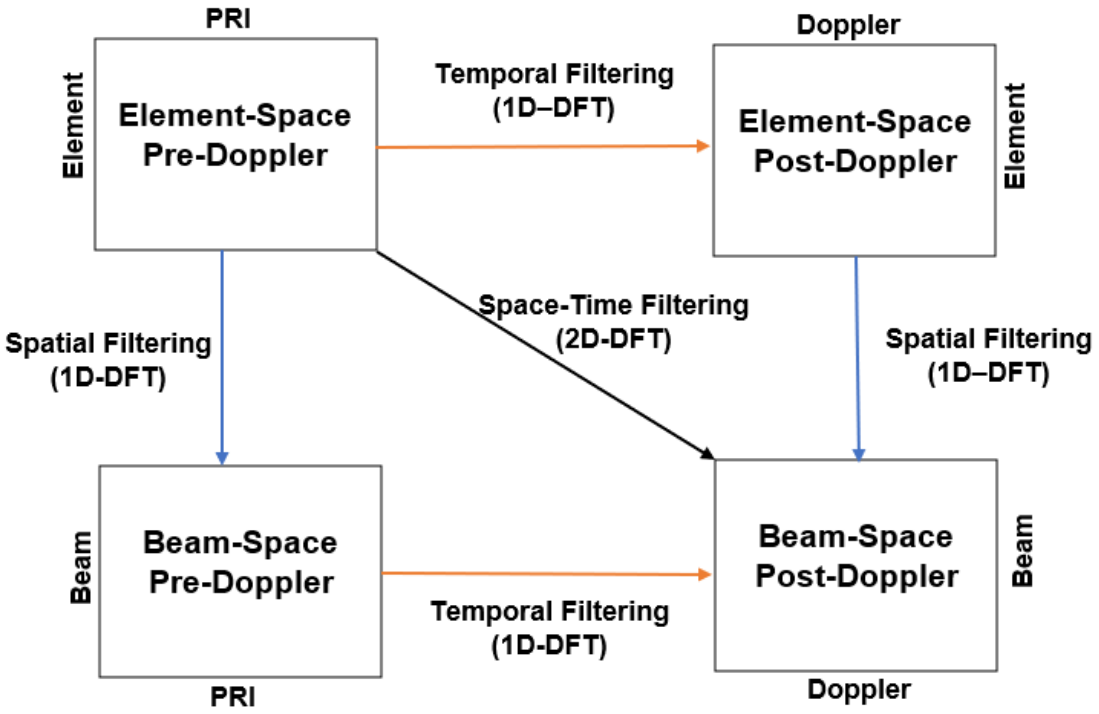

Figure 2.12: Various types of RD-STAP algorithms classified based on the type transformation filtering applied to the CPI data prior to adaptive processing [1].

bins is selected such that the central bin corresponds to the frequency response peak with remaining bins corresponding to the adjacent bins on either side of it. DiPierto discusses EFA in elaborate detail in [29] with specific derivations and theoretical basis. An order 2 EFA, that extracts the central and one adjacent Doppler bin on its either side, requires training data of length $2 \times \text{DoF} = 2 \times (3 \times N) = 6N$, which is considerably less than the minimum data requirement of the FD-STAP scenario of $2 \times MN$. Furthermore, the matched apodized Doppler weight vector can be pre-calculated as it is shift-invariant in the frequency domain, which further reduces the computational requirement [37]. Similarly, an order 2 EFA, requires M number of $\tilde{\mathbf{R}}$ matrices of size $3N \times 3N$ to be calculated across each spatial channel. Thus the overall computations required for an order 2 EFA is $M \times [N \times ((2 \times \text{Order}) - 1)]^3 = M(3N)^3$, which is significantly smaller than FD-STAP's overall computational requirement of

$(MN)^3$ – reduction by a factor of $M^2/27$. Thus, an order 2 EFA enables reduction in both training data and computational requirements by a factor of $M/3$ and $M^2/27$ respectively with minimal performance loss as stated in [29]. A typical process flow of an order 2 EFA is shown in Figure 2.13.

2.6.4 Joint domain localized (JDL) Algorithm

JDL is a beamspace post-Doppler class of RD-STAP algorithm that transforms the received data from space-time to angle-Doppler domain prior to applying adaptive filtering. Unlike EFA, a 2D DFT is applied together on both spatial and temporal components of the space-time vector in JDL to transform it to angle-Doppler domain [30]. Once transformed, the angle-Doppler bin data grouped into L number of localized processing regions LPRs, each comprised of M_d Doppler bins and N_b angle/-

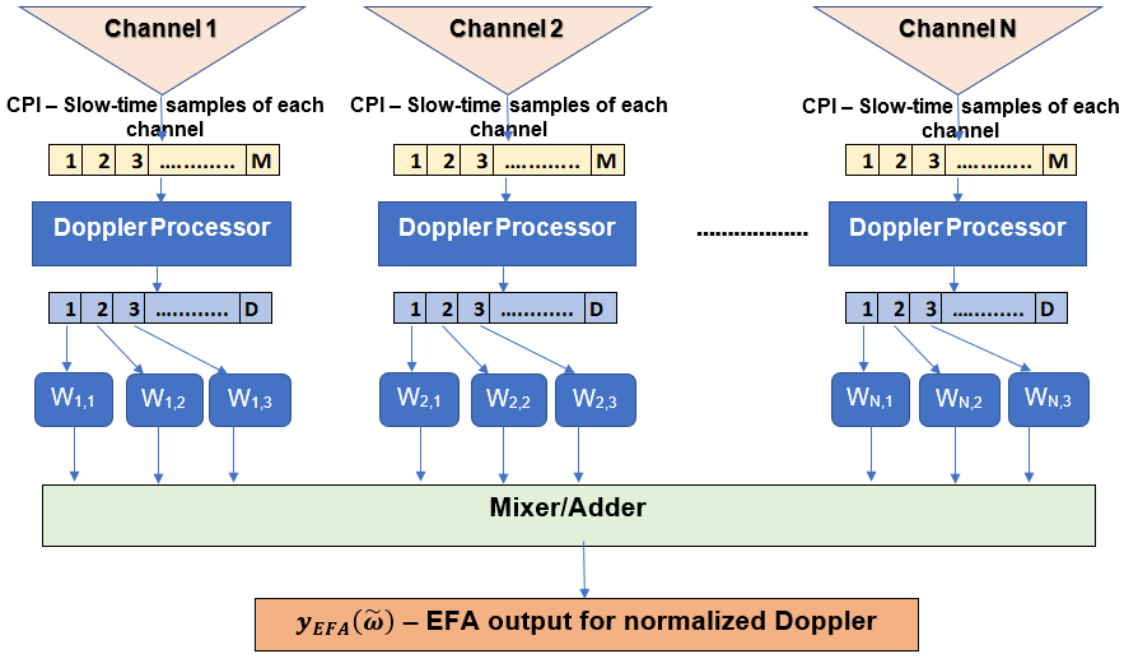

Figure 2.13: An Order 2 EFA process flow for an N channel array that received M pulses in a CPI. The adaptive weights shown in the figure represents $\mathbf{w}_{n,d}$, where n corresponds to the channel and d corresponds to a specific Doppler bin.

beam bins. M_d and N_b are chosen to be odd numbers and are smaller than the M and N respectively. LPRs of size $[3 \times 3]$ or $[5 \times 5]$ are generally adopted to reduce the overall dimensionality of the adaptive processing [53]. Figure 2.14 demonstrates the JDL implementation using LPRs of size $[3 \times 3]$ for a system with 11 pulses and 11 receiver channels ($[11 \times 11]$). The angle bins chosen to form each LPR are centered around the look-direction of the antenna array corresponding to 0° [30,53]. However, due to distribution of clutter in Doppler, each Doppler bins have to tested. Hence, the number of LPRs is equal to total number of pulses or Doppler bins, with Doppler bin being tested is centred within the LPR. Both Ong [30], and Wang and Cai [53] describe the background, derivation and mathematical model of JDL in detail. A typical process flow of JDL is shown in Figure 2.15 [1].

Similar to EFA, JDL is also employed to reduce the computational and sample support burden of FD-STAP. But unlike EFA that reduces DoF only in the Doppler domain, JDL enables DoF reduction in both angle and Doppler domains by choosing

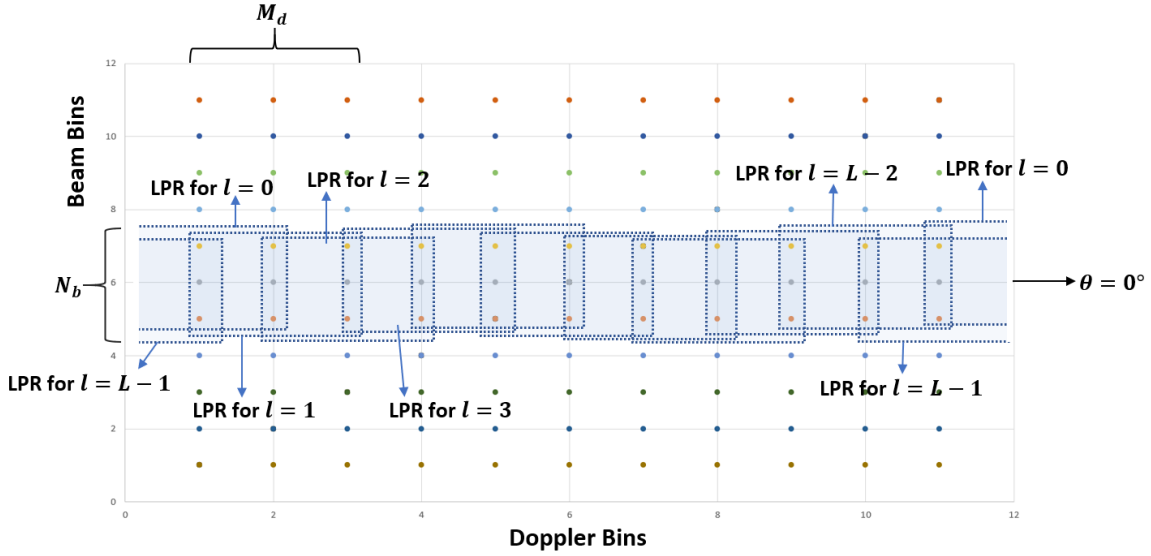

Figure 2.14: An example of LPR layout of a $[3 \times 3]$ JDL algorithm implemented on a $[11 \times 11]$ space-time system. The LPRs are clearly shown to be centred around the look-drection of the receiver antenna at 0°. A total of L LPRs are shown with $l = 0$ corresponding to the first LPR, while $l = L - 1$ corresponds to the last LPR.

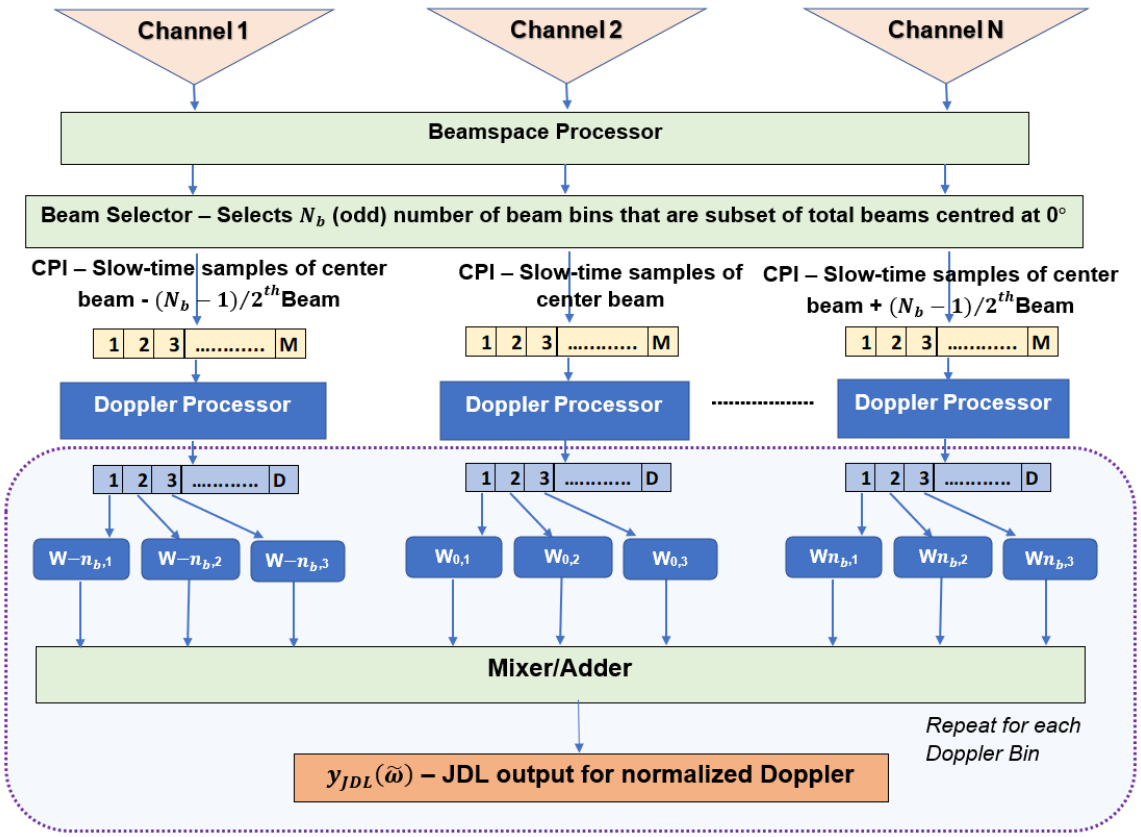

Figure 2.15: JDL algorithm process flow for an N channel array that received M pulses in a CPI. N_b number of angle bins are selected from the output of the beamspace processor, centred at (0°).The adaptive weights shown in the figure represents $\mathbf{w}_{n_b,m_d}$, where n_b and m_d corresponds to a specific angle and Doppler bin.

a subset of the available bins in the respective domains to form LPR prior to adaptive filtering. Thus, the training data requirement of a $[3 \times 3]$ JDL reduces to 18 $(2 \times 3 \times 3)$ from 242 $(2 \times 11 \times 11)$ for the scenario shown in Figure 2.14. Similarly, the computations required reduce to $11 \times 11 \times (3 \times 3)^3 = 8.82 \times 10^4$ from $(11 \times 11)^3 = 1.77 \times 10^6$ for FD-STAP and $11 \times (11 \times 3)^3 = 3.95 \times 10^5$ for an Order 2 EFA. This comparison clearly shows the considerable reduction in the computation time between JDL, FD-STAP, and EFA. Thus JDL experiments are expected to be executed N^2/N_b^3 times faster than EFA experiments. This reduction in training data requirement, while yielding reduction in processing time required, may increase the SINR loss

compared to EFA due to smaller DoF and training data available to suppress the interference sources. Chapter IV will analyze this trade-off in detail.

2.7 Passive Bistatic Radar (PBR)

Bistatic radars transmit and receive from two separate locations [54]. PBR, a specific case of bistatic radar, operates only in receive-mode relying on stationary emitters of opportunity for target detection. Bistatic radar offers both advantages and shortfalls against monostatic radars. One such advantage is that targets can be viewed from different angles enabling low-observable targets to be detected, as target RCS varies with bistatic angle (β). Transmitter signal is also received directly at the receiver, potentially inducing interference masking weaker target returns [55]. Similarly, PBR also has both benefits and shortfalls: As a receive only system, PBR does not have to compete for bandwidth in a frequency congested environment. Conversely, due to dependence on non-cooperative emitters of opportunity, the resulting signal processing can be more challenging when compared to monostatic or general bistatic scenarios.

2.7.1 Passive Bistatic Geometry

The basic bistatic geometry shown in Figure 2.16 is described using a 2D North-reference coordinate system discussed in [47, 54]. This basic geometry assumes that the transmitter and the receiver are positioned at the same altitude within the bistatic plane. A brief overview of this basic bistatic geometry is as follows. The bistatic baseline, L, is the distance between the transmitter and the receiver. Similarly, the bistatic range, R_B, is the sum of the distances between target and transmitter (R_T), and target and receiver (R_R), i.e., $R_B = R_T + R_R$. Constant R_B generates elliptical isorange contours within the bistatic plane as shown in Figure 2.16. These

isorange contours represent constant propagation delay from all ground scatterers that lie on this isorange contour [37]. Conversely, extending this to the 3D PBR geometry, depicted in Figure 2.17, creates a prolate spheroid where the surface defines a constant bistatic range. This prolate spheroid (ellipsoid) is formed by revolving the 2D geometry's isorange contour ellipse about its major axis [37] whose foci are represented by the transmitter and receiver. The intersection of the ground plane ($x-y$ plane) and this ellipsoid produces ellipses of constant bistatic range, as shown in Figure 2.16 [54]. Finally, the bistatic angle, is the angle between the transmitter and receiver with its vertex at the target as shown in Figure 2.16.

The geometry of the PBR model considered in this research cannot be described using the basic bistatic geometry in Figure 2.16 due to altitude variations between

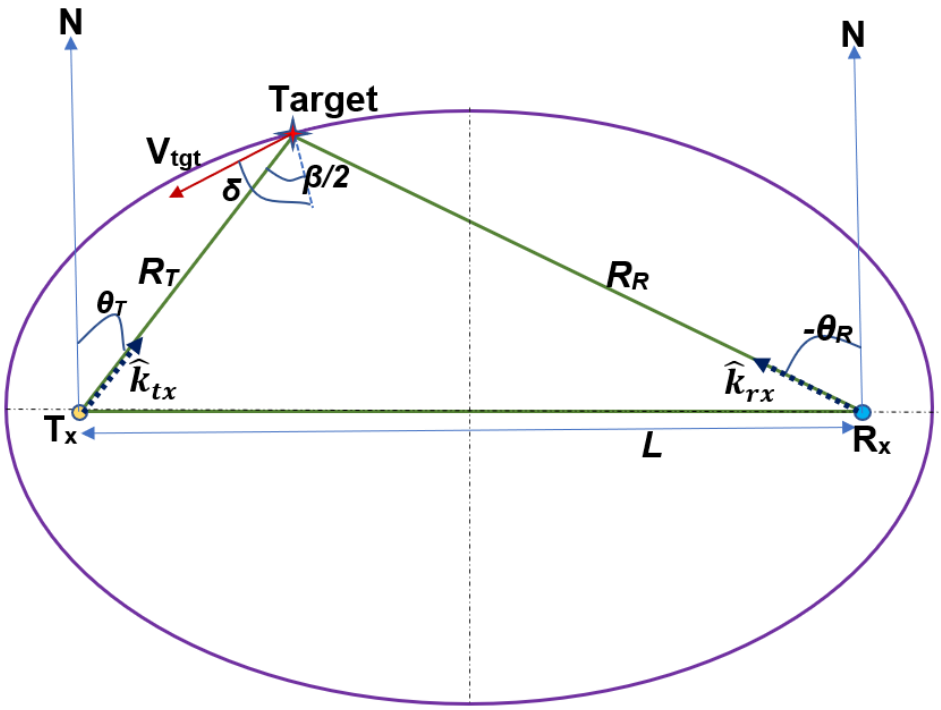

Figure 2.16: A typical passive bistatic geometry with North-referenced coordinate system [47].

the transmitter and the receiver. Instead, a 3D geometry shown in Figure 2.17 is adopted to describe the PBR geometry. The receiver system is assumed to be a ULA mounted on an airborne platform travelling at v_{rx} along the y-axis at h_R meters above the ground plane. Conversely, the LTE transmitter is assumed to be stationary at $(L\cos\theta_T\cos\phi_T, L\cos\theta_T\sin\phi_T, h_T)$, such that $h_R > h_T$ [37]. The bistatic baseline, L, is expressed as $|\frac{h_R - h_T}{\sin\theta_T}|$ in the 3D PBR geometry. Assuming a flat earth model, the grazing angle can be treated as the elevation angle, θ_T, between the transmitter and receiver. Furthermore, θ_T is defined as negative. The angle between the transmitter and the receiver in the ground plane is defined as azimuth angle, ϕ_T, where 0° and 90° corresponds to the x and y axis respectively. The PBR model simulated in this research assumes the transmitter lies on the x-axis with $\phi_T = 0°$. Other specific parameters chosen to model this PBR geometry are detailed in Section 3.3.

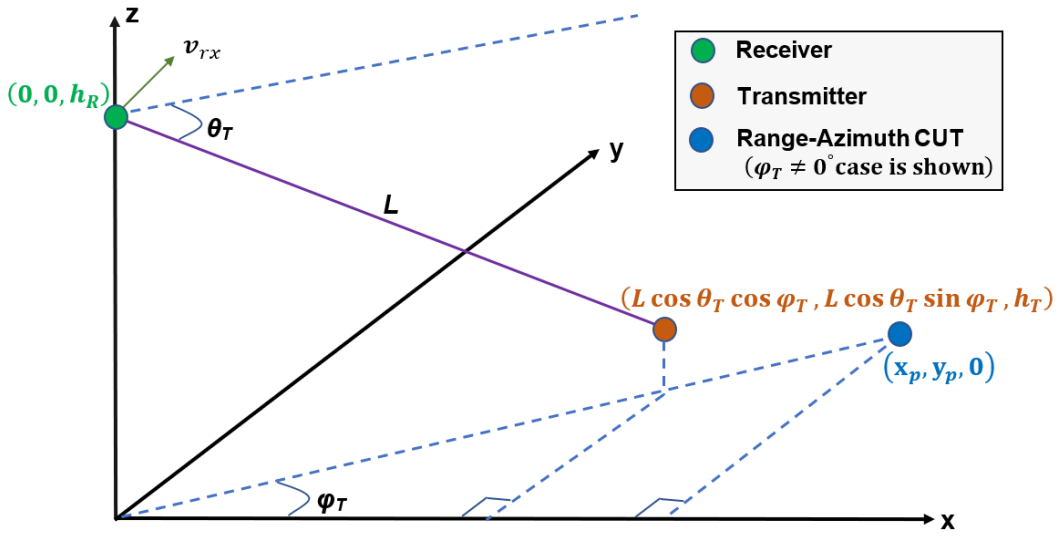

Figure 2.17: A typical passive bistatic geometry with North-referenced coordinate system [47].

2.7.2 Passive STAP Clutter

The airborne platform of the PBR system defined in this research induces a Doppler shift on the clutter that extends in both range and angle [37]. Conversely, the stationary LTE transmitter does not induce a Doppler shift on the clutter. Thus, in a passive system the resulting Doppler shift is half of the shift seen in a monostatic system while keeping v_{rx} and λ constant. Induced Doppler shift is defined as

$$f_d = \frac{\hat{\mathbf{k}}_{tx} \cdot \mathbf{v}_{tx} + \hat{\mathbf{k}}_{rx} \cdot \mathbf{v}_{rx}}{\lambda}, \tag{2.47}$$

where $\hat{\mathbf{k}}_{tx}$ and $\hat{\mathbf{k}}_{rx}$ are the unit vectors pointing to the target from the transmitter and receiver respectively (see Figure 2.16) and $\mathbf{v}_{tx}$ and $\mathbf{v}_{rx}$ are the transmitter and receiver velocity vectors in the 3D space. The stationarity of the transmitter reduces (2.47) to

$$f_d = \frac{\hat{\mathbf{k}}_{rx} \cdot \mathbf{v}_{rx}}{\lambda}, \tag{2.48}$$

where $\mathbf{v}_{rx} = v_{rx}\,\hat{\mathbf{y}}$ and $\hat{\mathbf{k}}_{rx}$ is expressed as

$$\hat{\mathbf{k}}_{rx} = \cos\theta\cos\phi\,\hat{\mathbf{x}} + \cos\theta\sin\phi\,\hat{\mathbf{y}} + \sin\theta\,\hat{\mathbf{z}}, \tag{2.49}$$

where θ and ϕ are the elevation and azimuth angles from the ULA reference channel to a point on $x-y$ plane. Substituting $\mathbf{v}_{rx} = v_{rx}\,\hat{\mathbf{y}}$ and $\hat{\mathbf{k}}_{rx}$ into (2.48) results in

$$f_d = \frac{v_{rx}}{\lambda}\cos\theta\sin\phi. \tag{2.50}$$

Normalizing f_d results in

$$\bar{f}_d = \frac{v_{rx}}{\lambda\, f_r}\cos\theta\sin\phi, \tag{2.51}$$

where f_r is the PRF of the PBR system. Equation (2.51) highlights that $\bar{f}_d$ behaves linearly as function of $\cos\theta \sin\phi$ in the PBR system in contrast to monostatic system where $\bar{f}_d$ is a linear function of $\sin\phi$. In a monostatic system $\cos\theta$ and $\sin\phi$ are decoupled due to circular range bins with constant $\cos\theta$ within the range bin. However, in a PBR system both θ and ϕ vary while traversing the elliptical isorange contour to maintain constant bistatic range [37].

2.7.3 Passive STAP Doppler Response

The total Doppler response, f_{tot}, induced by a moving target in a PBR scenario can be decomposed to two separate Doppler shift components: The target Doppler shift, f_{tgt}, and the receiver Doppler shift, f_{rx}. The target Doppler is defined as

$$\begin{aligned} f_{tgt} &= \frac{\hat{\mathbf{k}}_{tx} \cdot \mathbf{v}_{tgt} + \hat{\mathbf{k}}_{rx} \cdot \mathbf{v}_{tgt}}{\lambda} \\ &= \frac{v_{tgt}}{\lambda}\Big[\hat{\mathbf{k}}_{tx} \cdot \hat{\mathrm{v}}_{tgt} + \hat{\mathbf{k}}_{rx} \cdot \hat{\mathrm{v}}_{tgt}\Big], \end{aligned} \tag{2.52}$$

where $\hat{\mathrm{v}}_{tgt}$ and v_{tgt} are the direction and the magnitude of the target's velocity, $\mathbf{v}_{tgt}$. The unit vectors $\hat{\mathbf{k}}_{tx}$ and $\hat{\mathbf{k}}_{rx}$, and $\hat{\mathrm{v}}_{tgt}$ are defined based on the geometry shown in Figure 2.16 as

$$\hat{\mathbf{k}}_{tx} = \sin\frac{\beta}{2}\,\hat{\mathbf{x}} + \cos\frac{\beta}{2}\,\hat{\mathbf{y}} \tag{2.53a}$$

$$\hat{\mathbf{k}}_{rx} = -\sin\frac{\beta}{2}\,\hat{\mathbf{x}} + \cos\frac{\beta}{2}\,\hat{\mathbf{y}} \tag{2.53b}$$

$$\hat{\mathrm{v}}_{tgt} = \sin\delta\,\hat{\mathbf{x}} + \cos\delta\,\hat{\mathbf{y}}, \tag{2.53c}$$

where β is the bistatic angle, δ is the angle between the bistatic angle bisector and the target velocity vector as shown in Figure 2.16.

Substituting equations (2.53a), (2.53b) and (2.53c) into (2.52) results in

$$\begin{aligned} f_{tgt} &= \frac{v_{tgt}}{\lambda}\left[\sin\frac{\beta}{2}\sin\delta + \cos\frac{\beta}{2}\cos\delta - \sin\frac{\beta}{2}\sin\delta + \cos\frac{\beta}{2}\cos\delta\right] \\ &= \frac{v_{tgt}}{\lambda}\left[\cos\left(\delta - \frac{\beta}{2}\right) + \cos\left(\delta + \frac{\beta}{2}\right)\right] \\ &= \frac{2v_{tgt}}{\lambda}\cos\delta\cos\frac{\beta}{2}. \end{aligned} \tag{2.54}$$

The normalized Doppler induced by both target and receiver platforms are expressed as [37]

$$\bar{f}_{tgt} = \frac{2v_{tgt}}{\lambda f_r}\cos\delta\cos\frac{\beta}{2} \tag{2.55a}$$

$$\begin{aligned} \bar{f}_{rx} &= \frac{\hat{\mathbf{k}}_{rx}\cdot\mathbf{v}_{rx}}{\lambda f_r} \\ &= \frac{v_{rx}}{\lambda f_r}\cos\theta\sin\phi, \end{aligned} \tag{2.55b}$$

where target's position is described by its elevation (θ) and azimuth (ϕ) angles. Combining (2.55a) and (2.55b) yields the following normalized total Doppler response

$$\bar{f}_{tot} = \bar{f}_{tgt} + \bar{f}_{rx} = \frac{2v_{tgt}}{\lambda f_r}\cos\delta\cos\frac{\beta}{2} + \frac{v_{rx}}{\lambda f_r}\cos\theta\sin\phi. \tag{2.56}$$

2.8 Chapter Conclusion

Brief overviews of LTE signal structure and transmission, radar signal processing basics, STAP and RD-STAP were provided in this chapter. The two performance metrics used in analyzing the impacts of varying LTE signal attributes on PBR performance were also introduced. Chapter III will detail the modelling and simulation (M&S) methodology used in this research.

III. Methodology

3.1 Chapter Overview

This chapter outlines the methods employed in the M&S activities of this thesis research. Firstly, it introduces the LTE waveform generation and symbol extraction steps that results in the formation of LTE pulse-train waveforms. Following this, the M&S steps of the core radar signal processing concepts of this research, both FD-STAP and RD-STAP, are documented in detail. This chapter also includes any assumptions adopted to generate the radar and target scene geometry and characteristics.

3.2 LTE Waveform Generation

LTE waveforms can be generated on MATLAB® using either the AFIT LTE or the MATLAB LTE toolboxes. The AFIT LTE toolbox was developed at AFIT by Radar Engineering Faculty and students, which generates an LTE waveform of fixed bandwidth containing 110 RBs per symbol, with 120 symbols per radioframe (extended CP mode). AFIT LTE toolbox provides the flexibility to generate waveforms with or without synchronisation and reference signals and the ability to vary the number of symbols. However, it lacks the ability to easily modify the effective bandwidth and the bit-rate of the signal. Conversely, MATLAB LTE toolbox is more robust in providing greater flexibility in generating waveforms with varying bandwidths, bit-rates, signal duration, and synchronisation and reference signals characteristics. Considering the core aim of this research is to characterize the impacts of varying LTE waveform attributes on PBR performance, MATLAB LTE toolbox was chosen as the preferred LTE waveform modeling tool of this research. A detailed discussion of MATLAB LTE toolbox user interface is provided within [2]. A screen capture of the MATLAB

wireless waveform generator application output of a 20 MHZ LTE FDD DL signal is shown in Figure 3.1 for reference. As highlighted in [2], MATLAB commands were used instead of this user interface to generate multiple realizations of LTE waveforms more robustly and efficiently. A snippet of the code used is provided as Figure 3.2.

3.2.1 Symbol Extraction

As an extension of [2] this research will also extract the fifth symbol to form the individual pulses of the transmit pulse-train waveform in all experiments. This approach removes the control regions and synchronisation signal effects from M&S to focus only on the random user data and CSRE segments of the LTE waveform. The fourth symbol could be used if a waveform with user data without CSRE is desired

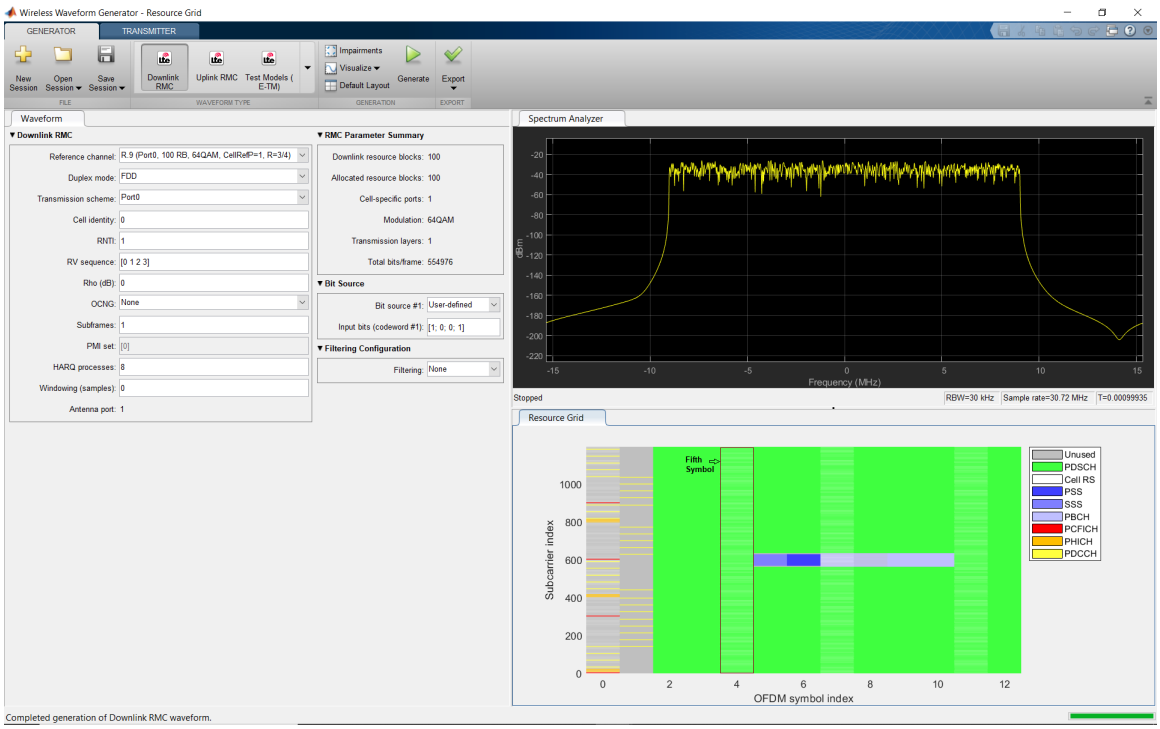

Figure 3.1: Screenshot of MATLAB wireless waveform generator application output showing one realization of 20 MHz 64 QAM LTE FDD DL subframe. The resource grid clearly indicates the symbols containing CSRE, synchronisation, and control signals. The symbol of preference for this research, fifth symbol, can be seen only containing user data samples and CSRE depicted in green and white.

```
rc = 'R.9';
rmc = lteRMCDL(rc);
rmc.DuplexMode = 'FDD';
rmc.TotSubframes = 1;
rmc.PDSCH.Modulation = '64QAM';
[signal, S, sInfo] = lteRMCDLTool(rmc,randi([0 1],1e6,1));
b_eff = 18.015e6;
num_samp = double(sInfo.Nfft);
fsamp_fact = 30.72e6/sInfo.SamplingRate;
CP_samp1 = 160/fsamp_fact;
CP_samp2 = 144/fsamp_fact;
```

Figure 3.2: MATLAB code used to generate one realization of 20 MHz 64 QAM LTE FDD DL subframe, which is a more robust way to generate LTE signals compared to the waveform generator application shown in Figure 3.1. $\text{fsamp}_{\text{fact}}$ (f_s) is the sample scaling factor between the differing bandwidth modes and the highest LTE bandwidth mode of 20 MHz: e.g., sample scaling factor for 10 MHz mode is 2 as the number of useful samples of 10 MHz and 20 MHz are 1024 and 2048 respectively.

(refer to Figure 2.5). The LTE symbol extraction process is dependent on the effective bandwidth of the signal to be generated. Indexing of the samples to be extracted, $Samp_{sym}$, is executed using Equations (3.1a) - (3.1e).

$$T_{start} = \left[N_{cp_1} + \left((n-2)\cdot N_{cp_2}\right) + \left((n-1)\cdot N_u\right)\right]\cdot T_s \tag{3.1a}$$

$$T_{end} = \left[T_{start} + N_{cp_2} + N_u\right]\cdot T_s \tag{3.1b}$$

$$Samp_{start} = T_{start}\times f_s + 1 \tag{3.1c}$$

$$Samp_{end} = T_{end}\times f_s \tag{3.1d}$$

$$Samp_{sym} = Signal\left(Samp_{start} : Samp_{end}\right), \tag{3.1e}$$

where

- n is the symbol to be extracted (fifth symbol in this research),
- T_{start} and T_{end} are the starting and ending time indices of the extracted symbol,

- $Samp_{start}$ and $Samp_{end}$ are the first and the last samples of the extracted symbol,
- N_{cp_1} and N_{cp_2} are the number of samples of the CP corresponding to the first symbol and the remaining six symbols of a normal mode LTE signal,
- T_s and f_s are the sample duration and sampling rate of the LTE signal, and
- *Signal* is the one radioframe of LTE FDD DL generated using MATLAB LTE tool.

3.3 Radar and STAP Model Simulation

This section outlines steps used in modeling both PBR and STAP digital processor. The PBR is assumed to be an airborne side-looking multi-channel ULA radar receiving signals of opportunity from fixed transmitter on ground. This transmitter is defined by position coordinates as discussed in 2.7.1 and shown in Figure 2.17. A flat Earth model is assumed as stated in 1.6, hence the grazing angle can be treated as elevation angle. Finally, given the previously mentioned platform geometry definition, the specific values listed in Table 3.1 were chosen for all experiments of this research.

The x-coordinate of the target location was changed depending on the LTE bandwidth modes. As per detailed in 2.3.4, the bandwidth mode of an LTE signal ranges

Position Coordinate	**Value**
ϕ_T	0°
θ_T	45°
h_T	60 m
h_R	1000 m
$\bar{\mathbf{v}}_{rx}$	$v_{rx}\hat{\mathbf{y}}$
v_{rx}	$\approx$ 112 m/s

Table 3.1: PBR simulation model coordinates

from 1.4 MHz to 20 MHz, which impacts the range resolution of the LTE waveform. Therefore, selection of a target's x-coordinate position is critical in ensuring that sufficient matched filter responses can be simulated. This approach is required to model the clutter-Doppler spreading due to decorrelation of range sidelobes resulting from LTE pulse diverse waveform [37]. The six available LTE bandwidth modes were grouped into three separate bandwidth pairs: High-band (20 and 15 MHz); Mid-band (10 and 5 Mhz); and Low-band (3 and 1.4 MHz). Subsequently, the target's x-coordinate was changed for each of these bands, in order to model the clutter-Doppler spread using CMT (refer to 2.5.3).

3.3.1 Element-space Post-Doppler Simulation

This section outlines the M&S steps used to model the element-space post-Doppler STAP technique of EFA: one of the two RD-STAP algorithms analyzed in this project. Detailed description of EFA can be found in [29] and in Section 2.6.3 of this thesis report.

1. Assign radar waveform attributes for the simulation experiment as per listed below:
   (a) Set the number of pulses, M, to 16.
   (b) Set the number of channels, N, to 8.
   (c) Set the preferred RCS model for the clutter. All experiments used the IPOP clutter RCS model described in 2.5.3, unless otherwise specifically stated.
   (d) Set the PRF to 7500 Hz.
   (e) Set the PBR geometry coordinates values as per listed in Table 3.1.
2. Set the following LTE waveform attributes for each simulation experiment

(a) Specify the LTE bandwidth mode through changing the port value ('R.4' (1.4 MHz) through to 'R.9' (20 MHz)), refer to Figure 3.2.

(b) Choose one of the following LTE subcarrier modulation scheme: QPSK, 16 QAM or 64 QAM.

(c) Specify the effective bandwidth associated with the LTE bandwidth mode chosen for the experiment, where $\mathrm{B}_e = (N_u + 1) \cdot 15 \times 10^3$.

3. Generate a pulse-train waveform containing diverse LTE symbol in each pulse as per detailed below.

   (a) For each pulse generate 1 subframe of the LTE waveform defined at step 2. Refer Figure 3.2 for the MATLAB code used to generate this subframe.

   (b) Use sub-equations of (3.1) to extract the fifth symbol of the LTE subframe generated. Tag and store the extracted symbol as the signal corresponding to the respective pulse.

   (c) Repeat steps 3a and 3b for each of the M pulses.

   (d) Combine the individual pulses to form a pulse-train waveform, which will be used as the received radar signal in this simulation.

4. Set the preferred matched filter length by specifying the corresponding maximum range, where $\mathrm{R}_{max} = c \cdot \tau_{mf}$, τ_{mf} is the preferred matched filter duration and c is the speed of light in vacuum. For experiments using *Short* MF, let $\tau_{mf} = 5.4\mu s$. Similarly, for experiments using *Full* MF, let $\tau_{mf} = T_{sym} = 66.67\mu s$.

5. Use the R_{max} to perform match filtering of the received radar signal (LTE pulse-train) across fast-time using MATLAB *xcorr* function. Normalize this match filter response and store results.

6. Calculate clutter space-time snapshot, $\boldsymbol{\chi}_c$, and clutter covariance matrix, $\mathbf{R}_c$ through completing the below steps:

   (a) Calculate the temporal steering vector for all clutter patches, $\mathbf{b}(\bar{\omega})$. For experiments with ICM, add the chosen method's taper to the temporal steering vector. Design these ICM tapers for Method 1 and Method 2 using Equations (2.22) and (2.28).

   (b) Calculate the spatial steering vector for all clutter patches, $\mathbf{a}(\vartheta)$.

   (c) Calculate the space-time steering vector for all clutter patches, $\mathbf{v}(\vartheta, \bar{\omega})$ using Equation (2.11).

   (d) Calculate the RCS for each clutter patch based on the IPOP RCS model chosen. Refer to Subsection 2.5.3 for further details regarding RCS calculation.

   (e) Calculate CNR for each clutter patch using Equation (2.16).

   (f) For experiments without ICM

      i. Calculate $\boldsymbol{\chi}_c$ using Equation (2.14).

      ii. Calculate $\mathbf{R}_c$ using Equation (2.18).

   (g) For experiments with ICM

      i. Calculate $\boldsymbol{\chi}_c$ using Equations (2.21) and (2.22).

      ii. Calculate $\mathbf{R}_c$ using Equations (2.23) and (2.24).

   (h) Apply CMT to $\mathbf{R}_c$ using Equation (2.20).

7. Calculate noise space-time snapshot, $\boldsymbol{\chi}_n$, and noise covariance matrix, $\mathbf{R}_n$ by executing the following steps:

   (a) Calculate $\boldsymbol{\chi}_n$, such that $\boldsymbol{\chi}_n = \sigma^2 \alpha_n$, where α_n is a vector of length $MN \times 1$

containing complex noise amplitudes corresponding to each pulse-channel pair.

(b) Calculate $\mathbf{R}_n$ using Equation (2.32).

8. Calculate interference-plus-noise space-time snapshot, $\boldsymbol{\chi}_u$, where $\boldsymbol{\chi}_u = \boldsymbol{\chi}_c + \boldsymbol{\chi}_n$

9. Calculate the clairvoyant interference-plus-noise covariance matrix $\mathbf{R}_u = \mathbf{R}_c + \mathbf{R}_n$.

10. Estimate the space-time covariance matrix, $\hat{\mathbf{R}}$, by employing the SMI technique described in 2.5.6, in particular using Equation (2.37).

11. Calculate both optimum and practical FD-STAP filters, $\mathbf{w}_{\mathrm{o}}$ and $\mathbf{w}$, using Equations (2.35) and (2.38).

12. Calculate $\mathrm{SINR}_{\mathrm{L,o}}$ and $\mathrm{SINR}_{\mathrm{L}}$ for the FD-STAP using Equations (2.42) and (2.43).

13. Gather $\boldsymbol{\chi}_u$ of all rangebins and form a 3D datacube of dimension $M \times N \times L$.

14. Calculate target space-time snapshot for a target with position coordinate specified within Table 3.1, and place it at the appropriate rangebin of the datacube.

15. Assign the preferred EFA number, e.g., EFA number is 3 for Order 1 and 5 for Order 2 EFA.

16. Perform Doppler filtering of the space-time data by applying one-dimensional FFT across the slow-time components of both datacube and space-time steering vector.

17. Estimate the space-Doppler covariance matrix, $\hat{\tilde{\mathbf{R}}}$, for the chosen EFA case using SMI technique described in 2.5.6, in particular using Equation (2.37). Note, the

number of training data range bins would have reduced to $2 \times M_d \times N$, where M_d is the number of Doppler bins selected to perform adaptive filtering at each Doppler bin as per shown in Figure 2.13. Basically, M_d must equal the EFA number chosen at step 15.

18. Perform adaptive filtering at each Doppler bin with Doppler bin width restricted to the EFA number to calculate both optimum and practical RD-STAP weight vectors for all Doppler bins, $\tilde{\mathbf{w}}_{\mathrm{o}}$ and $\tilde{\mathbf{w}}$, using Equations (2.46a) and (2.46b).

19. Calculate $\mathrm{SINR}_{\mathrm{L,o}}$ and $\mathrm{SINR}_{\mathrm{L}}$ at each Doppler bin as a result of implementing this RD-STAP (EFA) technique using Equations (2.42) and (2.43). Store the $\mathrm{SINR}_{\mathrm{L,o}}$ and $\mathrm{SINR}_{\mathrm{L}}$ results of each realization separately.

20. Repeat steps 3 - 19 for the preferred number of realizations, which for this research was fixed at 200: Adopted same number of realizations as [2] to maintain consistency when comparing results.

21. Calculate the mean $\mathrm{SINR}_{\mathrm{L,o}}$ and $\mathrm{SINR}_{\mathrm{L}}$ curves for 200 realizations and store the results.

22. Repeat steps 1 - 21 for each bandwidth and subcarrier modulation scheme combination.

3.3.2 Beamspace Post-Doppler simulation

M&S steps required to implement JDL, which is the beamspace post-Doppler STAP technique chosen for analysis in this research, are outlined below. Most of the steps between the element and beamspace post-Doppler techniques are identical, particularly generation of the space-time datacube. Hence, these steps were kept common between these two techniques. Steps that are distinctly different between EFA and JDL are listed as follows.

1. Execute steps 1 to 15 listed in Subsection 3.3.1.

2. Perform Doppler processing and beamforming of the space-time data through applying 2D FFT to the space-time datacube and the space-time steering vector.

3. Assign preferred number of angular beam bins, N_b, and Doppler bins M_d, to form each LPR.

4. Extract angle-Doppler data corresponding to the specified number of beam bins centred at the look angle of $\theta = 0^\circ$ as per detailed in Subsection 2.6.4. This will result in a transformed datacube of size $M \times N_b \times L$.

5. Estimate the angle-Doppler covariance matrix, $\hat{\tilde{\mathbf{R}}}$, for the chosen Doppler-angle bin number combination using SMI technique described in 2.5.6, in particular using Equation (2.37). Note, the number of training data range bins would have reduced to $2 \times M_d \times N_b$.

6. Perform adaptive filtering and calculate $\text{SINR}_{\text{L,o}}$ and SINR_{L} due to implementing JDL algorithm at each Doppler bins be adopting steps 18-19 listed in Subsection 3.3.1.

7. Repeat these steps for 200 realizations.

8. Calculate the mean $\text{SINR}_{\text{L,o}}$ and SINR_{L} curves for the 200 realizations and store the results.

9. Repeat steps 1 - 8 for each bandwidth and subcarrier modulation scheme combination.

IV. Results and Analysis

4.1 Overview

This chapter documents the results of the M&S activities, conducted in accordance with the methodology described in chapter III. The two RD-STAP algorithms were compared through analyzing the impact on optimum SINR Loss ($SINR_{L,o}$) and estimated SINR Loss ($SINR_L$) curves due to varying LTE signal's bandwidth mode, and the bit-rate. Furthermore, as a control measure, the FD-STAP M&S results were compared with the results presented in [2]. This comparison confirmed the FD-STAP $SINR_{L,o}$ curves followed the same trend as [2], which ensured the M&S methodology adopted is sound and similar to the previously endorsed research that acted as the stepping-stone for this research. $SINR_{L,o}$ curves are referenced using 'OPT' subscript in the legend of the results provided throughout this chapter. Similarly, the absence of subscript in the legend indicates that the associated SINR curve relates to $SINR_L$.

4.2 Bandwidth mode effects on SINR Loss

As established in [2], $SINR_{L,o}$ of FD-STAP worsened with decrease in LTE bandwidth modes, with 20 MHz LTE signal producing the best $SINR_{L,o}$ compared to the remaining LTE bandwidth modes. The same trend was also observed with the RD-STAP algorithms as per highlighted in Figures 4.1 - 4.15. Similarly, the increase in the RD-STAP complexity was also seen to degrade the SINR loss performance, with EFA offering better performance compared to JDL at each bandwidth mode. As per detailed within 2.6.2, JDL is classified to be the most complex RD-STAP algorithm between EFA and JDL. Furthermore, within each RD-STAP algorithm, $SINR_{L,o}$ was better than $SINR_L$ as expected due to space-time covariance matrix estimation errors and subsequent inefficiencies introduced in generating $SINR_L$. Finally, an $SINR_{L,o}$ or

$SINR_L$ curve with smaller negative dB values demonstrates better target detection performance than a curve with larger negative dB values. In other words, an increasing trend in negative dB values is indicative of SINR loss performance degradation, while a decreasing trend indicates performance improvement.

4.2.1 High band - 20 and 15 MHz

As per detailed in Section 3.3, the selection of the target's x-coordinate position was dependent on the LTE bandwidth mode. Thus, for the High-band, the x-coordinate position was chosen to be 3100 m, same as Taylor's research model [2] for ease of comparison. However, the same target position could not be used for lower bandwidth modes due to poor range resolution, requiring target to be placed further out to sufficiently capture the matched filter response's sidelobes. Subsections 4.2.2 and 4.2.3 discusses the lower bandwidth modes in detail.

Figures 4.1, 4.2 and 4.3 corroborates Taylor's findings in [2] that $SINR_{L,o}$ improves with increase in LTE signal's bandwidth for FD-STAP. These results further establish that both RD-STAP algorithms follow the same trend as well. In particular within each RD-STAP algorithm, $SINR_{L,o}$ outperformed $SINR_L$ as expected due to space-time clutter covariance matrix estimation errors as stated in Section 4.2. Furthermore, the $SINR_L$ performance of EFA in the heavy-clutter region (low normalized Doppler region) was observed to perform slightly better compared to $SINR_{L,o}$ curves of JDL within the same region. Thus, this indicates that $SINR_L$ of EFA algorithm outperforms $SINR_{L,o}$ of JDL algorithm in heavy-clutter scenarios. From a more practical sense, EFA is the best performing of the two RD-STAP algorithms by a margin of approximately 3 dB in the clutter-heavy regions (low-Doppler values) and by a margin of 1 dB in the noise-heavy regions (higher-Doppler values).

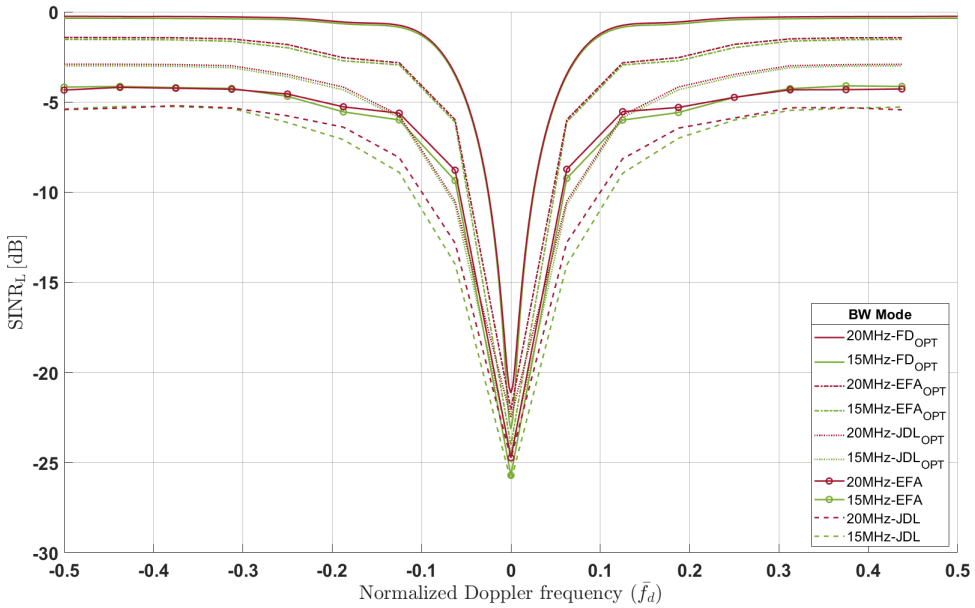

Figure 4.1: Mean $\text{SINR}_{\text{L,o}}$ and SINR_{L} curves comparing the effects of High-band bandwidth modes for QPSK LTE modulation scheme.

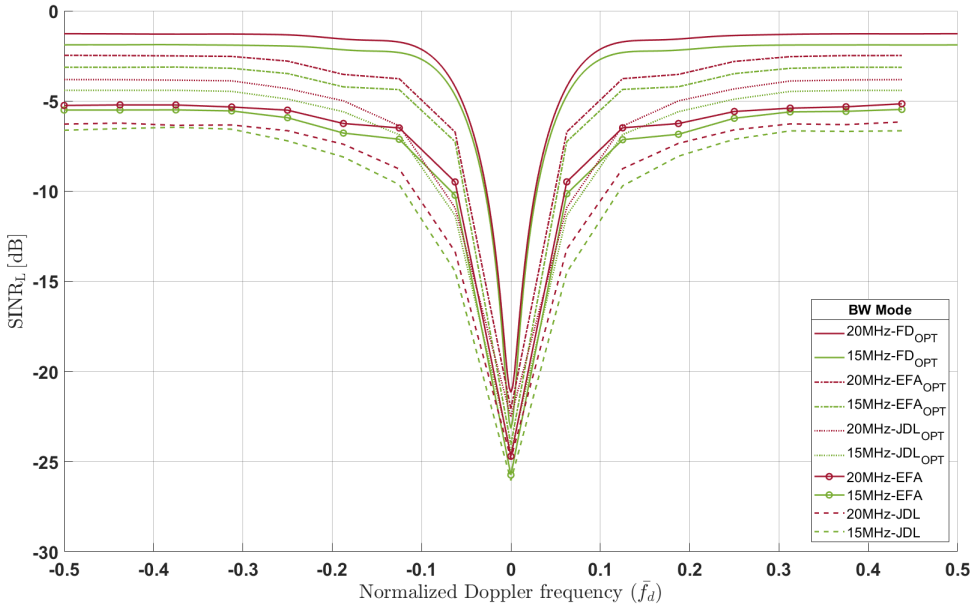

Figure 4.2: Mean $\text{SINR}_{\text{L,o}}$ and SINR_{L} curves comparing the effects of High-band bandwidth modes for 16 QAM LTE modulation scheme.

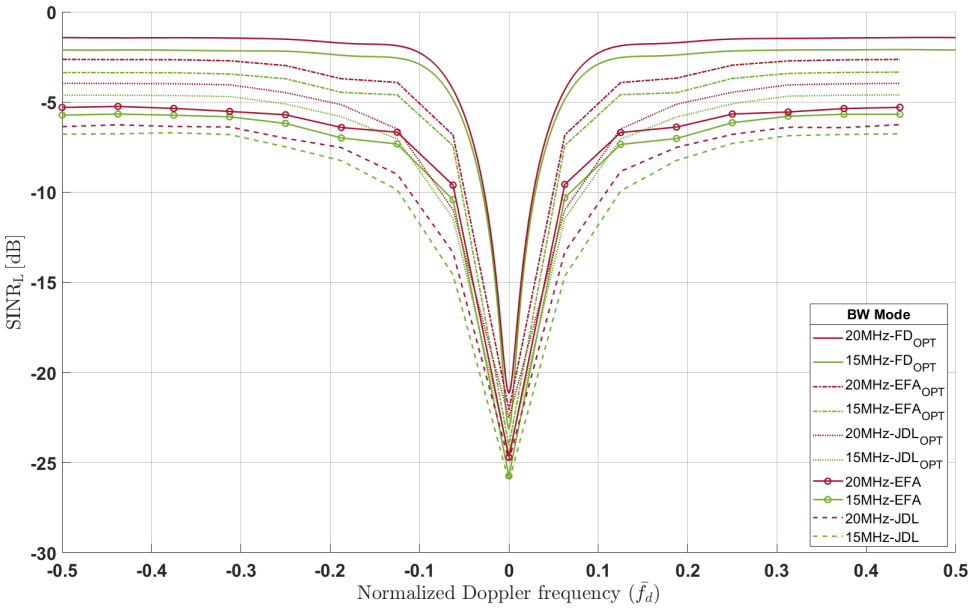

Figure 4.3: Mean $\text{SINR}_{\text{L,o}}$ and SINR_{L} curves comparing the effects of High-band bandwidth modes for 64 QAM LTE modulation scheme.

SINR loss values at $\bar{f}_d = -0.5$ were extracted for each bandwidth mode - bit-rate - STAP technique combination and plotted together as 3D bar graphs in Figures 4.4 and 4.5. Results were grouped and plotted in Figure 4.4 in such a way that it compares the bandwidth mode variation across various STAP techniques. These results confirm the previously established conclusion that SINR_{L} and $\text{SINR}_{\text{L,o}}$ degrades with decrease in LTE signal bandwidth mode. Similarly, Figure 4.5 highlights the previously observed trend that SINR loss performance improves with decrease in RD-STAP complexity. Additionally, Figure 4.5 also confirmed that $\text{SINR}_{\text{L,o}}$ outperformed SINR_{L} in both RD-STAP techniques. Figures 4.4 and 4.5 are presented to provide an alternative perspective for the reader to compare the SINR loss performance impacts. Finally, these figures provide a snapshot at a specific normalized Doppler frequency with taller bars indicative of better SINR performance (lower SINR loss) and shorter bars corresponds to poor performance (higher SINR loss).

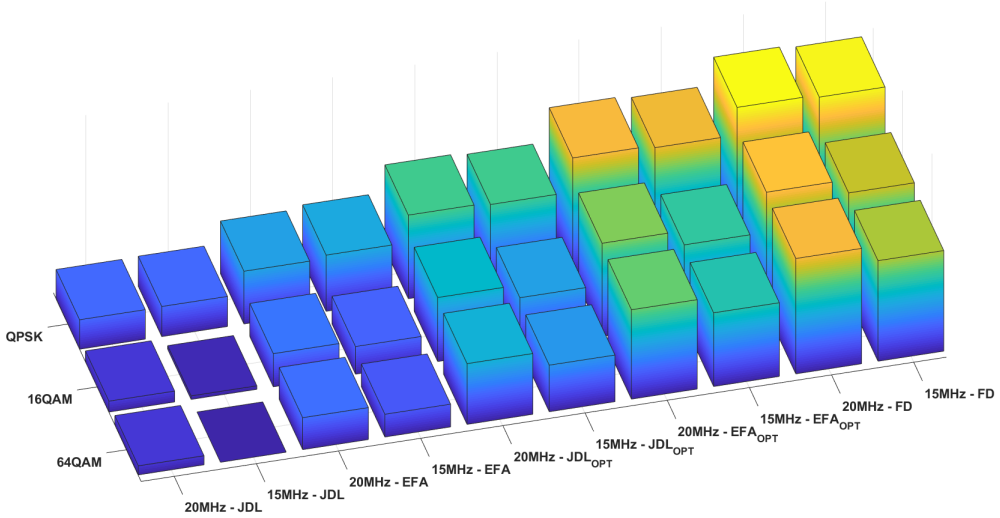

Figure 4.4: High-Band bandwidth modes comparison across STAP techniques at $\bar{f}_d = -0.5$. The height of the bar graphs is inversely related to the SINR loss. Tall bars represent better SINR loss performance (lower SINR loss) while shorter bars correspond to poor performance (higher SINR loss).

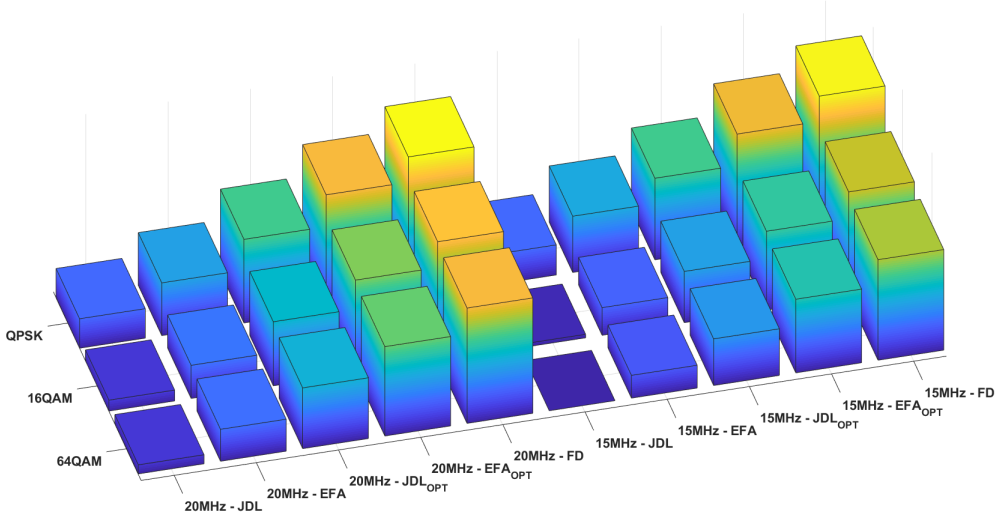

Figure 4.5: High-Band STAP techniques comparison across bandwidth modes at $\bar{f}_d = -0.5$. Tall bars represent better SINR loss performance while shorter bars correspond to poor performance.

4.2.2 Mid-band - 10 and 5 MHz

Due to the physical limitations imposed by the lower bandwidth modes, the target position had to be changed for different bandwidth modes. High-band simulations adopted the same target position as [2] (see Section 4.2.1), which is not valid for the lower bandwidth modes due to an increase in ΔR. Hence, target x-coordinate position of 6500 m was chosen for the Mid-band bandwidth modes. Simulation results provided as Figures 4.6, 4.7 and 4.8 indicate both $\text{SINR}_{\text{L,o}}$ and SINR_{L} degraded with decrease in bandwidth mode for both FD-STAP and RD-STAP algorithms. These results were consistent with Section 4.2.1 results. Additionally, the complexity of the RD-STAP algorithm had also influenced SINR loss with increase in complexity worsening both $\text{SINR}_{\text{L,o}}$ and SINR_{L}. Same trend was also observed with both High-band and Low-band bandwidth modes. Reduction in both DoF and the available training data have contributed to this observation. Finally, the SINR_{L} of EFA was observed to be slightly better than $\text{SINR}_{\text{L,o}}$ of JDL near the clutter notch. This supports a conclusion that EFA performs better than JDL when in close proximity to the clutter notch (ridge). More specifically, adopting JDL in the clutter-heavy regions worsened SINR_{L} by approximately 4 dB in comparison with EFA. Similarly, employing EFA in the noise-heavy regions improved SINR_{L} by approximately 2.5 dB compared to JDL.

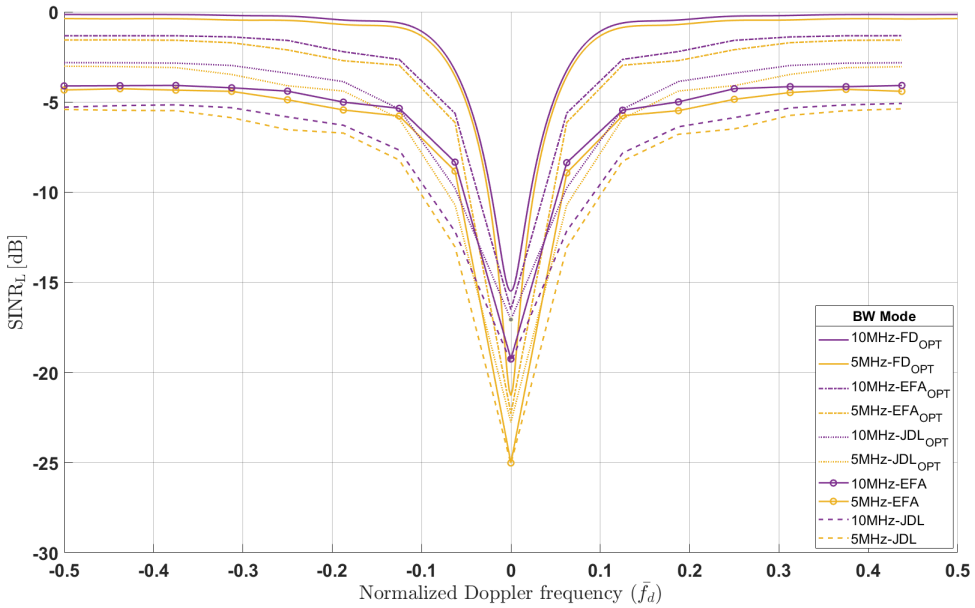

Figure 4.6: Mean $\text{SINR}_{\text{L,o}}$ and SINR_{L} curves comparing the effects of Mid-band bandwidth modes for QPSK LTE modulation scheme.

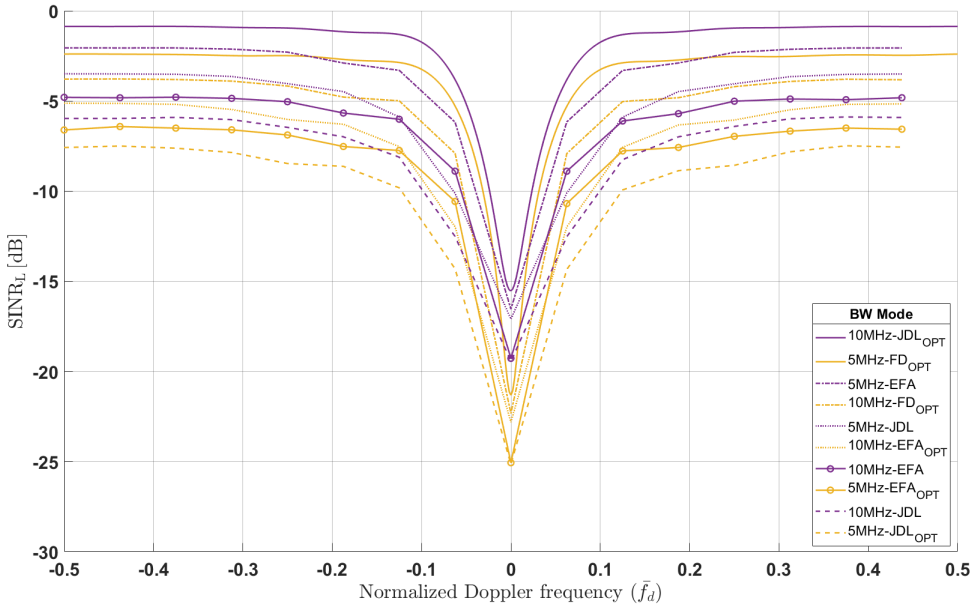

Figure 4.7: Mean $\text{SINR}_{\text{L,o}}$ and SINR_{L} curves comparing the effects of Mid-band bandwidth modes for 16 QAM LTE modulation scheme.

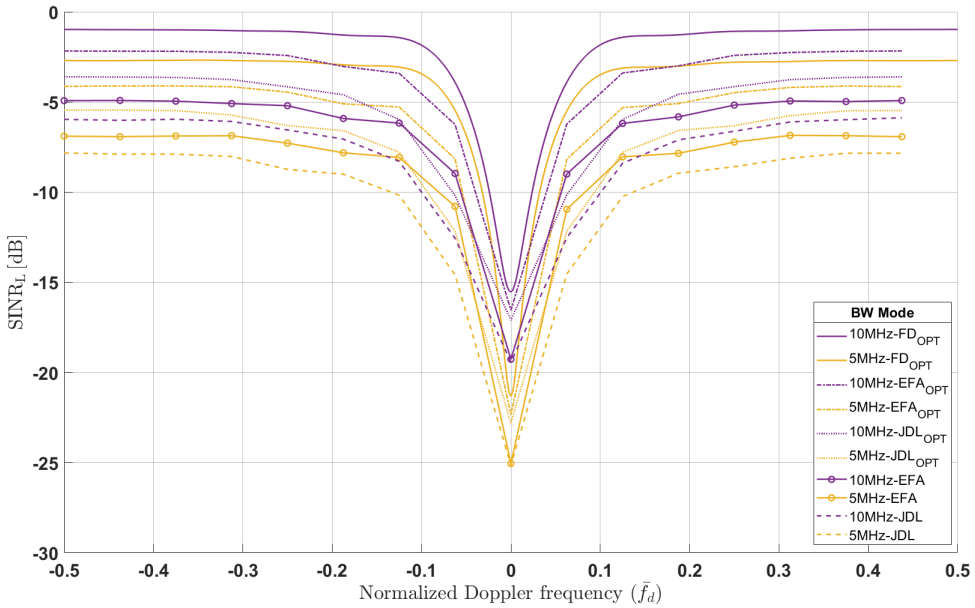

Figure 4.8: Mean $\text{SINR}_{\text{L,o}}$ and SINR_{L} curves comparing the effects of Mid-band bandwidth modes for 64 QAM LTE modulation scheme.

SINR loss values at $\bar{f}_d = -0.5$ were extracted for each of the Mid-band bandwidth modes and plotted together as 3D bar graphs in Figures 4.9 and 4.10. Figure 4.9 plotted compares the bandwidth mode variation across FD-STAP and RD-STAP techniques. The results corroborate the earlier conclusion that SINR_{L} and $\text{SINR}_{\text{L,o}}$ degrades with decrease in LTE signal bandwidth mode. Similarly, Figure 4.10 highlights the previously observed trend that SINR loss performance improves with decrease in RD-STAP complexity. Finally, Figure 4.10 also confirmed that $\text{SINR}_{\text{L,o}}$ outperformed SINR_{L} in both RD-STAP techniques.

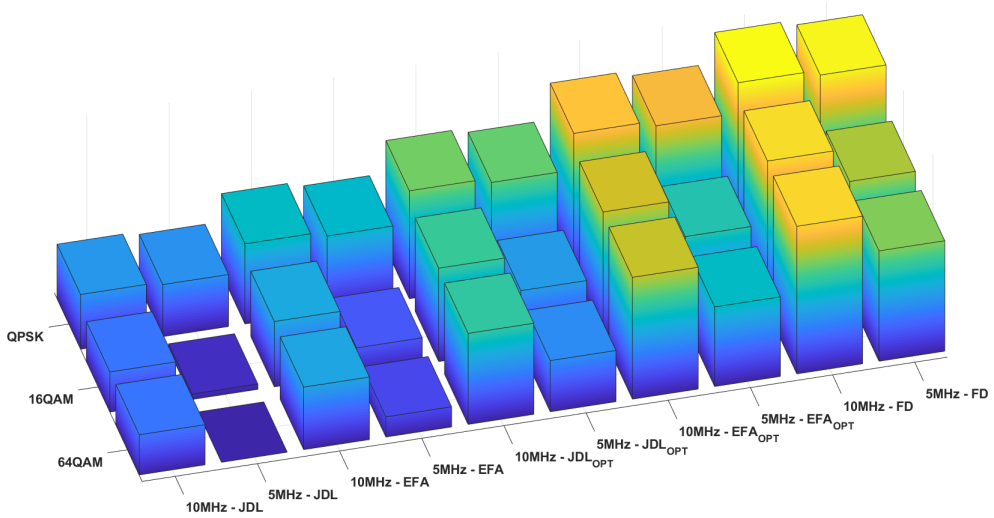

Figure 4.9: Mid-Band bandwidth modes comparison across STAP techniques at $\bar{f}_d = -0.5$. Tall bars represent better SINR loss performance while shorter bars correspond to poor performance.

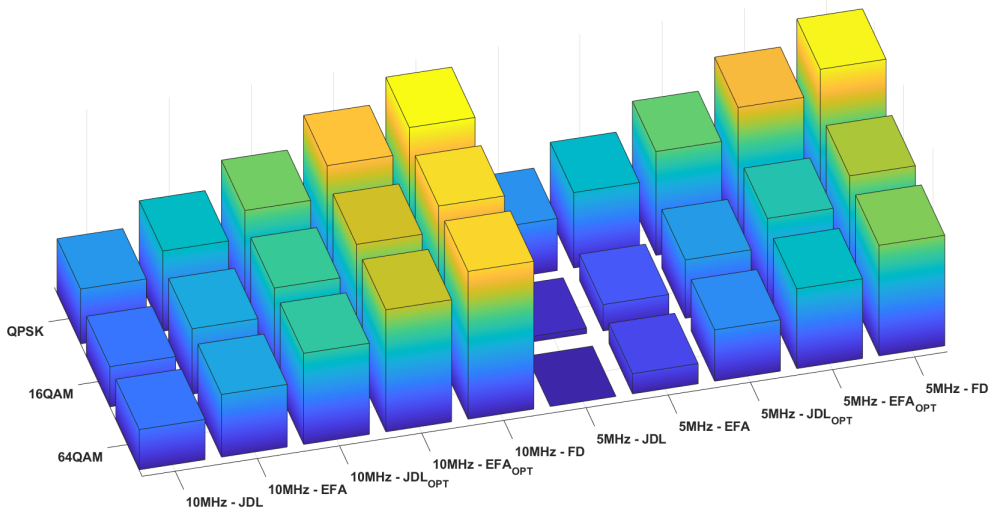

Figure 4.10: Mid-Band STAP techniques comparison across bandwidth modes at $\bar{f}_d = -0.5$. Tall bars represent better SINR loss performance while shorter bars correspond to poor performance.

4.2.3 Low-band - 3 and 1.4 MHz

The target position for the Low-band simulations was extended to 20500 m. $\mathrm{SINR_{L,o}}$ and $\mathrm{SINR_L}$ comparison is plotted for each modulation scheme in Figures 4.11, 4.12 and 4.13. Additionally, SINR loss values at $\bar{f}_d = -0.5$ for each of the Low-band bandwidth modes were plotted as 3D bar graphs in Figures 4.14 and 4.15. Analysis of these results indicate the trends observed with higher bandwidth modes were applicable to Low-band as well. Hence, further details are not provided in the interest of avoiding repeated analysis.

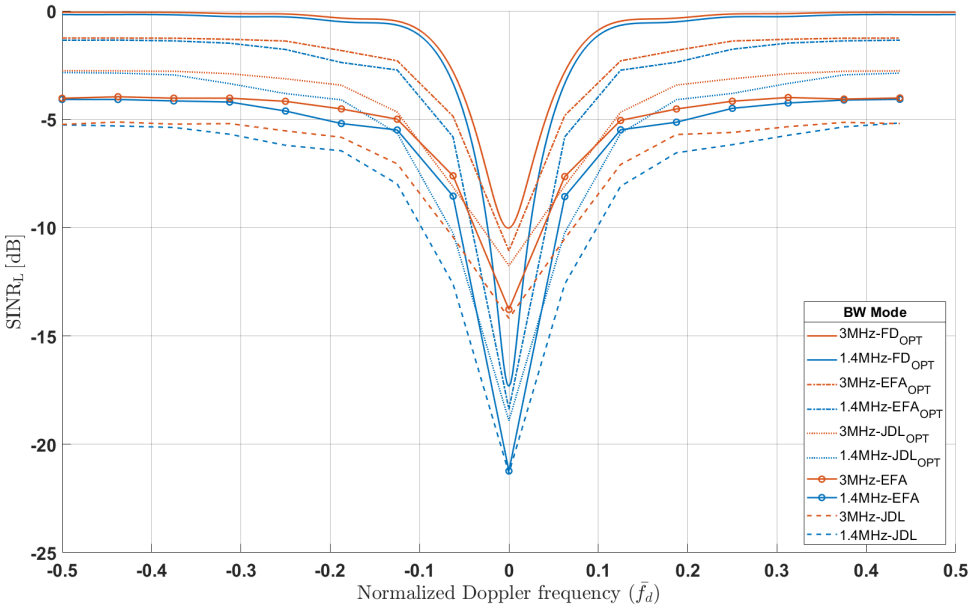

Figure 4.11: Mean $\mathrm{SINR_{L,o}}$ and $\mathrm{SINR_L}$ curves comparing the effects of Low-band bandwidth modes for QPSK LTE modulation scheme.

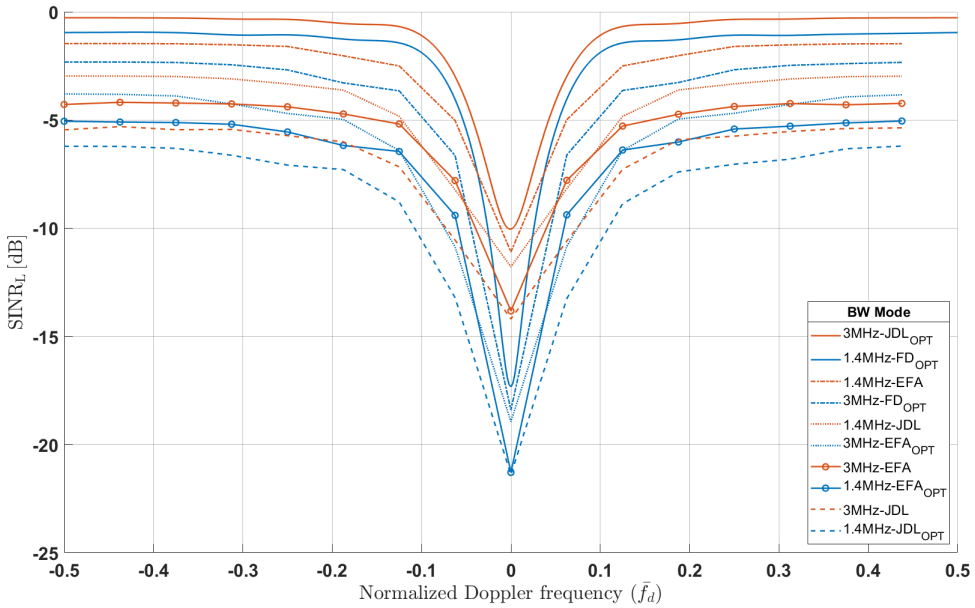

Figure 4.12: Mean $\text{SINR}_{\text{L,o}}$ and SINR_{L} curves comparing the effects of Low-band bandwidth modes for 16 QAM LTE modulation scheme.

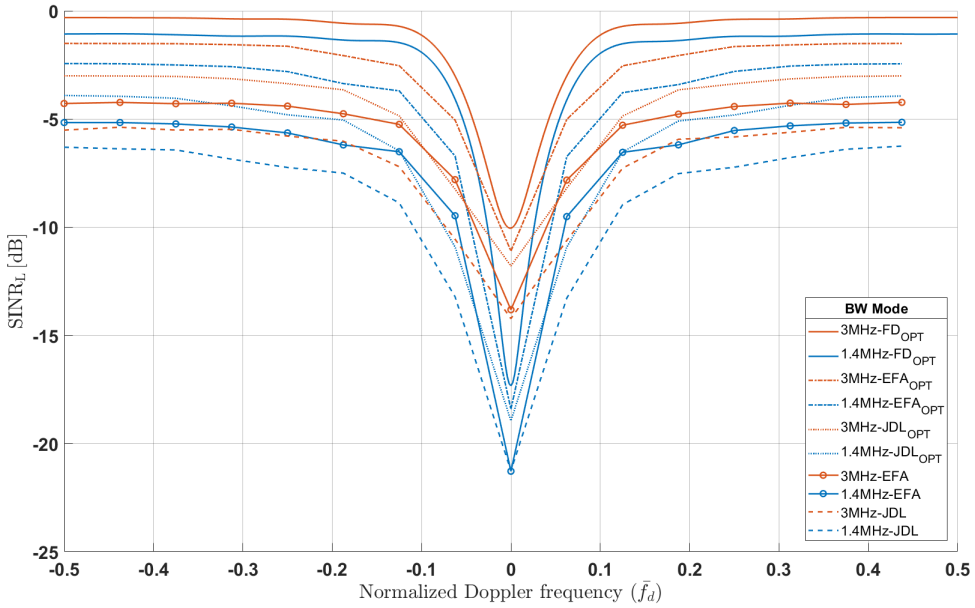

Figure 4.13: Mean $\text{SINR}_{\text{L,o}}$ and SINR_{L} curves comparing the effects of Low-band bandwidth modes for 64 QAM LTE modulation scheme.

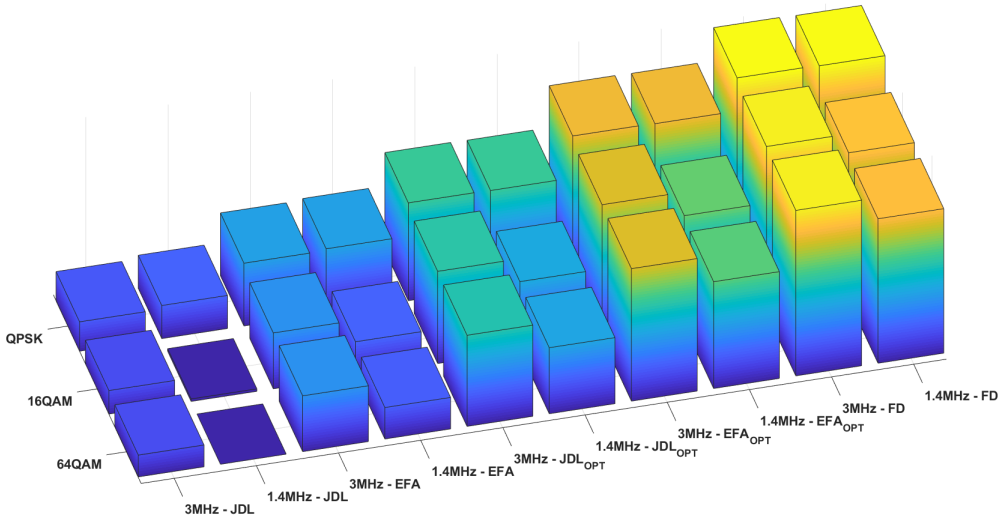

Figure 4.14: Low-Band bandwidth modes comparison across STAP techniques at $\bar{f}_d = -0.5$.

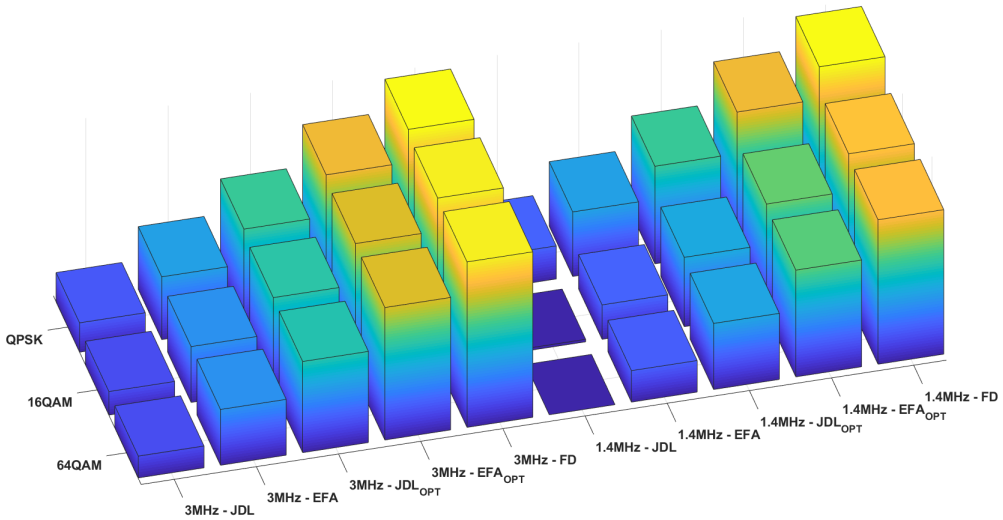

Figure 4.15: Low-Band STAP techniques comparison across bandwidth modes at $\bar{f}_d = -0.5$.

4.3 Subcarrier Modulation scheme (LTE bit-rate) effects on SINR Loss

As per established in [2], $\text{SINR}_{\text{L,o}}$ of FD-STAP worsened with increase in LTE bit-rate, with 64 QAM signal producing the worst SINR loss compared to 16 QAM and QPSK signals. QPSK produced the best $\text{SINR}_{\text{L,o}}$ and SINR_{L} of the three LTE bit-rates. This trend was also observed with the RD-STAP algorithms in Figures 4.16, 4.17 and 4.18. Increase in the RD-STAP complexity has degraded the SINR loss performance, with EFA offering better performance compared to JDL for each LTE bit-rate. Furthermore, within each RD-STAP algorithm, $\text{SINR}_{\text{L,o}}$ outperformed SINR_{L} as expected and as previously observed with bandwidth comparison results in Section 4.2. Finally, Figure 4.19 compare the effects of varying signal bit-rates across various STAP techniques using 3D bar graphs plotted using SINR values at $\bar{f}_d = -0.5$. These graphs confirmed the trends outlined above while providing an alternate perspective for the reader to visualize these trends.

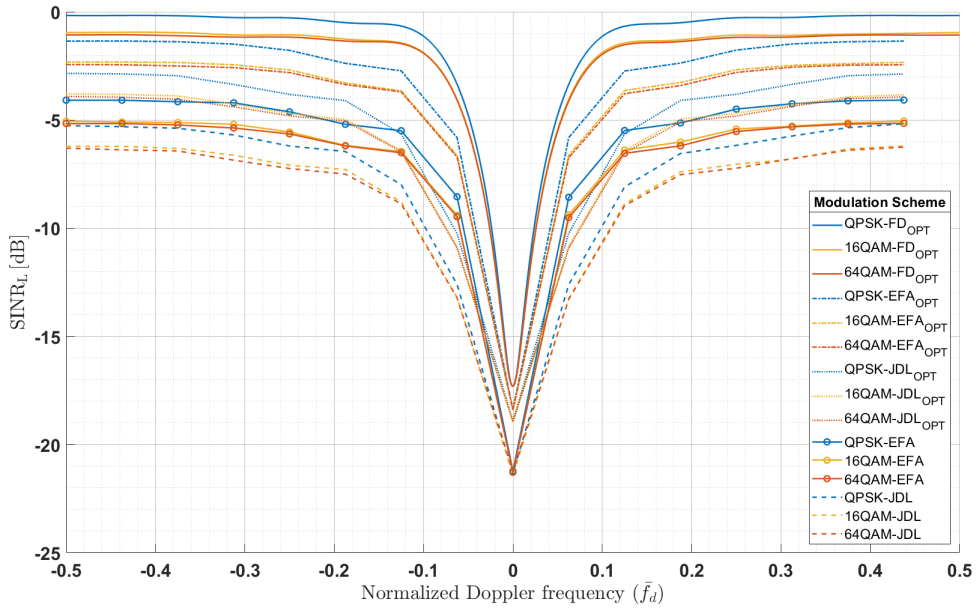

(a) 1.4 MHz

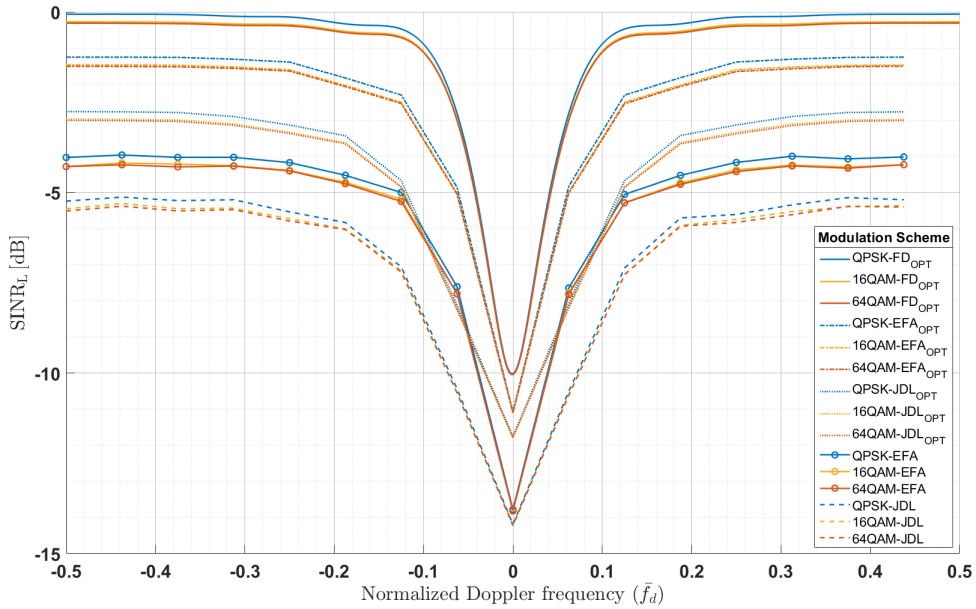

(b) 3 MHz

Figure 4.16: Mean $\text{SINR}_{\text{L,o}}$ and SINR_{L} curves comparing the effects of subcarrier modulation schemes for the Low-band LTE bandwidth modes. Figures 4.17 and 4.18 compares the remaining bandwidths.

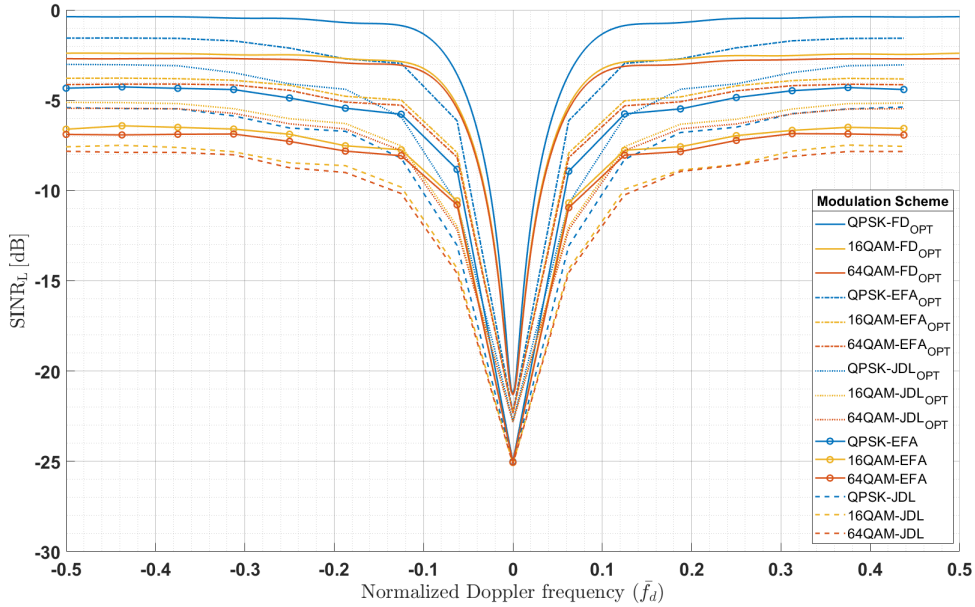

(a) 5 MHz

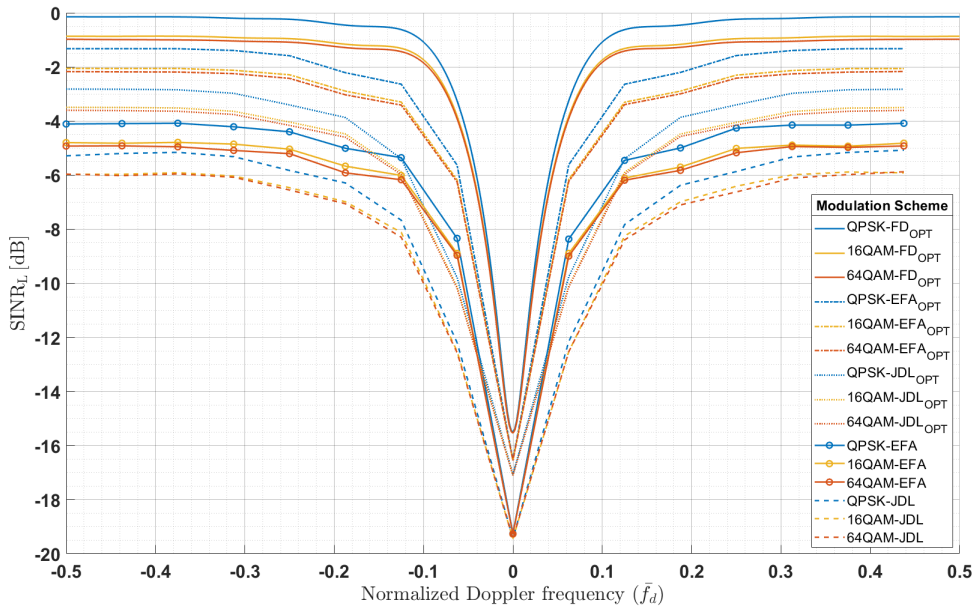

(b) 10 MHz

Figure 4.17: Mean SINR$_{L,o}$ and SINR$_L$ curves comparing the effects of subcarrier modulation schemes for the Mid-band LTE bandwidth modes.

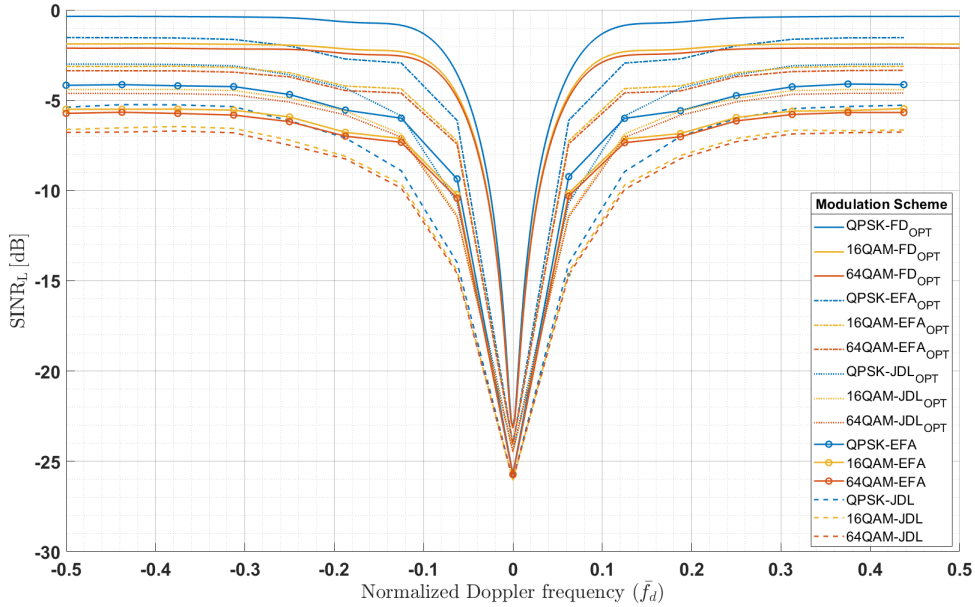

(a) 15 MHz

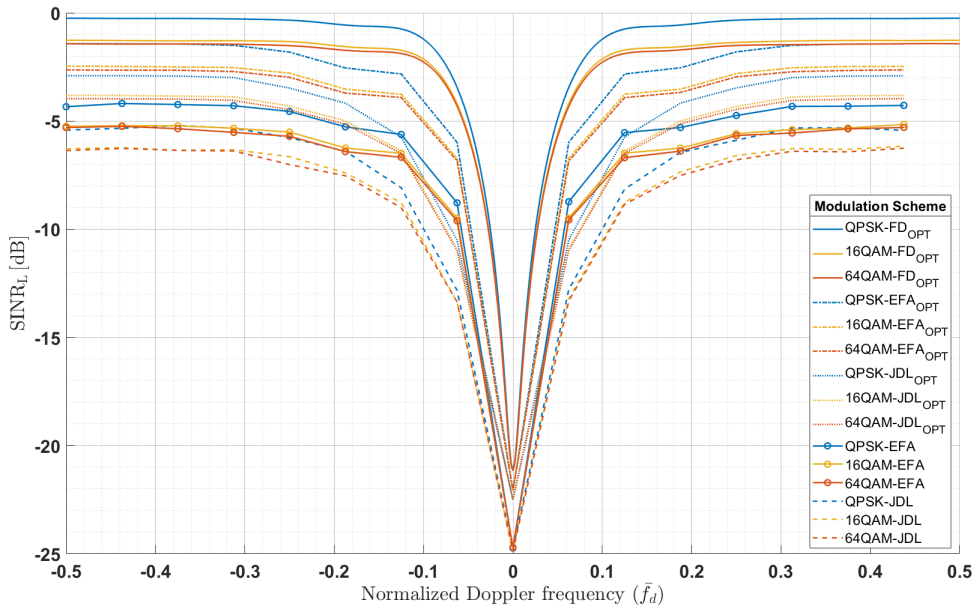

(b) 20 MHz

Figure 4.18: Mean SINR$_{L,o}$ and SINR$_L$ curves comparing the effects of subcarrier modulation schemes for the High-band LTE bandwidth modes.

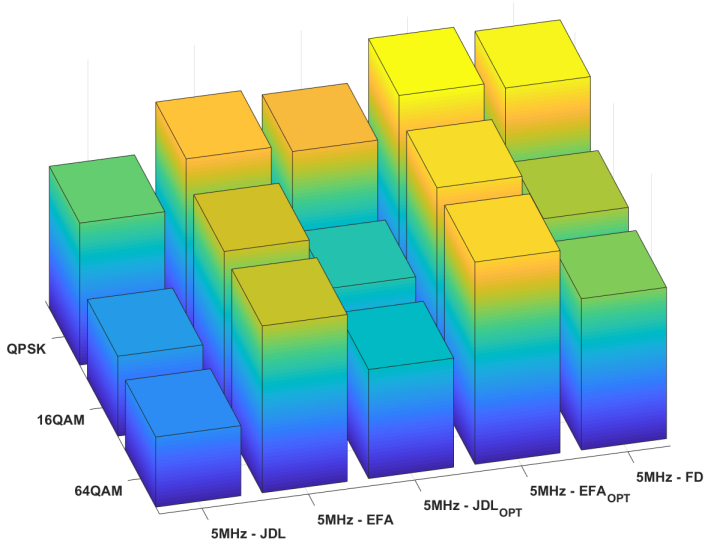

(a) 5 MHz

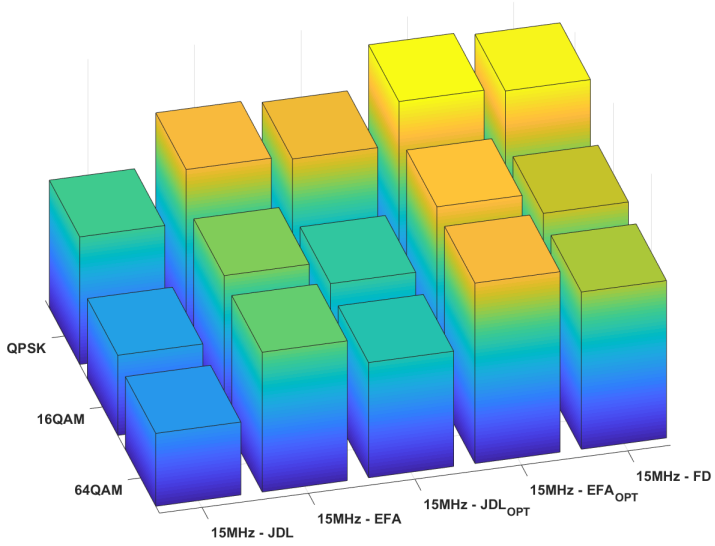

(b) 15 MHz

Figure 4.19: Comparison of subcarrier modulation scheme effects across STAP techniques of 5 MHz LTE signal at $\bar{f}_d = -0.5$. The height of the bar graphs is inversely related to the SINR loss. Tall bars represent better SINR loss performance (lower SINR loss) while shorter bars correspond to poor performance (higher SINR loss). Increase in signal bit-rates degraded the SINR performance. Increase in RD-STAP complexity within a bandwidth mode had also degraded the SINR performance.

4.4 LTE Transmission Mode Performance Trade-off

The analysis of the results presented within sections 4.2 and 4.3 concludes that both increasing the signal bandwidth and decreasing its bit-rate will degrade $\text{SINR}_{\text{L,o}}$ and SINR_{L} of both FD-STAP and RD-STAP. Thus, this provides an initial template to choose the best available LTE signal to meet the mission requirements. However, choosing a signal with the highest bandwidth or lowest bit-rate may not be the best approach. The results indicate that the bandwidth mode and bit-rate must be considered in tandem to obtain the best performance. Transmission signal choice made solely based on just one of these criteria will introduce SINR loss performance trade-off due to inadvertently choosing the low performing option for the remaining criterion. Figure 4.20 corroborates this finding through demonstrating that the SINR loss performance of a lower bandwidth - lower bit-rate LTE signal is superior to a higher bandwidth - higher bit-rate LTE signal.

This finding is further restricted through constraining the presence of performance trade-off to the LTE signals with closer bandwidth mode separation. Increasing the separation between LTE bandwidth modes significantly reduces the impact of bit-rate on SINR loss performance trade-off. This adjustment to SINR loss performance is established through comparing LTE signals with larger bandwidth mode separation in Figure 4.21. Target's x-coordinate position for the Mid-band bandwidth modes was changed to match Low-band (20500 m) to enable accurate comparison of simulation results in this section.

Furthermore, The choice of bandwidth mode directly impacts the range resolution performance of the waveform. Table 4.1 lists the range resolution metrics (ΔR) for each of the LTE bandwidth modes. Hence, choosing a low bandwidth low bit-rate signal, while improving the SINR loss performance metric, degrades the range resolution offered. Therefore, careful consideration of the performance trade-off between

SINR loss and ΔR metrics must be exercised in choosing the best LTE signal of opportunity that meets the needs of the mission.

B **[MHz]**	B_e **[MHz]**	ΔR **[m]**
1.4	1.095	107.07
3	2.715	49.97
5	4.515	29.98
10	9.015	14.99
15	13.515	9.99
20	18.015	7.49

Table 4.1: Range resolution comparison of various LTE bandwidth modes

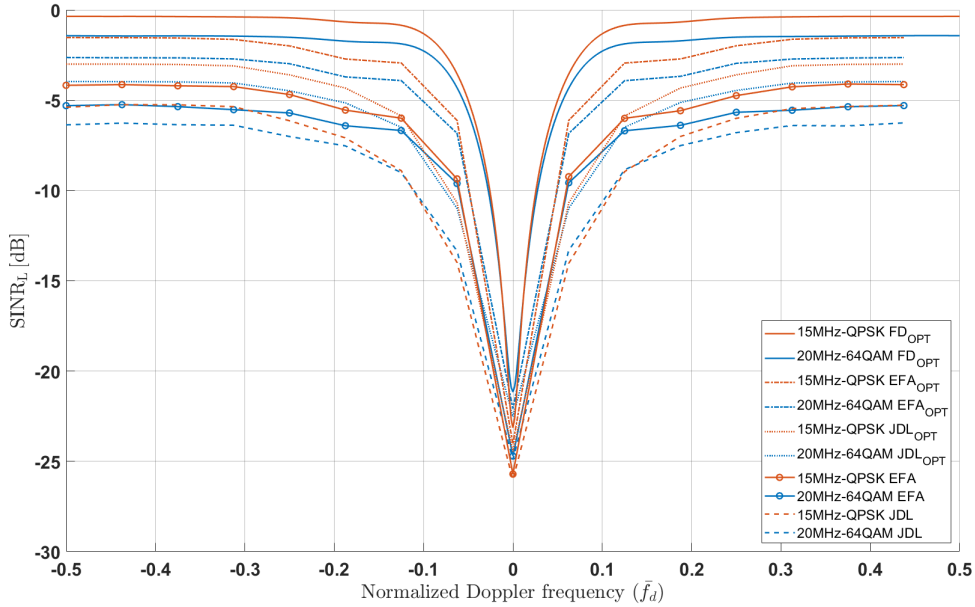

(a) 20 MHz - 64 QAM vs 15 MHZ - QPSK

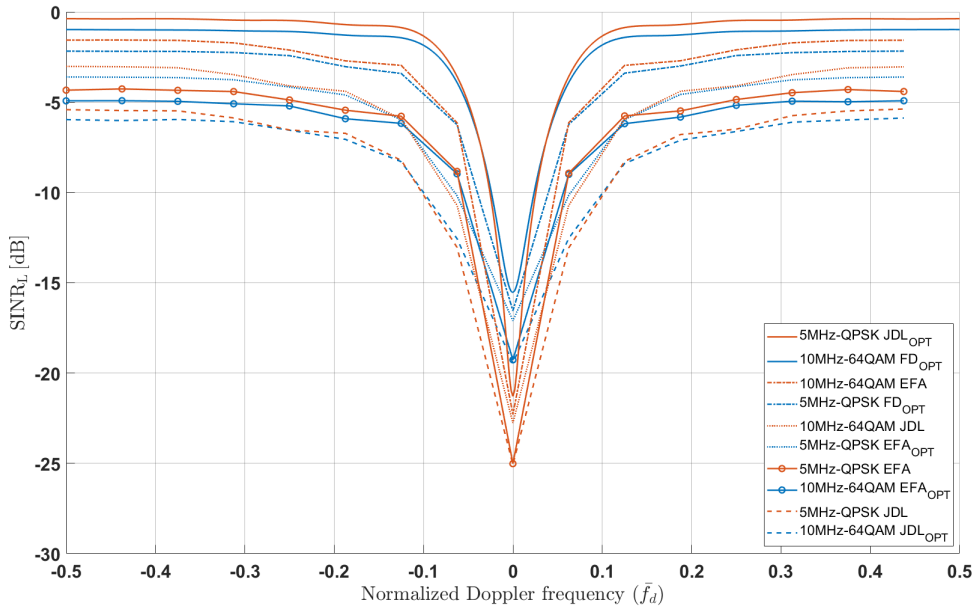

(b) 10 MHz - 64 QAM vs 5 MHZ - QPSK

Figure 4.20: LTE Signal choice trade-off analysis shown through comparison of high bandwidth and high bit-rate signal against a lower bandwidth and lower bit-rate signal, with closer bandwidth mode separation. Simulation plots demonstrate that choice of bit-rate has significant effect when choosing between closely separated LTE bandwidth modes.

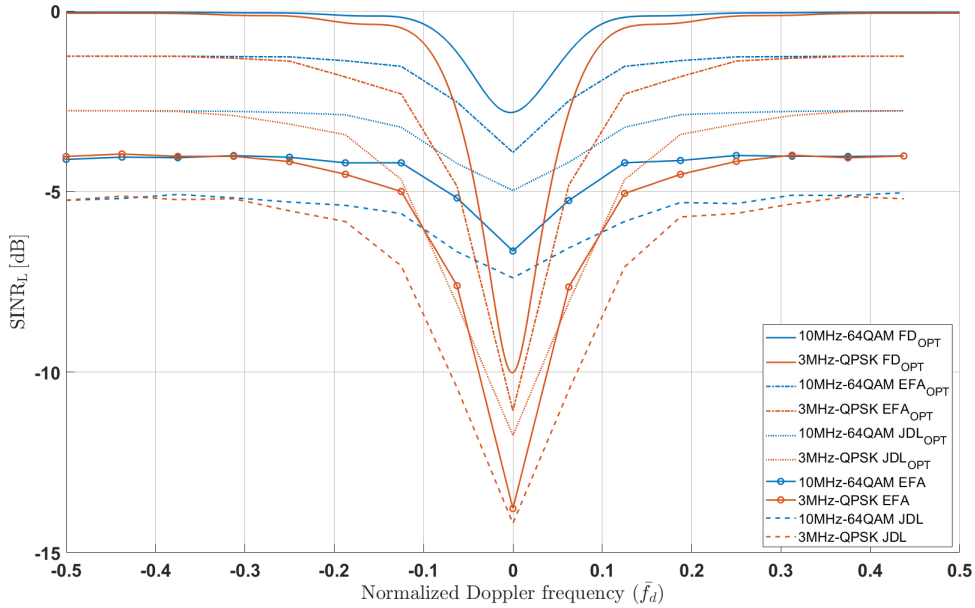

(a) 10 MHz - 64 QAM vs 3 MHZ - QPSK

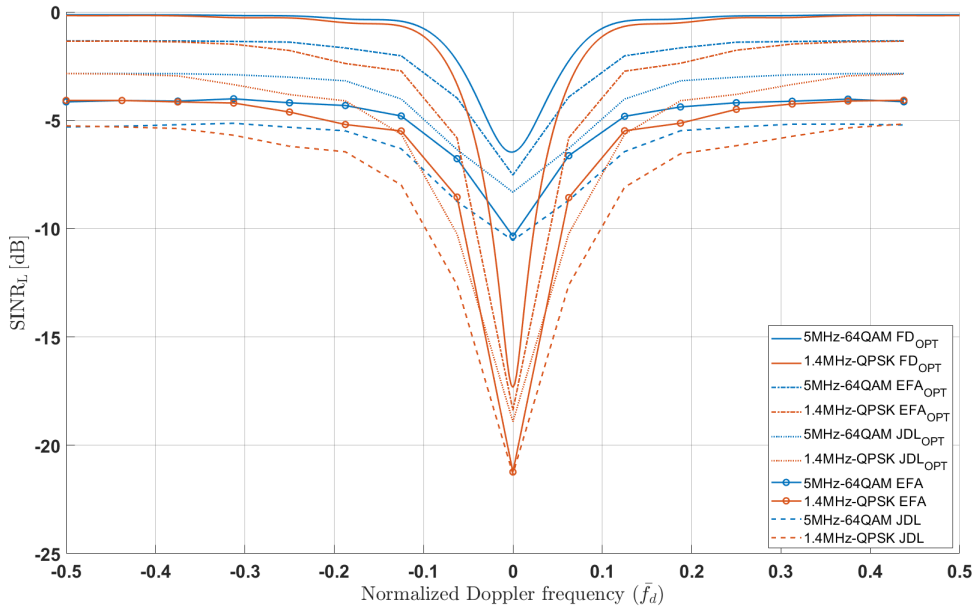

(b) 5 MHz - 64 QAM vs 1.4 MHZ - QPSK

Figure 4.21: LTE Signal choice trade-off analysis shown through comparison of high bandwidth and high bit-rate signal against a lower bandwidth and lower bit-rate signal, with wider bandwidth mode separation. Subfigures demonstrate that choice of bit-rate has insignificant effect when choosing between LTE bandwidth modes that are further apart.

4.5 ICM effects on PBR performance

The RD-STAP results analyzed so far had confirmed that an increase in LTE signal bandwidth or decrease in its bit-rate improves SINR loss performance metrics. This conclusion is consistent with FD-STAP results documented in [2]. Thus, these results have characterized the PBR target detection performance of LTE signal attributes using both FD-STAP and RD-STAP as set forth in 1.2. As an extension to this research objective the impacts of ICM on PBR performance was analyzed using FD-STAP. ICM is modeled through applying time-domain taper to the temporal steering vector as detailed in 2.5.4. Results of this M&S are detailed in this section.

The comparison of FD-STAP and RD-STAP results outlined in this research confirm that they follow the same trend. Therefore, it is expected that ICM impact analysis using RD-STAP will yield results similar to the FD-STAP results covered in this section. However, this hypothesis is not confirmed as part of this research, instead recommended as a potential future research activity.

4.5.1 ICM Method 1 Results

Figures 4.22 - 4.24 compare the effects of ICM, modeled using Method 1, on PBR performance based on FD-STAP algorithm. These results are based on 200 Monte Carlo simulations. These results indicate that the introduction of ICM has widened the clutter notch through comparison of the SINR_{L} curves with and without ICM. Clutter notch widening is representative of clutter sources becoming more incoherent, which requires more DoF to adaptively process and suppress these clutter sources. Additionally, increasing the velocity standard deviation, σ_v, has widened the corresponding SINR_{L} curve clutter notches further. SINR_{L} worsened by approximately 6.5 dB between $\sigma_v = 0$ and $\sigma_v = 2$ cases at $\bar{f}_d = 0.05$ for the LTE signal with QPSK subcarrier modulation. Velocity standard deviation variations had insignificant impact

on SINR_L curves when moving away from the clutter notch region. For example, at $\bar{f}_d = 0.2$, SINR_L degraded by approximately 3 dB between $\sigma_v = 0$ and $\sigma_v = 2$ cases. Hence, this illustrates that the presence of ICM degrades the SINR_L performance in the clutter notch region with severe degradation occurring as σ_v increases. These simulation results further highlight that in the noise-heavy regions varying σ_v had insignificant impact on SINR_L. The ICM performance impact trend outlined above for the QPSK signal can also be extended to 16QAM and 64QAM signals as shown in Figures 4.23 and 4.24. This analysis of the simulation results using FD-STAP confirms the impacts ICM theorized in 2.5.4.1.

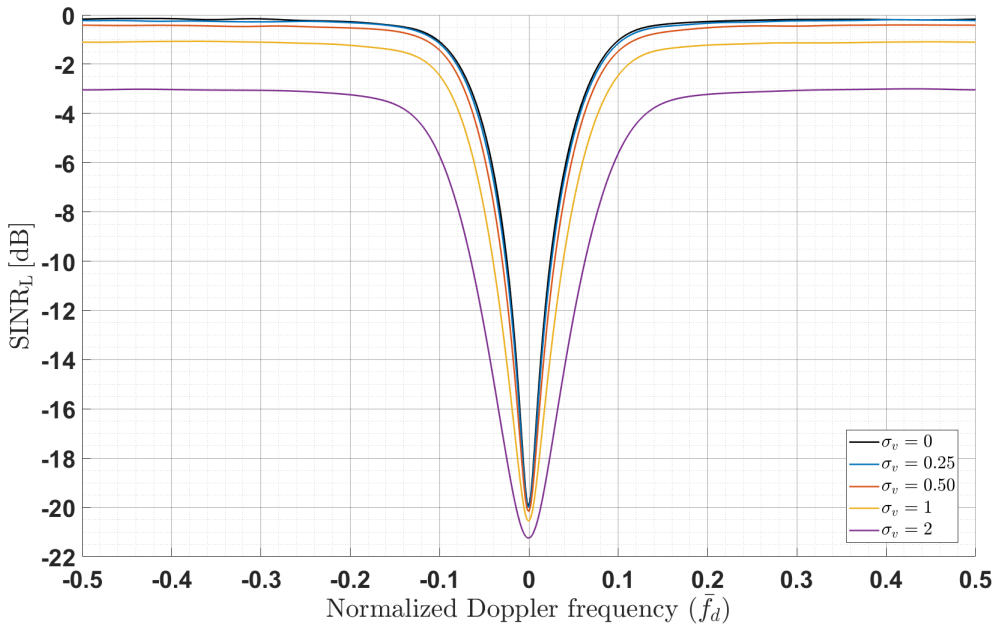

Figure 4.22: Effects of ICM on FD-STAP shown through comparing varying σ_v for 10 MHz - QPSK LTE FDD DL signal.

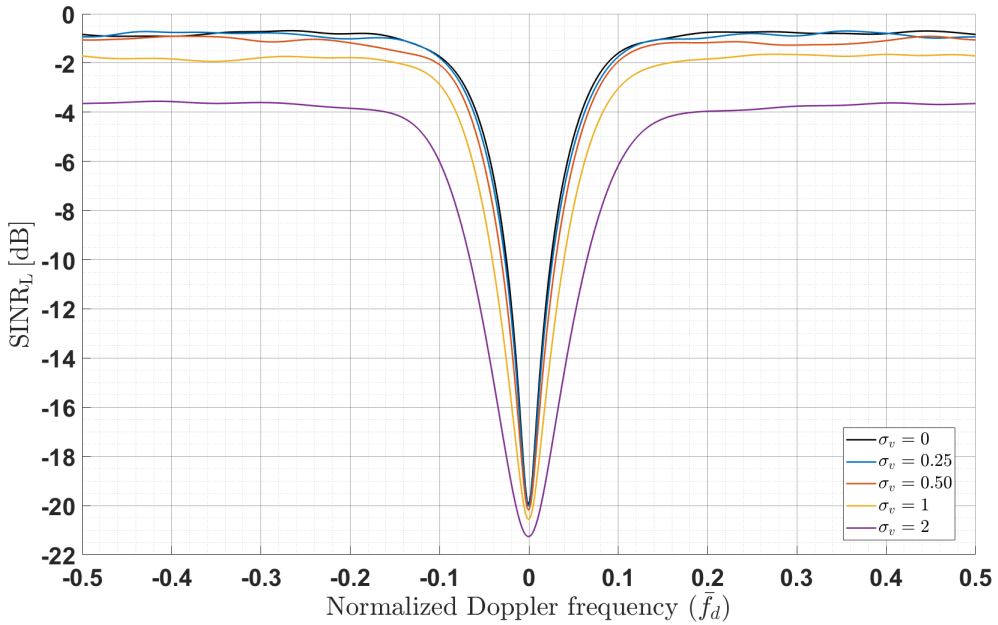

Figure 4.23: Effects of ICM on FD-STAP shown through comparing various σ_v for 10 MHz - 16QAM LTE FDD DL signal.

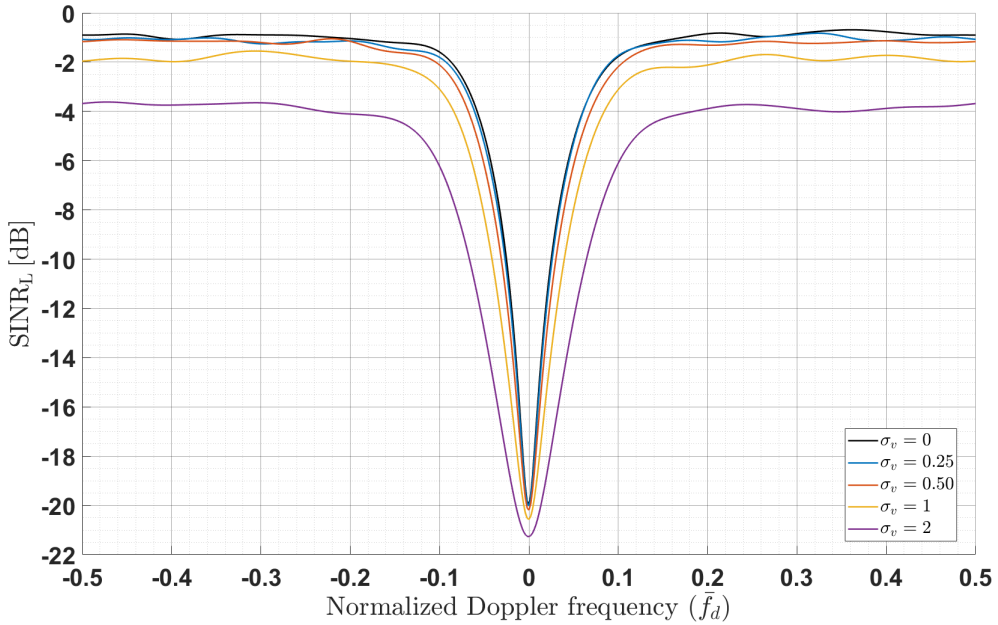

Figure 4.24: Effects of ICM on FD-STAP shown through comparing various σ_v for 10 MHz - 64QAM LTE FDD DL signal.

4.5.2 ICM Method 2 Results

Figures 4.25 - 4.27 compare the effects of ICM modeled using Method 2 based on FD-STAP algorithm. Similar to Method 1 results, these results are also based on 200 Monte Carlo simulations. In line with results presented in 4.5.1, the introduction of ICM has widened the clutter notch. Additionally, increasing the wind speed of the clutter model, v_c, has widened the corresponding $\mathrm{SINR_L}$ curve clutter notches further. Thus, these simulation results using FD-STAP confirms the impacts ICM theorized in 2.5.4.2.

Additionally, increase in v_c has also worsened the $\mathrm{SINR_L}$ over the entire normalized Doppler frequency range. This degradation in normalized Doppler spectrum outside of the clutter notch region is unique to Method 2 approach and was not present within Method 1 results. In fact the analysis of Method 1 results in 4.5.1 had established that varying σ_v had insignificant impact on $\mathrm{SINR_L}$ in the noise-heavy regions. This trend observed with ICM Method 2 results could be attributed to the clutter sources increasingly becoming non-coherent with increase in v_c. This non-coherency contributes in these clutter sources behaving more like random noise sources. As a result, the noise power across the entire Doppler spectrum is seen to increase through degradation in $\mathrm{SINR_L}$, while decreasing the clutter notch depth due to lack of coherency among clutter due to ICM.

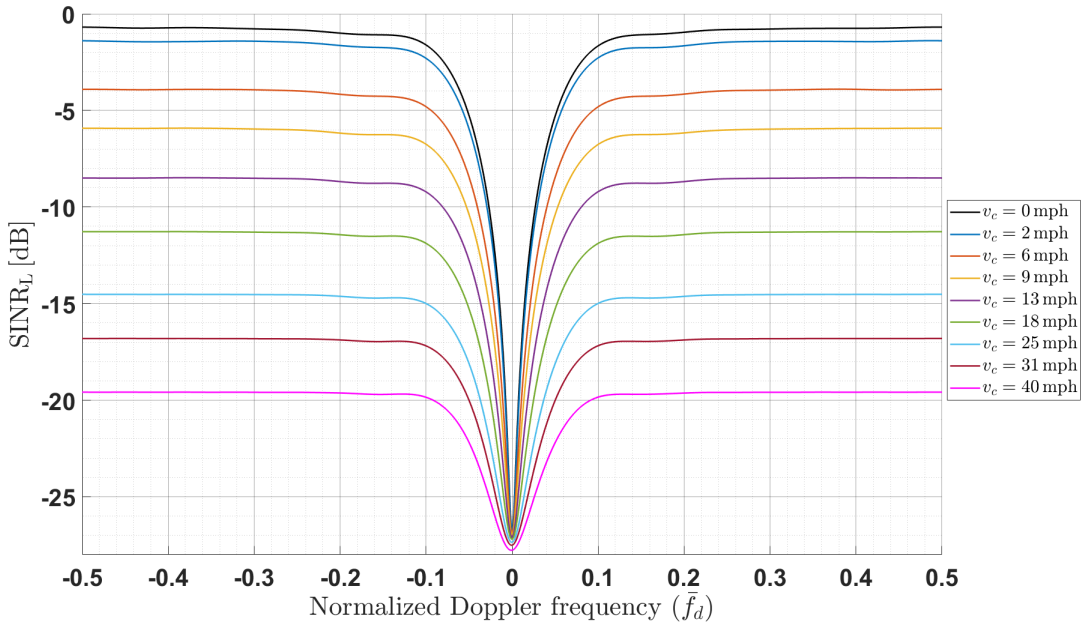

Figure 4.25: Effects of ICM on FD-STAP shown through comparing varying v_c for 10 MHz - QPSK LTE FDD DL signal.

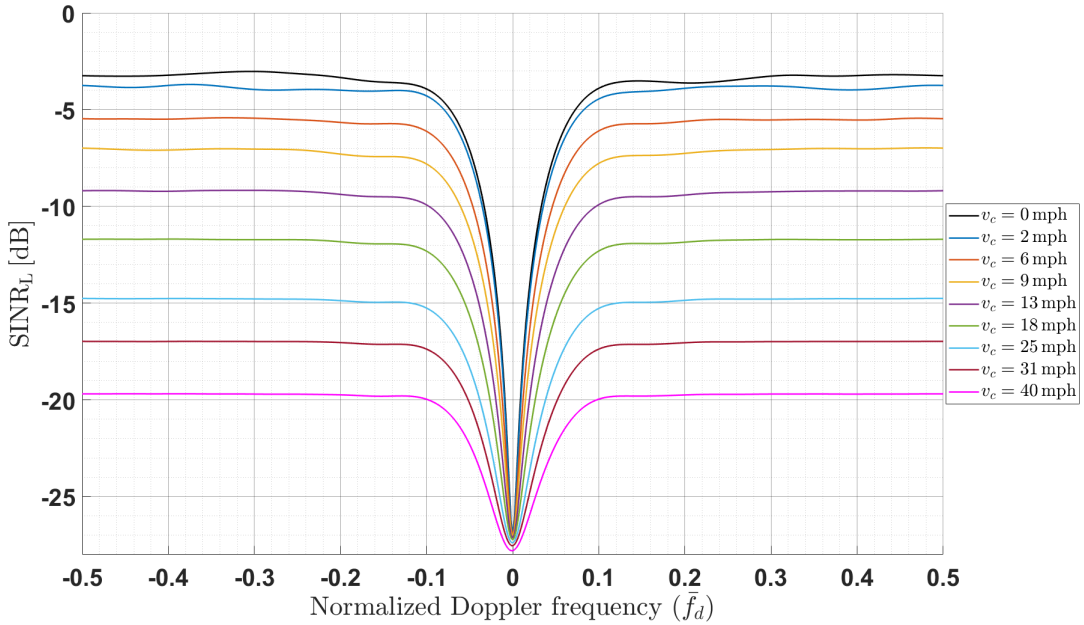

Figure 4.26: Effects of ICM on FD-STAP shown through comparing various v_c for 10 MHz - 16QAM LTE FDD DL signal.

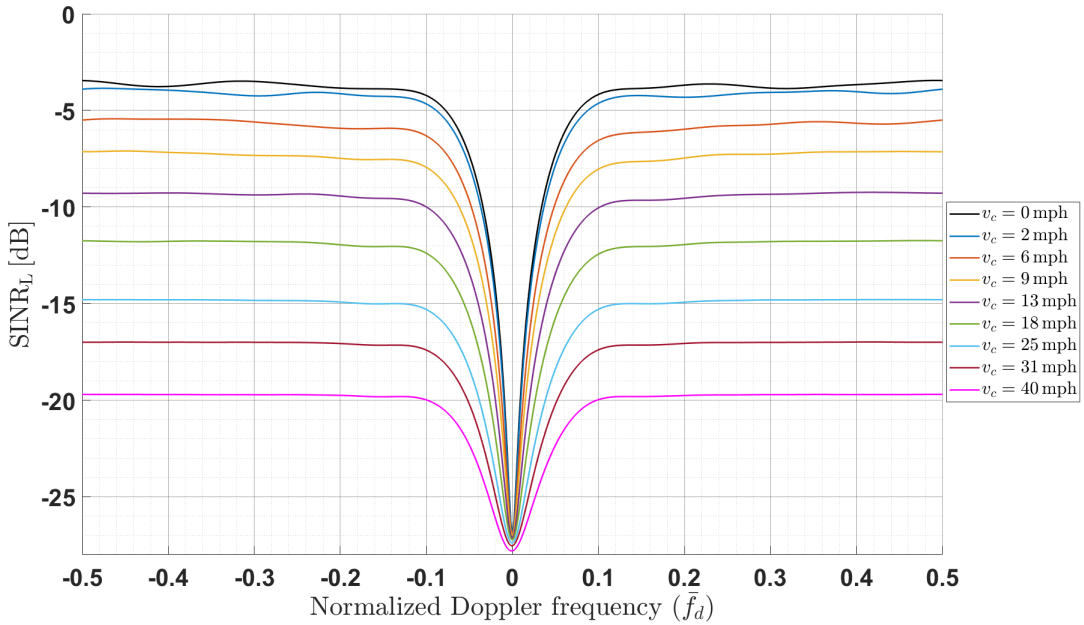

Figure 4.27: Effects of ICM on FD-STAP shown through comparing various v_c of the ICM for 10 MHz - 64QAM LTE FDD DL signal.

Even though the clutter notch widening trend with increase in v_c was consistent across all bit-rates, the previously established SINR_L degradation trend with increase in signal bit-rate (see section 4.3) was no longer present. Figure 4.28 corroborates this observation. These results show that in heavy wind scenarios choosing a low bit-rate LTE signal is not expected to provide a superior target detection performance than high bit-rate signal of same bandwidth. In particular at $v_c = 40\,\text{mph}$ the SINR_L curves for all three bit-rates were almost identical. Thus, Method 2 illustrates increase in v_c diminishes the previously established performance superiority of lower bit-rate LTE signals over the higher bit-rate.

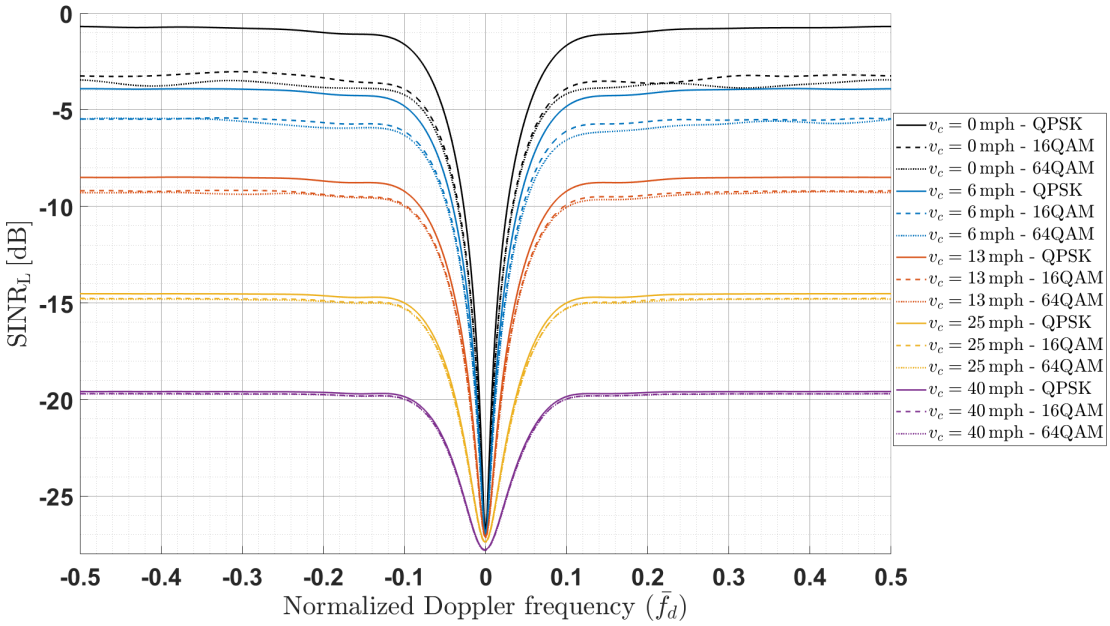

Figure 4.28: Comparison of the effects of varying v_c on different subcarrier modulation schemes of 10 MHz LTE FDD DL signal. Results show that increase in v_c degrades the previously established performance superiority of lower bit-rate LTE signals over the higher bit-rate.

Finally, an alternate comparison metric in terms of 3dB loss clutter notch width of the SINR_L curves was generated for further analysis. Figures 4.29 and 4.30 compare the effects of increasing σ_v and v_c on SINR_L curve clutter notch width at the 3dB loss point for varying bit-rates of the 10 MHz LTE signal. Results indicate both ICM methods increase the clutter notch width with increase in ICM. This confirms the theory outlined in 2.5.4 and the results presented in 4.5. The key difference between the two methods is that clutter notch widened linearly with increase in σ_v under Method 1, whereas the clutter notch widening was non-linear and almost logarithmic under Method 2. This difference in relationship between ICM and clutter notch width is likely due to the underlying mathematical model and could be investigated further as a future research task.

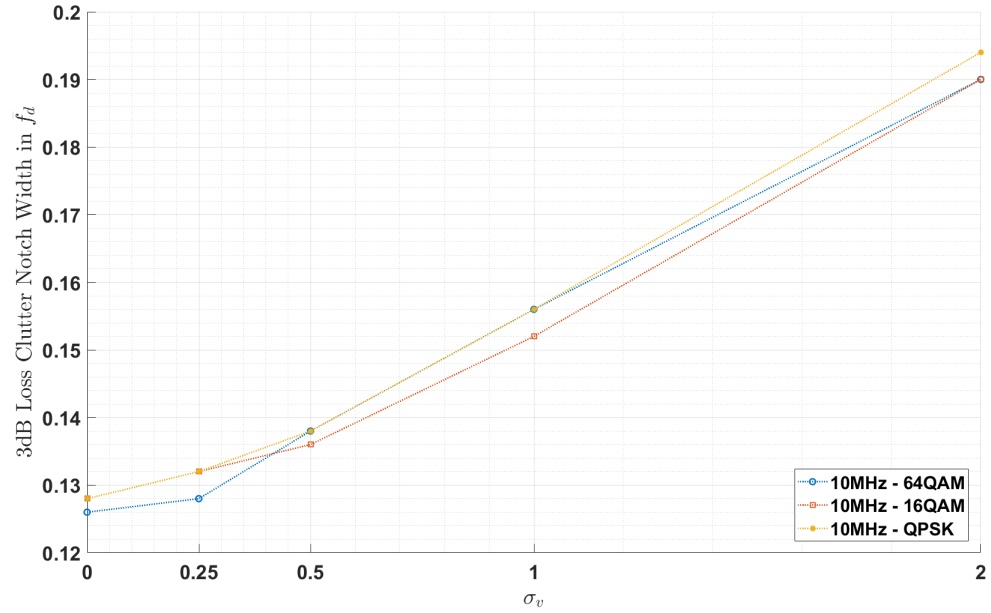

Figure 4.29: Comparison of 3dB loss clutter notch widths for varying σ_v on different subcarrier modulation schemes of 10 MHz LTE FDD DL signal.

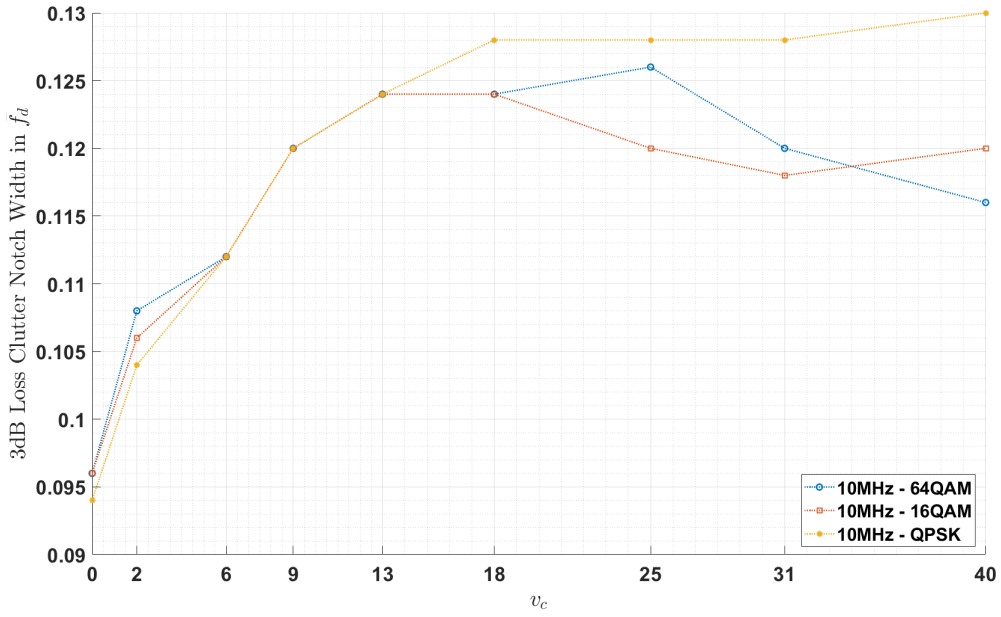

Figure 4.30: Comparison of 3dB loss clutter notch widths for varying v_c on different subcarrier modulation schemes of 10 MHz LTE FDD DL signal.

4.6 Comparison of *Short* and *Full* length matched filter (MF) simulations

The MF length of the simulation results presented so far was restricted to significantly reduce the computation time and resources required. As an example, simulating the clairvoyant clutter space-time steering vectors for the *Full* MF length of 66.67 μs consumed almost 640 GB of RAM for each of the High-band bandwidth mode - bit-rate combination. Furthermore, the computation took significant time to complete one realization, which would have resulted in significantly longer Montecarlo simulations. Hence, the MF length was limited to 5.4 μs for the simulations analyzed thus far. This specific duration of 5.4 μs was selected as the *Short* length MF to remain consistent with [2] and to ensure comparison of simulation results has same underlying MF length. This limits the clutter Doppler spread effects of outer rangebins resulting in better than actual $\text{SINR}_{\text{L,o}}$ and SINR_{L} performance. In order to overcome this issue virtual computing approach was adopted, which simulated the *Full* MF performance characteristics. The *Full* length MF duration was chosen as 66.67 μs, which equates to T_{sym}. Under this method a cluster of computers were gathered to produce a memory capacity of 640 GB, with results of 200 Monte Carlo simulations plotted in Figure 4.31. As highlighted above, the higher bandwidth modes took significantly longer time to compute and resulted in the virtual computer to become unresponsive. Hence, only the Low-band bandwidth modes' *Full* MF characteristics were simulated.

Results clearly indicate modeling the clutter using the entire MF length had worsened $\text{SINR}_{\text{L,o}}$ and SINR_{L} by approximately 1.5 dB for the 3 MHz LTE bandwidth mode using QPSK modulation. Similarly, both SINR loss metrics had worsened by approximately 2 dB for the 1.4 MHz QPSK signal for the *Full* MF length model. Quantitative increase in $\text{SINR}_{\text{L,o}}$ and SINR_{L} were approximated at the noise-heavy regions, at the far extremes of the normalized Doppler frequency scale. Therefore, in realistic applications, using *Full* MF length will worsen both $\text{SINR}_{\text{L,o}}$ and SINR_{L} due

to incorporating the clutter-Doppler spread from the rangebins corresponding to the *Full* MF length. Apart from this point of difference, changing MF length did not result in any other change to the trends analyzed thus far. Hence, LTE signal attributes effects on PBR STAP performance for both FD-STAP and RD-STAP remain valid regardless of the MF length chosen for M&S purposes.

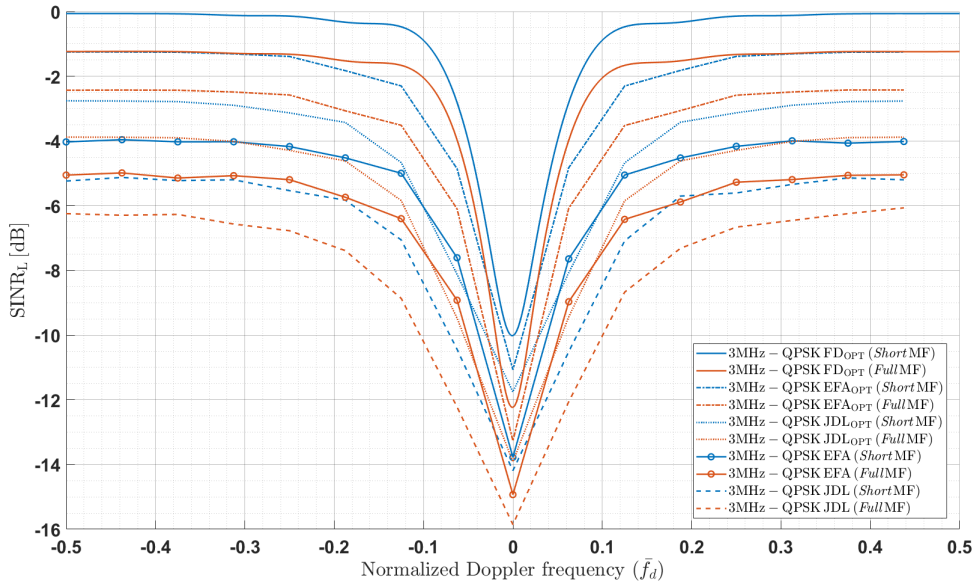

(a) 3 MHZ - QPSK

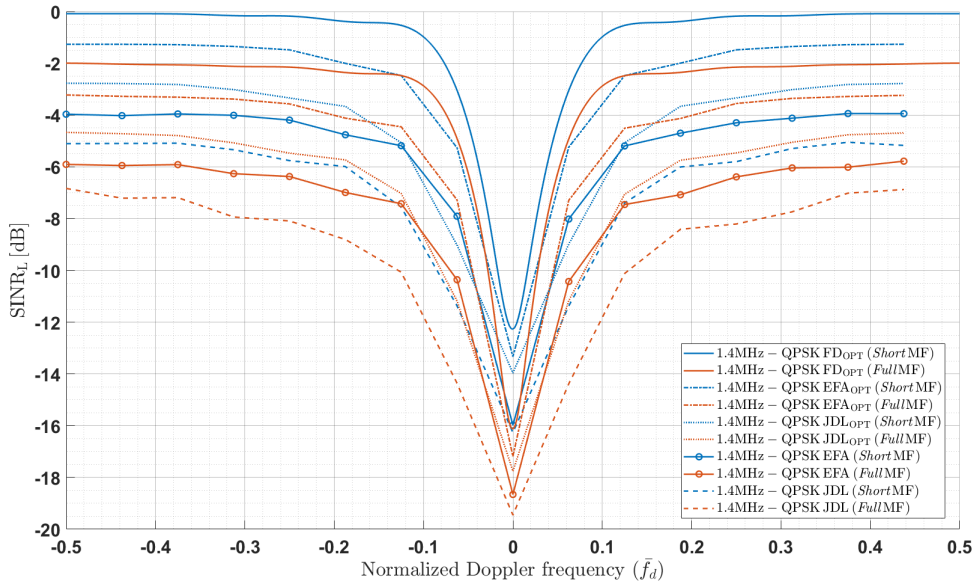

(b) 1.4 MHZ - QPSK

Figure 4.31: SINR loss performance characteristics comparison *Short* and *Full* MF lengths for 3 and 1.4 MHz LTE signals with QPSK modulation. Increasing the MF length degraded both $\text{SINR}_{\text{L,o}}$ and SINR_{L} regardless of LTE signal's bandwidth mode or its subcarrier modulation scheme.

V. Conclusion and Future Work

This thesis tackled the PBR signal selection problem in GMTI missions through generating performance metrics in terms of SINR loss, which compared two key LTE signal attributes using a few STAP techniques. Absence of extensive prior work in this topic area influenced this research to focus primarily on expanding on [2], which addressed a similar problem using optimum FD-STAP. Operationally representative RD-STAP techniques, specifically EFA and JDL, were researched and employed to generate the PBR performance metrics. M&S associated with this research was conducted using MATLAB® with significant computational resource limitation experienced in simulating the SINR curves of higher bandwidth mode LTE signals. This limitation was mitigated through employing virtual computing to increase the physical computing capacity of the processing computer. Simulation results have concluded that increasing signal bandwidth will improve the PBR performance metrics provided in terms of both SINR ($\text{SINR}_{\text{L,o}}$, SINR_{L}) and ΔR. Conversely, increasing the bit-rate of the subcarrier modulation scheme had worsened SINR_{L} and $\text{SINR}_{\text{L,o}}$, with nil effect on ΔR. This trend was consistent regardless of the STAP techniques employed. Additionally, increasing the complexity of RD-STAP algorithms has also worsened both $\text{SINR}_{\text{L,o}}$ and SINR_{L}, without impacting the performance trends of LTE signal attributes. Presence of a performance trade-off between the two LTE signal attributes was investigated and confirmed, which dictates careful consideration of mission requirements in choosing the suitable LTE signal as documented in this paper.

Finally, the impact of ICM on PBR performance was analyzed through two separate ICM models using FD-STAP. FD-STAP results confirmed the theoretical hypothesis that the increase in clutter motion will widen the clutter ridge due to increasing the rank of $\mathbf{R}_c$. Furthermore, the previously established performance superiority of

lower bit-rate LTE signals over the higher bit-rate signals had diminished with increase in wind speed when using Method 2 to model ICM. Analysis of ICM effects using RD-STAP algorithm is recommended as potential future research task.

5.1 Future Work

The following list contains recommended future research activities to build on this research.

1. Investigate the impacts of other signal attributes and features such as the PSS, SSS and CSRE on PBR performance.

2. Explore the impact of ICM on PBR performance using RD-STAP. Verify if RD-STAP results trend is consistent with FD-STAP results documented in this research.

3. Further explore and optimize the ICM methods investigated in this research.

4. Expand this M&S activity to a laboratory or practical setting to validate the simulation results though experiments.

5. Employ a similar M&S methodology to investigate the impact of 5G signal attributes in PBR performance.

6. Explore MF length impacts using $4/3^{\text{rd}}$ Earth model instead of the flat Earth model adopted in this research.

Bibliography

1. J. Ward, "Space-Time Adaptive Processing for Airborne Radar," Massachusetts Institute of Technology, Lexington, Massachusetts, Tech. Rep. 1015, 1994.

2. F. D. Taylor, "Orthogonal frequency division multiplexed waveform effects on passive bistatic radar," Thesis, AFIT-ENG-MS-19-M-058, Air Force Institute of Technology, 2019.

3. A. Evers and J. A. Jackson, "Analysis of an LTE waveform for radar applications," *IEEE National Radar Conference - Proceedings*, vol. 1, pp. 200–205, 2014.

4. ——, "Cross-ambiguity characterization of communication waveform features for passive radar," *IEEE Transactions on Aerospace and Electronic Systems*, vol. 51, no. 4, pp. 3440–3445, 2015.

5. R. S. Abdullah, A. A. Salah, A. Ismail, F. Hashim, N. H. Aziz, and N. E. Rashid, "Ground moving target detection using LTE-based passive radar," *Proceeding - 2015 International Conference on Radar, Antenna, Microwave, Electronics, and Telecommunications, ICRAMET 2015*, pp. 70–75, 2016.

6. A. A. Salah, R. S. Abdullah, A. Ismail, F. Hashim, and N. H. Abdul Aziz, "Experimental study of LTE signals as illuminators of opportunity for passive bistatic radar applications," *Electronics Letters*, vol. 50, no. 7, pp. 545–547, 2014.

7. C. Klock, V. Winkler, and M. Edrich, "LTE-signal processing for passive radar air traffic surveillance," *Proceedings International Radar Symposium*, pp. 1–9, 2017.

8. S. Bartoletti, A. Conti, and M. Z. Win, "Passive radar via LTE signals of opportunity," *2014 IEEE International Conference on Communications Workshops, ICC 2014*, pp. 181–185, 2014.

9. J. P. Stralka and G. G. Meyer, "OFDM-based wideband phased array radar architecture," *2008 IEEE Radar Conference, RADAR 2008*, 2008.

10. F. D. Taylor and J. R. Lievsay, "LTE Bandwidth and Modulation Scheme Effects on Passive Bistatic Radar," in *2018 52nd Asilomar Conference on Signals, Systems, and Computers*, 2018, pp. 916–919.

11. S. D. Blunt and E. L. Mokole, "Overview of radar waveform diversity," *IEEE Aerospace and Electronic Systems Magazine*, vol. 31, no. 11, pp. 2–40, 2016.

12. E. T. S. I, "LTE - Evolved Universal Terrestrial Radio Access (E-UTRA) - physical layer; General description," *3GPP TS 36.201 version 13.0.0 Release 13*, 2016.

13. ——, "LTE - Evolved Universal Terrestrial Radio Access (E-UTRA) - Physical channels and modulation," *3GPP TS 36.211 version 9.0.0 Release 9*, vol. 0, 2010.

14. J. Acharya, L. Gao, and S. Gaur, *Heterogeneous Networks in LTE-Advanced*, 1st ed. John Wiley Sons, Ltd., 2014.

15. E. Dahlman, S. Parkvall, and J. Skold, *4G, LTE The Road to 5G Third Edition*. Elsevier Ltd, 2016.

16. T. Higgins, S. D. Blunt, and A. K. Shackelford, "Time-range adaptive processing for pulse agile radar," *2010 International Waveform Diversity and Design Conference, WDD 2010*, no. 2, pp. 115–120, 2010.

17. W. L. Melvin, "A STAP overview," *IEEE Aerospace and Electronic Systems Magazine*, vol. 19, no. 1 II, pp. 19–35, 2004.

18. W. L. Melvin, M. C. Wicks, and R. D. Brown, "Assessment of multichannel airborne radar measurements for analysis and design of space-time processing architectures and algorithms," *IEEE National Radar Conference - Proceedings*, no. May, pp. 130–135, 1996.

19. M. Rangaswamy, "An overview of space-time adaptive processing for radar," *2003 Proceedings of the International Conference on Radar, RADAR 2003*, pp. 45–50, 2003.

20. H. Wang, Yuhong Zhang, and Qingwen Zhang, "A view of current status of space-time processing algorithm research," vol. 0, pp. 635–640, 2002.

21. J. Scott Goldstein and I. S. Reed, "Theory of partially adaptive radar," *IEEE Transactions on Aerospace and Electronic Systems*, vol. 33, no. 4, pp. 1309–1325, 1997.

22. H. Griffiths and C. Baker, "Passive coherent location radar systems." *IEE Proceedings-Radar, Sonar and Navigation*, vol. 152, no. 4, pp. 153–159, 2005.

23. L. Guisheng, B. Zheng, and X. Zhiyong, "Evaluation of Adaptive Space-Time Processing for Inclined Sideways Looking Array Airborne Radars," in *Proceedings of International Radar Conference*, 1996.

24. R. Klemm, "Introduction to Space-Time Adaptive Processing," *Automatic Classification and Segmentation of Brain Tumor in CT Images using Optimal Dominant Gray level Run Length Texture Features*, 1998.

25. ——, "Ambiguities in Bistatic STAP Radar," 2000.

26. J. S. Goldstein, J. R. Guerci, and I. S. Reed, "Advanced concepts in STAP," *IEEE National Radar Conference - Proceedings*, vol. 0, pp. 699–704, 2000.

27. W. L. Melvin, M. J. Callahan, and M. C. Wicks, "Bistatic STAP: Application to airborne radar," *IEEE National Radar Conference - Proceedings*, pp. 1–7, 2002.

28. R. D. Brown, M. C. Wicks, Y. Zhang, Q. Zhang, and H. Wang, "A Space-Time Adaptive Processing Approach for Improved Performance and Affordability," 1996.

29. R. C. DiPietro, "Extended Factor Space-Time Processing for Airborne Radar Systems," in *Twenty-Sixth Asilomar Conference on Signals, Systems and Computers*, Pacific Grove, CA, USA, 1992.

30. K. Ong, "Angular bin compression for joint domain localised (JDL) processor," pp. 353–356, 2005.

31. R. S. Adve and M. C. Wicks, "Joint domain localized processing using measured spatial steering vectors," *IEEE National Radar Conference - Proceedings*, no. May, pp. 165–170, 1998.

32. S. Wu and Y. Li, "Adaptive channel equalization for space-time adaptive processing," *IEEE National Radar Conference - Proceedings*, 1995.

33. B. Himed, M. C. Wicks, and P. Zulch, "A new constrained joint-domain localized approach for airborne radars," *IEEE National Radar Conference - Proceedings*, pp. 403–407, 2002.

34. Z. Zenghui, Z. Jubo, and W. Yongliang, "Local degrees of freedom of clutter for airborne space-time adaptive processing radar with subarrays," *IET Radar, Sonar and Navigation*, vol. 6, no. 3, pp. 130–136, 2012.

35. T. B. Hale, M. A. Temple, J. F. Raquet, M. E. Oxley, and M. C. Wicks, "Localized three-dimensional adaptive spatial-temporal processing for airborne radar," *IEE Conference Publication*, vol. 150, no. 490, pp. 191–195, 2002.

36. A. K. Shackelford, K. Gerlach, and S. D. Blunt, "Partially adaptive STAP using the FRACTA algorithm," *IEEE Transactions on Aerospace and Electronic Systems*, vol. 45, no. 1, pp. 58–69, 2009.

37. J. R. Lievsay, "Passive Radar Clutter Modeling and Emitter Selection for Ground Moving Target Identification," Ph.D. dissertation, University of Oklahoma, 2017.

38. M. Richards, J. Scheer, and W. Holm, *Principles of Modern Radar: Basic Principles*, 1st ed. SciTech Publishing, 2010.

39. W. L. Melvin and J. A. Scheer, *Principles of modern radar: Advanced techniques*, 1st ed. SciTech Publishing, 2013.

40. J. R. Guerci, "Next generation intelligent radar," *IEEE National Radar Conference - Proceedings*, pp. 7–10, 2007.

41. J. Billingsley, "Exponential Decay in Windblown Radar Ground Clutter Doppler Spectra : Multifrequency Measurements and Modeling," Tech. Rep. 997, 1996.

42. S. Suntharalingam and J. R. Lievsay, "Performance Analysis of LTE Signals in RD-STAP Applications," *IEEE International Radar Conference - Proceedings*, 2021.

43. Telesystem Innovations, "Telesystem Innovations LTE in a Nutshell : The Physical Layer," 2010.

44. Rohde&Schwarz, "EUTRA / LTE Digital Standard and Operating Manual for R&S Signal Generators," 2013.

45. N. Levanon and E. Mozeson, *Radar Signals*, first edit ed., N. Levanon, Ed. Hoboken, New Jersey: John Wiley Sons, Ltd., 2004.

46. J. R. Lievsay and N. A. Goodman, "Multi-Transmitter clutter modeling for passive STAP," *2016 IEEE Radar Conference, RadarConf 2016*, no. 1, pp. 1–6, 2016.

47. N. J. Willis, *Bistatic Radar*, 2nd ed. Raleigh, NC, USA: SciTech Publishing, Inc, 1995.

48. J. R. Guerci, *Space-Time Adaptive Processing for Radar*, 1st ed. Artech House, 2003.

49. F. E. Nathanson, J. P. Reilly, and M. N. Cohen, *Radar Design Principles: Signal Processing and the Environment*. SciTech Publishing, Inc, 1999.

50. P. M. Techau, J. S. Bergin, and J. R. Guerci, "Effects of internal clutter motion on STAP in a heterogeneous environment," *IEEE National Radar Conference - Proceedings*, pp. 204–209, 2001.

51. H. Wang, M. Wicks, W. Zhang, and L. Hall, "Improvements in Existing Airborne Early Warning Radars," pp. 189–196, 1994.

52. L. E. Brennan, J. D. Mallett, and I. S. Reed, "Adaptive Arrays in Airborne MTI Radar," *IEEE Transactions on Antennas and Propagation*, vol. 24, no. 5, pp. 607–615, 1976.

53. H. Wang and L. Cai, "On Adaptive Spatial-Temporal Processing for Airborne Surveillance Radar Systems," *IEEE Transactions on Aerospace and Electronic Systems*, vol. 30, no. 3, pp. 660–670, 1994.

54. M. I. Skolnik, *Radar Handbook*, 3rd ed. McGraw-Hill, 2008.

55. A. Nundu, "Direct Path Interference Suppression and Received Signal Processing for OFDM Passive Radar," Thesis, AFIT-ENG-MS-19-M-049, Air Force Institute of Technology, 2019.

REPORT DOCUMENTATION PAGE

Form Approved
OMB No. 0704–0188

1. REPORT DATE *(DD–MM–YYYY)*	2. REPORT TYPE	3. DATES COVERED *(From — To)*
19–03–2021	Master's Thesis	Sept 2019 — Mar 2021

4. TITLE AND SUBTITLE

Performance Analysis of Long-Term Evolution Signals in Passive Bistatic Radar applications using Reduced Dimension Space-Time Adaptive Processing techniques

5a. CONTRACT NUMBER

5b. GRANT NUMBER

5c. PROGRAM ELEMENT NUMBER

6. AUTHOR(S)

FLTLT Sureshan Suntharalingam

5d. PROJECT NUMBER

5e. TASK NUMBER

5f. WORK UNIT NUMBER

7. PERFORMING ORGANIZATION NAME(S) AND ADDRESS(ES)

Air Force Institute of Technology
Graduate School of Engineering and Management (AFIT/EN)
2950 Hobson Way
WPAFB OH 45433-7765

8. PERFORMING ORGANIZATION REPORT NUMBER

AFIT-ENG-MS-21-M-082

9. SPONSORING / MONITORING AGENCY NAME(S) AND ADDRESS(ES)

Intentionally Left Blank.

10. SPONSOR/MONITOR'S ACRONYM(S)

11. SPONSOR/MONITOR'S REPORT NUMBER(S)

12. DISTRIBUTION / AVAILABILITY STATEMENT

DISTRIBUTION STATEMENT A:
APPROVED FOR PUBLIC RELEASE; DISTRIBUTION UNLIMITED.

13. SUPPLEMENTARY NOTES

14. ABSTRACT

Widespread availability of long term evolution (LTE) signals makes them potential for use in passive bistatic radar (PBR) applications. However, their utility in such applications is yet to be fully explored. This research focuses on the key LTE signal attributes, such as subcarrier modulation schemes and bandwidth, and their effect on PBR application. space-time adaptive processing (STAP) concepts, both full-dimension STAP (FD-STAP) reduced-dimension STAP (RD-STAP), were employed to evaluate and compare the effects of varying these signal attributes, in terms of signal to interference-plus-noise ratio (SINR) loss metrics. Simulation results concluded that decreasing LTE signal's bandwidth and increasing its bitrate will worsen both $\mathrm{SINR_L}$ and $\mathrm{SINR_{L,o}}$. This trend remained valid irrespective of the type of STAP algorithm used. This research further analyzed the SINR performance trade-off resulting from the choice of an LTE signal of opportunity for airborne PBR application solely based on just one of the two signal attributes discussed in this report. Additionally, the impacts of intrinsic clutter motion (ICM) on PBR performance metrics was examined and characterized using FD-STAP.

15. SUBJECT TERMS

PBR, STAP, RD-STAP, LTE, SINR

16. SECURITY CLASSIFICATION OF:			17. LIMITATION OF ABSTRACT	18. NUMBER OF PAGES	19a. NAME OF RESPONSIBLE PERSON
a. REPORT	b. ABSTRACT	c. THIS PAGE			Major James R. Lievsay, AFIT/ENG
U	U	U	UU	118	19b. TELEPHONE NUMBER *(include area code)* (937) 255-6565, ext 3369; james.lievsay@afit.edu